Universitat Politècnica de Catalunya

Departament d'Enginyeria Elèctrica - Centre
d'Innovació Tecnològica en Convertidors
Estàtics i Accionaments

UPC Departament d'Enginyeria Elèctrica
UNIVERSITAT POLITÈCNICA DE CATALUNYA

UPC CITCEA - Centre d'Innovació Tecnològica
en Convertidors Estàtics i Accionaments

Doctoral Thesis

Multiterminal HVDC transmission systems for offshore wind

Author:	**Agustí Egea-Àlvarez**
Supervisor:	**Oriol Gomis-Bellmunt**

Barcelona, July 2014

Universitat Politècnica de Catalunya
Departament d'Enginyeria Elèctrica
Centre d'Innovació Tecnològica en Convertidors Estàtics i Accionament
Av. Diagonal, 647. Pl. 2
08028 Barcelona

First printed copy, July 2014

UNIVERSITAT POLITÈCNICA DE CATALUNYA
BARCELONATECH
Escola de Doctorat

Acta de qualificació de tesi doctoral

Curs acadèmic:

Nom i cognoms

Programa de doctorat

Unitat estructural responsable del programa

Resolució del Tribunal

Reunit el Tribunal designat a l'efecte, el doctorand / la doctoranda exposa el tema de la seva tesi doctoral titulada

____

____.

Acabada la lectura i després de donar resposta a les qüestions formulades pels membres titulars del tribunal, aquest atorga la qualificació:

☐ NO APTE ☐ APROVAT ☐ NOTABLE ☐ EXCEL·LENT

(Nom, cognoms i signatura) President/a	(Nom, cognoms i signatura) Secretari/ària	
(Nom, cognoms i signatura) Vocal	(Nom, cognoms i signatura) Vocal	(Nom, cognoms i signatura) Vocal

______________________, _______ d'/de __________________ de _______________

El resultat de l'escrutini dels vots emesos pels membres titulars del tribunal, efectuat per l'Escola de Doctorat, a instància de la Comissió de Doctorat de la UPC, atorga la MENCIÓ CUM LAUDE:

☐ SÍ ☐ NO

(Nom, cognoms i signatura) President de la Comissió Permanent de l'Escola de Doctorat	(Nom, cognoms i signatura) Secretària de la Comissió Permanent de l'Escola de Doctorat

Barcelona, _______ d'/de ____________________ de _________

-”Je connais une planète où il y a un Monsieur cramoisi. Il n’a jamais respiré une fleur. Il n’a jamais regardé une étoile. Il n’a jamais aimé personne. Il n’a jamais rien fait d’autre que des additions. Et toute la journée il répète comme toi: ”Je suis un homme sérieux! Je suis un homme sérieux!” et ça le fait gonfler d’orgueil. Mais ce n’est pas un homme, c’est un champignon!”

-”Un quoi?”

-”Un champignon!”

Le Petit Prince. Antoine de Saint-Exupéry

Acknowledgements

First of all, I would like to express my sincere gratitude to my PhD supervisor Dr. Oriol Gomis-Bellmunt for his guidance and support over this more than 7 years of professional relationship. However, Oriol was not alone in his guidance and during my international internships I had excellent supervisors. During my first internship in the ELECTA group (KU Leuven) I was guided by Dr. Dirk Van Hertem and during my second stage in Alstom Grid UK I was guided by Dr. Fainan Hassan. I would also like to thank the Spanish Economy and Competitiveness Ministry that funds this PhD thesis by means of a FPI grant.

El meu segon agraïment és cap a la meva família especialment als meus Pares (Mercè i Toni) i les meves avies (Carolina i Maria). Com tampoc podria oblidar tota aquella gent que m'ha anat donant un cop de mà i hem conformant els diferents estrats que conformen aquesta tesis. El meu profund agraïment als amics del Le Citcearie Française (L′Adria, la Paola, l′Edu i la Mònica), en Yong, i els meus millors aprenents que mai he tingut, els Joans (Sau i Al.les). També cal sumar-hi tots els nanos i nanes del CITCEA que m′han aguantat durant tot aquest temps (Gabri, Tomàs, Carlos M., Alex S., Isaac, Aleix, Dani H., Pol, Pau S., Cristian...). Com tampoc es podria concebre aquesta tesis sense els savis consells, d′ en Toni, en Sam, en Montesinos, l′Andi, en Roberto ni els Joans (Bergas i Rull) ni les noies de gestió la Maria, la Judit i la Paz. També recordar als companys de Departament en Lluis Monjo i en David Romero, en Fernando de l′IREC, als companys de la junta de la Societat Catalana de Tecnologia (SCT-IEC), especialment el seu president el Sr. Federico Luque, i als amics de fora de la Universitat l′Andreu, l′Ignasi, en Saül i en Jordi.

Also, I would like to thank my workmates in Alstom Grid Stafford, Sajjad, Jose, Jonathan John and Costas and the HVDC-UPC team, Abel, Raza, Kevin, Afsaneh and Ana. Ik wil ook mijn collega's uit Leuven bedanken voor het advies en de koffiepauzes: Jef, Carlos, Simon, Benjamin en Hakan.

Finally, I would like to thank my English family, Liz, David, Peter and John for all the support that I received during my visit in Stafford and all the effort that they put into helping me understand British culture, but anyway... ”I know nothing I am from Barcelona...”

Le Agus

Abstract

Offshore wind is emerging as one of the future energy vectors. Offshore wind power plant locations provide stronger and constant wind speed that allows the extraction of more power compared to onshore locations. In addition, as wind turbine component transportation is less restricted to terrestrial infrastructure, larger and more powerful wind turbines can be installed offshore. In Europe, 1,567 MW of offshore wind power was installed in 2013. It represents 14% of the total wind power installed in Europe.

Offshore wind power plants near the shore can be connected to the main grid by means of conventional AC technology. However, if these wind farms are installed further than 80-100 km, the use of AC equipment is economically infeasible due to reactive power issues. In these applications HVDC system based on static converters can be used.

The projects built and commissioned nowadays are based on point-to-point connections, where, each wind farm or wind farm clusters are connected to the terrestrial grid individually. Consequently, these lines might be understood as an extension of the AC system. If different offshore wind farms are interconnected among themselves and connected at the same time to different AC systems, for example, different countries, a DC grid is created. This scenario creates one of the most important challenges in the electrical power system since its creation, more than 100 years ago. The most relevant challenges to be addressed are the stability and operation of the DC grid and the integration and interaction with the AC grid.

This thesis addresses various aspects related to the future Multiterminal-HVDC systems for the transmission of offshore wind power. First, voltage control and the system operation are discussed and verified by means of emulation using an HVDC scaled experimental platform built for this purpose. Voltage stability might be endangered during contingencies due to the different inertia time constants of the AC and the DC system. DC systems only have the equivelent inertia of the capacitors compared to synchronous machines rotating masses of the AC systems. Therefore, in faulty conditions the power transmitted through the DC system must be reduced quickly and efficiently. For this reason, in this thesis a coordinated power reduction algorithm is presented taking advantage of Dynamic Braking Resistors (DBR) connected to onshore converter stations and the ability of the power plants to reduce the generated power.

From the AC and DC grid integration point of view, the connection point between the offshore grid and the AC grid might be located remotely leading to a connection with a reduced Short Circuit Ratio (SCR). In the literature several issues regarding the connection of transistor-based power converters to weak AC grid have been reported. In this thesis an advanced control for Voltage Source Converters connected to weak grids is presented and tested by means of simulations.

From the AC and DC grid interactions shown, the voltage stability is not enough to operate a DC grid. Transmission System Operators (TSO) operate the power flow through the cables and the power exchanged by the power converters. In this thesis, a novel hierarchical power flow control method is presented. The aim of the proposed power flow control is to obtain the desired power flows by changing the voltage control set-points while the system stability is ensured.

Finally, a control procedure for offshore wind farms based on Squirrel Cage Induction Generators connected to a single power converter is introduced.

Resum

L'energia eòlica marina emergeix com un dels vectors energètics del futur. Les localitzacions eòliques marines proporcionen vens més forts i constants que les terrestres, cosa que permet extreure més potència. A més a més, els aerogeneradors marins poden ser més grans i més potents ja que es redueixen les limitacions de gàlib existent en les infraestructures terrestres. A tall d'exemple, l'any 2013 a Europa es van instal.lar 1.567 MW de potència eòlica marina, cosa que representa un 14% de la potència eòlica instal.lada a Europa. Els parcs eòlics marins poden ser connectats a la xarxa elèctrica terrestre utilitzant aparamenta convencional de corrent alterna, però quan la distancia amb la costa excedeix els 80-100 km l'ús d'aquesta tecnologia es torna econòmicament inviable degut a l'energia reactiva generada en els conductors. Per solucionar aquest problema, s'emparen els sistemes en corrent continua basats en convertidors estàtics.
Els projectes construïts o projectats a dia d'avui es basen en esquemes de connexió punt-a-punt, on, cada parc eòlic o agrupació de parcs eòlics es troba connectat a la xara terrestre individualment. En conseqüència, l'operació d'aquestes línies es pot considerar com una extensió de la xarxa d'alterna. Però, si s'interconnecten diferents parc eòlics amb diferents xarxes terrestres d'alterna (per exemple, diferents països) en corrent continua, s'obtenen xarxes en corrent continua. Aquest nou escenari crea un dels majors reptes des de la creació dels sistema elèctric de potencia, ara fa més de 100 anys. Entre aquests reptes hi ha l'estabilitat i l'operació dels sistemes en corrent contínua i la seva integració i coexistència amb les xarxes en corrent alterna. En la present tesis s'han estudiat diferents aspectes dels futurs sistemes multiterminal en alta tensió en corrent contínua (HVDC, en anglès) per la transmissió de potencia generada mitjançant parcs eòlics marins. Primerament, es descriu el control de tensió i els modes d'operació dels sistemes multiterminal i es verifiquen en una plataforma experimental construïda per aquest propòsit. L'estabilitat de tensió dels sistemes en corrent continua, es pot veure afectada durant una falta a la xarxa d'alterna degut a la reduïda inèrcia dels sistemes multiterminal, només formada pels condensadors dels

convertidors i els cables. Així la potència que no pot injectar a la xarxa ha de ser reduïda de forma ràpida i eficient. Per això, en aquesta tesis es presenta un sistema coordinat de reducció de potència que utilitza la resistència de frenat dels convertidors de connexió a la xarxa i els mètodes de reducció de potència dels parcs eòlics.

Des del punt de vista de la integració de les xarxes en continua i en alterna, el punt d'interconnexió pot estar localitzat llunys dels grans centres de generació, la qual cosa implica tenir una potència de curtcircuit molt reduïda. En la bibliografia científica s'han descrit diverses problemàtiques a l'hora de connectar un convertidor de commutació forçada a les xarxes dèbils. Per tal de pal.liar aquests inconvenients, en aquesta tesis es presenta un algorisme avançat de connexió de convertidors a xarxes dèbils basat en control vectorial.

Des del punt de vista de les interaccions i interoperabilitat dels sistemes en corrent alterna i continua, no n'hi ha suficient en garantir l'estabilitat, ja que el propòsit finals dels operadors de xarxa és fer fluir una potencia a traves de la xarxa per tal de satisfer la demanda. Per aquest propòsit en aquesta tesis es presenta un control jeràrquic de control del flux de potència que fixa el flux de potència a traves d'una xarxa multiterminal canviant les consignes del control primari, tot assegurant l'estabilitat del sistema.

Per tancar la tesis, es presenta un nou controlador per parcs eòlics basats en aerogeneradors de gàbia d'esquirol controlats per un sol convertidor.

Contents

List of Figures

List of Tables

Nomenclature

Acronyms

AC	Alternating Current
CITCEA	Centre Innovació Tecnològica en Convertidors Estàtics i Accionaments
DAQ	Data Acquisition
DBR	Dynamic Braking Resistor
DC	Direct Current
DFIG	Double Fed Induction Machine
GSC	Grid Side Converter
HVAC	High Voltage Alternating Current
HVDC	High Voltage Direct Current
IGBT	Insulated Gate Bipolar Transistor
IMC	Internal Model Control
IPCC	Intergovernmental Panel on Climate Change
LCC	Line Commuted Converter
LHP	Left Hand Plane
LPF	Low Pass Filter
LTI	Linear Time Invariant

MMC	Modular Multilevel Converters
MPPT	Maximum Power Point Tracker
MT-HVDC	Multiterminal-HVDC
PCC	Point of Common Coupling
PI	Proportional-Integral Controller
PLL	Phase Locked Loop
PMSM	Permanent Magnet Synchronous Machine
PSC	Power Synchronization Control
SCADA	Supervisory Control And Data Acquisition
SCIM	Squirrel Cage Induction Machines
SCR	Short Circuit Ratio
TSO	Transmission System Operator
UPC	Universitat Politècnica de Catalunya
VSC	Voltage Source Converter
WF	Wind Farm
WFC	Wind Farm Converters
WGC	Wind Generator Converter
WT	Wind Turbine
WTC	Wind Turbine Converter

Chapter 1

Introduction

Over the last decades world climate conditions have experienced alarming changes, such as the constant temperature increase since 1971 or the desertification of certain parts of the Earth. According to the Intergovernmental Panel on Climate Change (IPCC), it is "extremely likely" that the human influence was the dominant cause of global warming between 1951 and 2010 [1]. This period matches with the global industrialization process started after the Second World War. One of the main causes of this climate change is the enormous amount of greenhouse effect gases that are released to the atmosphere every year. Electrical energy and heat production have an important role in the greenhouse gases mix. It represents 27% of the total greenhouse effect gasses released in Europe in 2012 [2].

To counteract the human effects different governmental programs have been launched worldwide. One of the most ambitious projects is the European 20-20-20 targets program. This program has three main key points: to reduce greenhouse gas emissions by 20% compared to 1990 level, to raise the share of EU energy consumption produced from renewable resources to 20% and to improve the EU's energy efficiency by 20% [3]. From the previous points, it can be deduced that the electrical generation mix needs to become less-carbon intensive.

One of the most fastest-growing renewable electrical generation technologies is the wind-based power plants, especially in offshore locations. At the end of 2013 there were 6,562 MW of offshore power installed [4] in Europe, of which 1,567 MW was installed in 2013. Some advantages of installing wind power plants offshore are: the availability of more powerful and constant wind resources, fewer transport and logistic problems and less acoustic and visual pollution among others. On the other hand, offshore wind power plants are most costly than onshore wind power plants.

There are many engineering challenges related to offshore wind farms. In the electrical engineering field, the integration of these power plants to the main AC grid represents one of the biggest challenges and breakthrough in power system engineering from the last decades. If traditional AC (Alternating Current) technology is used, large amounts of reactive power appear in the conductors, even if no active power is transmitted. This phenomenon is due to the capacitive effect created between the submarine cables and the undersea environment.

Reactive power can be compensated using inductances, but from an economic point of view, there is a critical distance that makes the use of DC (Direct Current) more attractive. The critical distance depends on each particular case but it is located around 100 km [5]. Until recently, High Voltage Direct Current (HVDC) transmission systems were based on current-fed Line Commuted Converters (LCC). New converter topologies and lower-priced fast-switching semiconductors recently made possible to build voltage source converter (VSC) based HVDC transmission systems. The benefits of using VSC are the ability to independently control the active and reactive power while reducing the size of the output filters needed to have a low harmonic distortion, and has a smaller foot print compared to LCC technology [6, 7, 8, 9]. However, research using current-based converters is on-going [10, 11].

Most of the existing HVDC transmission systems use point-to-point connections [12]. This means that each wind farm converter is directly connected to the main AC grid by means of a DC cable. The opportunity to create new DC grids [13] offshore both interconnecting different countries and transmitting all the wind power generated have increased the interest in converting point-to-point connections to meshed DC grids. The connection of different wind farms and different onshore AC grids can be performed with a common DC grid based on a Multiterminal-HVDC (MT-HVDC) or DC grid arrangement, where the terminals are wind farms or grid connections.

1.1 Research motivation

Considering this future scenario, the main goals of this thesis are:

- To understand the existent HVDC, HVAC and wind farm technology (hardware, control...) and its integration and interaction.
- To obtain rigorous models for the DC and AC grid, and the wind turbines including the power converter and their control systems.
- To design and build an experimental platform for an MT-HVDC system used to study the different DC voltage control algorithms for MT-HVDC systems.
- To study the power flow control in a DC system ensuring grid stability and interactions with the AC grid.
- To study possible power reductions methods and implementations for a MT-HVDC system in case of an AC contingency.
- To understand the weak grids phenomena (stability, electrical limits...) and to propose solutions for the control of a VSC connected to a weak grid.
- To propose new control procedures for offshore wind farms equipped with squirrel cage and fed by a unique power converter.

1.2 Thesis Contributions

The main thesis contributions of this thesis are

- Verification of the basic control structures and operation modes for an HVDC system by means of an experimental platform design and built for this purpose.
- A power reduction coordinated scheme between the HVDC Dinamic Braking Resistor and the wind farm has been proposed. The controllers have been designed avoiding the limit cycle existence by mean of the describing function.

- A novel hierarchical power flow control system for MT-HVDC grid, inspired in the traditional AC control system, is proposed.
- A non-linear control for VSC connected to weak grid based on vector control is presented and verified by means of simulations.
- A Control procedure for wind farm based on squirrel cage induction generators and connected to a single power converter is presented and verified by means of simulations.

1.3 Thesis Outline

The thesis is organized in 9 chapters. Chapter 2 presents the different AC (L and LC coupling filter) and DC grid (Back-to-Back, 2 terminal and 4 terminal grid) models and their control structures based on vector control. Chapter 3 presents the MT-HVDC operation points according to the control equations and the power converter limits. Chapter 4 deals with the design and validation of an MT-HVDC experimental platform under some scenarios. Chapters 5 and 6 deal with DC system-specific problems. Chapter 5 presents a coordinated power reduction method that allows control of the DC voltage during an AC contingencies. Chapter 6 analyses the weak grid problem and proposes a modified vector control scheme. Chapter 7 presents the hierarchical power flow control for MT-HVDC systems. Chapter 8 introduces the new control procedure for squirrel cage-based wind farms controller by means of a single power converter.Finally, chapter 9 summarises the thesis results and elaborates the conclusions.

1.4 Work developed during this PhD

This thesis has been carried out in the research group CITCEA-UPC, part of the Electrical Engineering Department of the Technical University of Catalonia. The work has been supported by a PFI grant from *Ministerio de Economia y competitividad* under the project *"Sistemas multiterminal de corriente continua en alta tension (HVDC) para la integracion de energias renovables en la red electrica"* with the project reference ENE2009-08555. Also, the author has collaborated in the industrial projects Vendaval II, developed for Alstom Wind and the research projects KIC InnoEnergy Smartpower and the project *"Sistemas de transporte electrico para grandes centrales eolicas marinas"* funded by *Ministerio de Economia y competitividad* the under the reference ENE2012-33043. Furthermore, the author has collaborated in the CIGRE working group B4-58 (Devices for Load Flow Control and Methodologies for Direct Voltage Control in a Meshed HVDC Grid) and has been a member of the Electrical Engineering Department Board, as student representative, and a member of the Technical Catalan Society (SCT-IEC) Board and President of the local PES-IEEE Barcelona's chapter.

Chapter 2

HVDC basic modelling and control

2.1 Introduction

This chapter presents the models and controls used throughout the thesis. These structures represent the state of the art in transistor-based vector control, especially focussing on HVDC systems. From the modelling point of view, the VSC average model and several AC and DC models are introduced, including

- Average power converter model
- DC grid models
  - Back-to-Back
  - HVDC Link (two terminal system)
  - MT-HVDC grid (four terminal, three line system)
- AC grid models
  - Inductive coupling filter (L) + Thevenin grid equivalent
  - Inductive-capacitive coupling filter (LC) + Thevenin grid equivalent

From the control point of view, the basic current control (or inner loop) for a VSC converter is explained. In addition, the possible outer control loop depending on their control propose is commented on, including:

- VSC basic control (AC Current loop and PLL)

- AC voltage generation (for offshore grid voltage generation)
- Proportional-Integral DC bus controller
- Droop DC bus controller
- Active power controller (for AC or DC sides)

2.2 VSC average model

Although the VSC converter is based on the discrete states of the switching of the IGBTs, for control design and power system analysis purposes it is convenient to derive a more simplified equivalent model. A simplified model can be derived by decoupling the DC and AC parts of the converter as illustrated in Figure 2.1 [14]. The DC side is modelled as a controlled current source, while the AC side is modelled with a three-phase AC voltage source. This models reflects the power converter behaviour at low frequencies, for this reason, this model is often called low frequency power converter model or average power converter model.

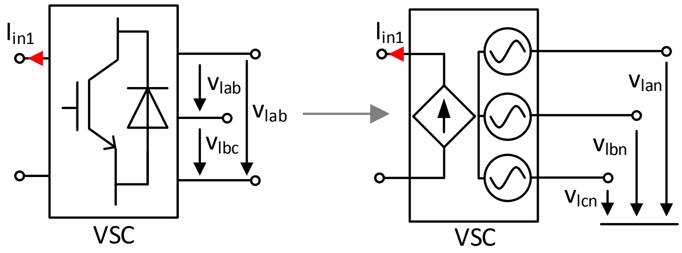

Figure 2.1: Voltage Source Converter average model

The current source in the DC side reflects the active power exchanged between the AC and the DC side and assures system power balance. The DC current of the source can be computed by neglecting converter losses as

$$I_{in1} = \frac{P_1}{E_1} \tag{2.1}$$

where I_{in1} is the current injected in the power converter DC side, E_1 is the DC side voltage and P_1 is the active power in the AC side.

2.3 AC grid coupling filter models

In order to avoid a shortcircuit between the VSC and the AC grid, the power converter cannot be directly connected. For this reason, a coupling filter is required. The most typical filters for HVDC applications are the L filter, but when a VSC is connected to a weak grid or an offshore wind farm a capacitor is needed in order to control the voltage. In this section the models of the L and LC filter are presented in the synchronous reference frame.

2.3.1 Park transformation

The electrical quantities in the *abc* frame are useful in a number of applications but has an oscillating nature. For the controller design it is useful to have constant quantities. This can be achieved by using the *Park transformation* [15] and the so-called Synchronous Reference Frame (SRF).

The Park transformation is given by

$$[x_{qd0}] = [T_{qd0}]\,[x_{abc}] \tag{2.2}$$

and its inverse

$$[x_{abc}] = [T_{qd0}]^{-1}\,[x_{qd0}] \tag{2.3}$$

where x_{abc} is a vector with the three-phase quantities in the *abc* frame and x_{qd0} is a vector with the transformed quantities in the $qd0$ frame.

The transformation matrix $T\left(\theta\right)$ can be written as

$$T\left(\theta\right) = \frac{2}{3}\begin{bmatrix} cos\left(\theta\right) & cos\left(\theta - \frac{2\pi}{3}\right) & cos\left(\theta + \frac{2\pi}{3}\right) \\ sin\left(\theta\right) & sin\left(\theta - \frac{2\pi}{3}\right) & sin\left(\theta + \frac{2\pi}{3}\right) \\ \frac{1}{2} & \frac{1}{2} & \frac{1}{2} \end{bmatrix} \tag{2.4}$$

and its inverse

$$T^{-1}(\theta) = \begin{bmatrix} cos\left(\theta\right) & sin\left(\theta\right) & 1 \\ cos\left(\theta - \frac{2\pi}{3}\right) & sin\left(\theta - \frac{2\pi}{3}\right) & 1 \\ cos\left(\theta + \frac{2\pi}{3}\right) & sin\left(\theta + \frac{2\pi}{3}\right) & 1 \end{bmatrix} \tag{2.5}$$

The Park transformation can be also seen as a geometric transformation which combines the Clarke transformation and a rotation. In this thesis the q-axis is related to the torque or the active power and the d-axis is related to the magnetizing current or reactive power depending on the application.

2.3.2 L coupling filter

The coupling inductance provides current smoothing for the current from/to the power converter. Figure 2.2 shows the model of a VSC to the AC grid by means of an inductive filter. Its dynamic equation representation is

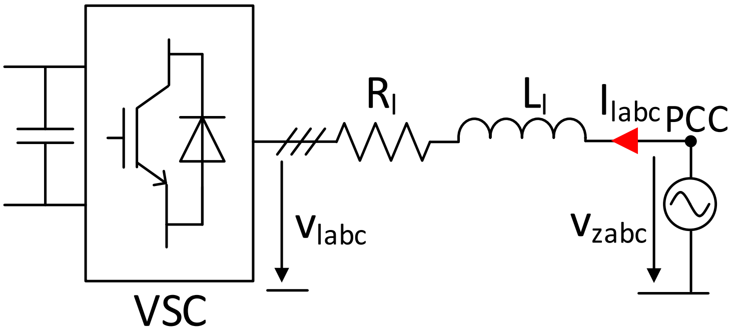

Figure 2.2: Model of a VSC connected to the AC grid by means of an L coupling filter

$$\frac{d}{dt}\begin{bmatrix} i_{lq} \\ i_{ld} \end{bmatrix} = \begin{bmatrix} -\frac{R_l}{L_l} & -\omega \\ \omega & -\frac{R_l}{L_l} \end{bmatrix} \begin{bmatrix} i_{lq} \\ i_{ld} \end{bmatrix} + \begin{bmatrix} -\frac{1}{L_l} & 0 & \frac{1}{L_l} & 0 \\ 0 & -\frac{1}{L_l} & 0 & \frac{1}{L_l} \end{bmatrix} \begin{bmatrix} v_{lq} \\ v_{ld} \\ v_{zq} \\ v_{zd} \end{bmatrix} \tag{2.6}$$

where v_{zqd} are the qd components of the voltage v_{zabc} at the PCC (Point of Common Coupling), $\underline{Z}_l = R_l + \jmath\omega L_l$ is the resistance and reactance of the coupling inductance, v_{lqd} is qd components of the voltage applied by the power converter, i_{lqd} is the current through the coupling filter and ω is the grid frequency.

2.3.3 LC coupling filter

The LC coupling filter provides voltage smoothing as well as current filtering. For modern HVDC power converters an inductive filter is theoretically enough, but when this power converter is facing to a weak grid or an offshore wind farm a capacitor near the converter is needed in order to control the AC voltage. Also, it is assumed that after the capacitor an inductive-based component is connected as a weak grid or a cable. Figure 2.3 presents the model of an LC filter.

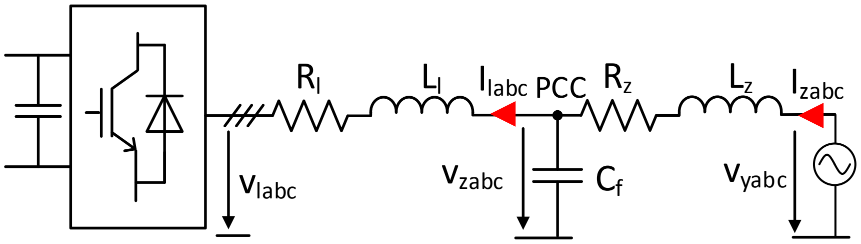

Figure 2.3: Model of a VSC connected to the AC grid by means of a LC coupling filter

The dynamic equation in the synchronous reference frame equations of an AC filter connected to an inductive element are

$$\dot{x}_{lc} = A_{lc}x_{lc} + B_{lc}u_{lc} \tag{2.7}$$

where A_{lc} and B_{lc} are

$$A_{lc} = \begin{bmatrix} -\frac{R_l}{L_l} & -\omega & \frac{1}{L_l} & 0 & 0 & 0 \\ \omega & -\frac{R_l}{L_l} & 0 & \frac{1}{L_l} & 0 & 0 \\ -\frac{1}{C_f} & 0 & 0 & -\omega & \frac{1}{C_f} & 0 \\ 0 & -\frac{1}{C_f} & \omega & 0 & 0 & \frac{1}{C_f} \\ 0 & 0 & -\frac{1}{L_z} & 0 & -\frac{R_z}{L_z} & -\omega \\ 0 & 0 & 0 & -\frac{1}{L_z} & \omega & -\frac{R_z}{L_z} \end{bmatrix} \tag{2.8}$$

$$B_{lc} = \begin{bmatrix} -\frac{1}{L_l} & 0 & 0 & 0 \\ 0 & -\frac{1}{L_l} & 0 & 0 \\ 0 & 0 & 0 & 0 \\ 0 & 0 & 0 & 0 \\ 0 & 0 & \frac{1}{L_z} & 0 \\ 0 & 0 & 0 & \frac{1}{L_z} \end{bmatrix} \tag{2.9}$$

and the state and input vectors are

$$x_{lc} = [i_{lq}\ i_{ld}\ v_{zq}\ v_{zd}\ i_{zq}\ i_{zd}]^T \tag{2.10}$$

$$u_{lc} = [v_{lq}\ v_{ld}\ v_{yq}\ v_{yd}]^T \tag{2.11}$$

where C_f is the shunt filter capacity, v_{yqd} are the qd components of the v_{yabc} voltage, i_{zqd} are the qd components of the current through the grid Thevenin equivalent model $\underline{Z}_z = R_z + \jmath\omega L_z$.

2.4 DC grid modelling

In this section the modelling of the DC grid is presented. As introduced in section 2.2, the VSC interacts in the DC grid as a current source. Therefore, the DC grid model inputs are currents. Transmission cables have been emulated using a π equivalent. First, the model of a VSC back-to-back structure is presented. After the two and four terminal models used for the MT-HVDC systems are introduced.

For the power transmission systems, as the power converter has an important amount of capacitance, it has been considered that the capacitance of the π equivalent cable is integrated into the converter capacity. Furthermore, the resistance and inductance of the positive and negative conductor is in only one impedance.

2.4.1 Back-to-back model

The back-to-back structure is one of the most-used configurations for VSC converters. It consist of the connection of two VSC for the DC side by means of a capacitor. It permits the connection of an electrical device to an AC grid eliminating the frequency dependency. For example, modern electrical drives as trains, or wind turbines use back-to-back structures to vary the rotational speed of the electrical machine without AC grid interactions. The same concept is applicable for high voltage systems, where HVDC back-to-back structures are used to connect asynchronous systems that work at different frequencies or the voltage angle difference is too large. Figure 2.4 shows a VSC Back-to-Back model, where its dynamic equation is

$$\frac{dE_1}{dt} = \begin{bmatrix} \frac{1}{C_1} & \frac{1}{C_1} \end{bmatrix} \begin{bmatrix} I_{in1} \\ I_{in2} \end{bmatrix} \tag{2.12}$$

where C_1 is the DC bus capacitor capacity.

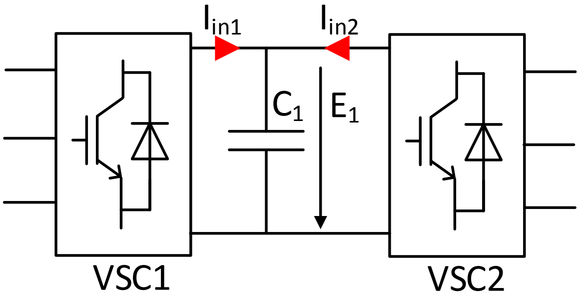

Figure 2.4: VSC Back-to-back model

2.4.2 Two terminal grid model

The two terminal grid for HVDC lines consists of two power converters connected by an cable or overhead line. This is the typical structure for HVDC links for onshore and offshore connections. Figure 2.5 shows the scheme of the modelled line.

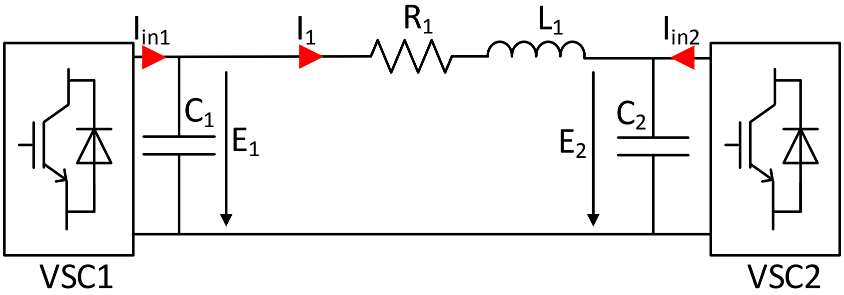

Figure 2.5: Two terminals DC grid modelled system

The dynamic equation of the two terminals scheme is

$$\frac{d}{dt}\begin{bmatrix} E_1 \\ I_1 \\ E_2 \end{bmatrix} = \begin{bmatrix} 0 & -\frac{1}{C_1} & 0 \\ \frac{1}{L_1} & -\frac{R_1}{L_1} & -\frac{1}{L_1} \\ 0 & \frac{1}{C_2} & 0 \end{bmatrix} \begin{bmatrix} E_1 \\ I_1 \\ E_2 \end{bmatrix} + \begin{bmatrix} \frac{1}{C_1} & 0 \\ 0 & 0 \\ 0 & \frac{1}{C_2} \end{bmatrix} \begin{bmatrix} I_{in1} \\ I_{in2} \end{bmatrix} \tag{2.13}$$

where R_1 and L_1 are the resistance and inductance value of the DC cable.

2.4.3 Four terminal grid

The four terminal scheme studied in this thesis consist of four power converters connected by means of three cables as is shown in Figure 2.6.

The dynamics equation of the four terminals scheme is

$$\dot{x}_{4t} = A_{4t}x_{4t} + B_{4t}u_{4t} \tag{2.14}$$

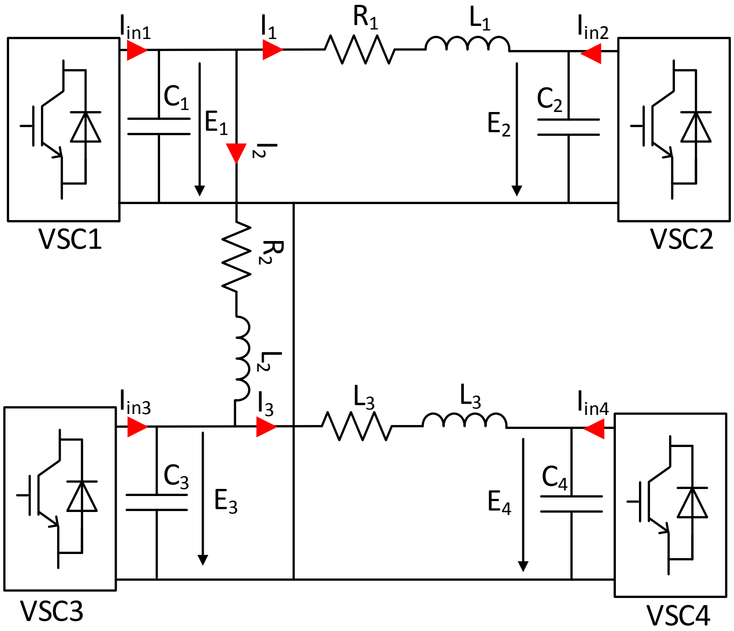

Figure 2.6: Four terminals DC grid modelled system

where the matrix gains are

$$A_{4t} = \begin{bmatrix} 0 & 0 & 0 & 0 & -\frac{1}{C_1} & -\frac{1}{C_1} & 0 \\ 0 & 0 & 0 & 0 & \frac{1}{C_2} & 0 & 0 \\ 0 & 0 & 0 & 0 & 0 & \frac{1}{C_3} & -\frac{1}{C_3} \\ 0 & 0 & 0 & 0 & 0 & 0 & \frac{1}{C_4} \\ \frac{1}{L_1} & -\frac{1}{L_1} & 0 & 0 & -\frac{R_1}{L_1} & 0 & 0 \\ \frac{1}{L_2} & 0 & -\frac{1}{L_2} & 0 & 0 & -\frac{R_2}{L_2} & 0 \\ 0 & 0 & \frac{1}{L_3} & -\frac{1}{L_3} & 0 & 0 & -\frac{R_3}{L_3} \end{bmatrix} \tag{2.15}$$

$$B_{4t} = \begin{bmatrix} \frac{1}{C_1} & 0 & 0 & 0 \\ 0 & \frac{1}{C_2} & 0 & 0 \\ 0 & 0 & \frac{1}{C_3} & 0 \\ 0 & 0 & 0 & \frac{1}{C_4} \\ 0 & 0 & 0 & 0 \\ 0 & 0 & 0 & 0 \\ 0 & 0 & 0 & 0 \end{bmatrix} \tag{2.16}$$

and the state and input vectors are

$$
\begin{aligned}
x_{4t} &= [E_1\ E_2\ E_3\ E_4\ I_1\ I_2\ I_3]^T && (2.17)\\
u_{4t} &= [I_{in1}\ I_{in2}\ I_{in3}\ I_{in4}]^T && (2.18)
\end{aligned}
$$

2.5 VSC basic control

The VSC allows us to control two electrical variables in the *qd* frame allowing us to control active and reactive power separately. content voltage at the PCC. Active power reference, in HVDC systems, it is adjusted to regulate the DC bus voltage and to ensure the power balance, i.e. the power injected into the grid has to be the same as the generated power.

The applied control scheme in this thesis is based on a two-level cascaded control system, the lower level controller allows us to regulate the AC current in the q and d components. This level is also known as current loop or inner loop and it is the basic control loop for a VSC. In HVDC applications, two possible control purposes can be found for the high level control:

- AC voltage creation: High level controllers focus on the creation of an AC grid side that dedicates both current components, i_{lqd}, to creating a new AC voltage with a preset angle and angular velocity. This control structure is used to create an AC grid in offshore wind farms.

- DC voltage control: High level controllers focused on the DC side dedicate a current component (i_{lq}) to regulate the DC voltage and ensure DC system stability. Furthermore, the other current component i_{ld} controls the voltage or the reactive power at the PCC. This is the typical control structure for VSC connecting DC systems with the main AC grid.

.

The controllers deal with currents and voltages in the *qd* reference frame rotating to adjust the electrical grid angle. For this reason, a Phase Locked Loop (PLL) to track the grid angle is required.

2.5.1 AC current control

In this section the control of the current through an L coupling filter is presented. The control objective is to control the i_{labc} current applying a voltage v_{labc} with the power converter. The plant equations are described in 2.3.2, where it is clear that there exist a coupling between the q and d components of voltages and currents. In order to control the i_{lq} and i_{ld} there are two main different control approaches:

- Multi-variable control, controlling the q and d components with a single two dimension controller.
- Decoupling and independently controlling q and d components.

The present text uses the second approach of decoupling and controlling i_{lq} and i_{ld} separately. Assuming that the control system is oriented with the d-axis component of the voltage at the PCC ($v_{zd} = 0$), the q and d components can be decoupled as

$$\begin{bmatrix} v_{lq} \\ v_{ld} \end{bmatrix} = \begin{bmatrix} -\hat{v}_{lq} + v_{zq} - l_l \omega i_{ld} \\ -\hat{v}_{ld} + l_l \omega i_{lq} \end{bmatrix} \tag{2.19}$$

where $\hat{v}_{lq}$ and $\hat{v}_{ld}$ are the outputs of the current controllers and v_{lq} and v_{ld} are the voltages to be applied by the converter. Substituting in 2.6

$$\begin{bmatrix} \widehat{v_{lq}} \\ \widehat{v_{ld}} \end{bmatrix} = \begin{bmatrix} R_l & 0 \\ 0 & R_l \end{bmatrix} \begin{bmatrix} i_{lq} \\ i_{ld} \end{bmatrix} + \begin{bmatrix} L_l & 0 \\ 0 & L_l \end{bmatrix} \frac{d}{dt} \begin{bmatrix} i_{lq} \\ i_{ld} \end{bmatrix} \tag{2.20}$$

Applying the Laplace transformation, the transfer function between the controller voltages and converter currents can be derived as

$$\begin{bmatrix} i_{lq}(s) \\ i_{ld}(s) \end{bmatrix} = \begin{bmatrix} \frac{1}{L_l s + R_l} & 0 \\ 0 & \frac{1}{L_l s + R_l} \end{bmatrix} \begin{bmatrix} \widehat{v_{lq}}(s) \\ \widehat{v_{ld}}(s) \end{bmatrix} \tag{2.21}$$

The controller can be designed using the Internal Model Control technique [16], resulting the following controller

$$K_{il}(s) = \frac{K_{p-il}s + K_{p-pl}}{s} \tag{2.22}$$

where the constants can be calculated as

$$K_{p-il} = \frac{L_l}{\tau_{il}} \tag{2.23}$$

$$K_{i-il} = \frac{R_l}{\tau_{il}} \tag{2.24}$$

where τ_{il} is the closed loop time constant of the electrical system. This constant must be chosen considering the converter physical restrictions. It is usual to define it a number of times (5-10 for example) slower than the converter switching frequency. The state-space representation of the inner loop controller using a PI controller is

$$\dot{x}_{il} = B_{il}u_{il} \tag{2.25}$$

$$y_{il} = C_{il}x_{il} + D_{il}u_{il} \tag{2.26}$$

where the matrix gains are

$$B_{il} = \begin{bmatrix} -1 & 0 & 1 & 0 & 0 & 0 \\ 0 & -1 & 0 & 1 & 0 & 0 \end{bmatrix} \tag{2.27}$$

$$C_{il} = \begin{bmatrix} K_{i-il} & 0 \\ 0 & K_{i-il} \end{bmatrix} \tag{2.28}$$

$$D_{il} = \begin{bmatrix} -K_{p-il} & 0 & K_{p-il} & -\omega L_l & 1 & 0 \\ 0 & -K_{p-il} & \omega L_l & K_{p-il} & 0 & 0 \end{bmatrix} \tag{2.29}$$

where the state variables, inputs and outputs are

$$x_{il} = [ei_{lq}\ ei_{ld}] \tag{2.30}$$

$$u_{il} = [i^*_{lq}\ i^*_{ld}\ i_{lq}\ i_{ld}\ v_{zq}\ v_{zd}] \tag{2.31}$$

$$y_{il} = [v_{lq}\ v_{ld}] \tag{2.32}$$

ei_{lqd} is the current error, defined as the difference between i^{*}_{lqd} (current reference) and i_{lqd}. The matrix gains are,

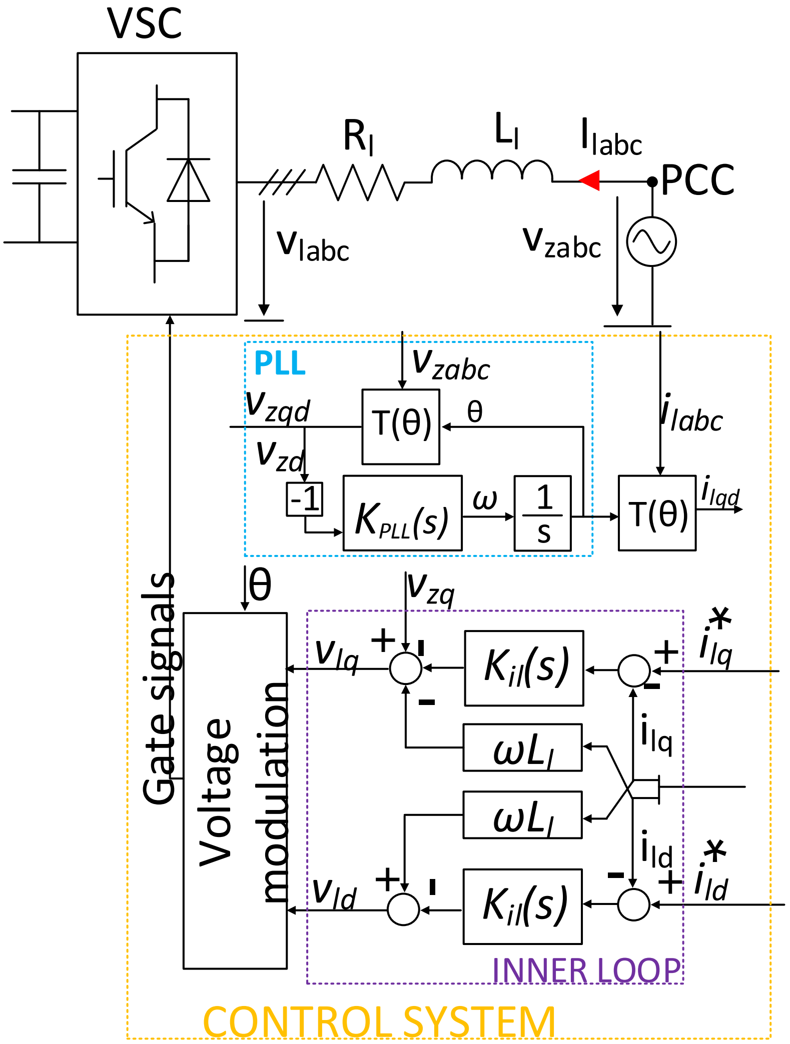

Figure 2.7: Scheme of the current control loop of a VSC connected to the AC grid by means of an L coupling filter

2.5.2 Phase Locked Loop

The PLL is required to extract the angle needed to synchronize the control system under the SRF. A classic scheme of a PLL is based on the d-axis voltage feedback by a PI controller to obtain the grid angular velocity and an extra integrator to obtain the angle. Figure 2.7 shows a representative scheme of the PLL integrated in the VSC control, which can be described as follows

$$K_{PLL}(s) = \frac{K_{p-pll}s + K_{i-pll}}{s} \tag{2.33}$$

where K_{p-pll} is the PLL proportional gain and K_{i-pll} is the PLL integral gain. According to [17] the PLL can be tuned as;

$$K_{p-pll} = \frac{2\xi_{pll}\omega}{\hat{V}_{za}} \tag{2.34}$$

$$K_{i-pll} = \frac{\omega^2}{\hat{V}_{za}} \tag{2.35}$$

where ξ_{pll} is the damping factor, $\hat{V}_{za}$ is the peak value of the v_{za} voltage. In [17] is suggested to choose a damping factor of $\xi_{pll} = 0.707$.

2.5.3 Current reference saturation

The currents references have to be limited according to the power converters current limit.

$$\mid I_{lqd}^{max} \mid = \sqrt{i_{lq}^2 + i_{ld}^2} \tag{2.36}$$

The limitation can be done differently depending on the priorities between active and reactive power, as two current component exist:

- Prioritizing i_q (active power) and providing only reactive power if there is enough available current.
- Prioritizing i_d (reactive power) and providing only active power if there is enough available current.

- Maintaining the angle between P and Q and reducing both of them equally.

In this thesis all the currents references are limited, but in order to simply the control schemes it is not drawn.

2.6 AC voltage creation

In this section the AC voltage controller to create an AC voltage for an offshore wind farm is described. This controller corresponds to a high level control that gives the current references to the low level control in order to obtain the desired AC voltage. The controller synthesis, structure and design is similar to the control structure presented in 2.5.3. First, the decoupling terms are introduced and after the controller tuning and the state-space representation are introduced. The controller decoupled structure is deduced from the equations of the v_{zqd} dynamics presented in 2.3.3 for a LC coupling filter, where the decoupling gains are

$$\begin{bmatrix} i_{lq} \\ i_{ld} \end{bmatrix} = \begin{bmatrix} -\hat{i}_{lq} - \omega C_f v_{zd} + i_{zd} \\ -\hat{i}_{ld} + \omega C_f v_{zq} + i_{zq} \end{bmatrix} \tag{2.37}$$

where $\hat{i}_{lq}$ and $\hat{i}_{ld}$ are the outputs of the voltage controllers. Substituting in 2.7,

$$\begin{bmatrix} \hat{i_{lq}} \\ \hat{i_{ld}} \end{bmatrix} = \begin{bmatrix} C_f & 0 \\ 0 & C_f \end{bmatrix} \frac{d}{dt} \begin{bmatrix} v_{zq} \\ v_{zd} \end{bmatrix} \tag{2.38}$$

Applying the Laplace transformation, the transfer function between the controller voltages and converter currents can be derived as

$$\begin{bmatrix} v_{zq}(s) \\ v_{zd}(s) \end{bmatrix} = \begin{bmatrix} \frac{1}{C_f s} & 0 \\ 0 & \frac{1}{C_f s} \end{bmatrix} \begin{bmatrix} \hat{i_{lq}}(s) \\ \hat{i_{ld}}(s) \end{bmatrix} \tag{2.39}$$

If IMC methodology is applied, the resulting controller is a proportional controller due to the integral effect of the capacitor, theoretically is not needed an extra integrator and the resulting controller is

$$K_{ol}(s) = K_{p-ol} \tag{2.40}$$

where K_{p-ol} is the proportional controller gain. It can be calculated as

$$K_{p-ol} = \frac{C_f}{\tau_{ol}} \tag{2.41}$$

where τ_{ol} is the desired close loop for the outer loop. note that this time constant should be between 3 and 5 times slower than τ_{il}. However, an integral part is added to the controller to improve the robustness in case of disturbances. The new controller is

$$K_{ol}(s) = \frac{K_{p-ol}s + K_{i-ol}}{s} \tag{2.42}$$

where the constants can be calculated as

$$K_{p-il} = 2C_f\xi_{ol}\omega_{ol} \tag{2.43}$$

$$K_{i-il} = C_f\omega_{ol}^2 \tag{2.44}$$

where ω_{ol} is the outer loop closed loop angular speed and ξ_{ol} is the damping factor. ω_{ol} should be tuned to be at least thee times slower than τ_{il}. Figure 2.8 shows an scheme of the overall controls scheme.

The state-space controller representation is,

$$\dot{x}_{ol} = B_{ol}u_{ol} \tag{2.45}$$

$$y_{ol} = C_{ol}x_{ol} + D_{ol}u_{ol} \tag{2.46}$$

where the state variables, inputs and outputs are

$$x_{ol} = [ev_{zq}\ ev_{zd}]^T \tag{2.47}$$

$$u_{ol} = [v_{zq}^*\ v_{zd}^*\ v_{zq}\ v_{zd}\ i_{zq}\ i_{zq}]^T \tag{2.48}$$

$$y_{ol} = [i_{lq}^*\ i_{ld}^*]^T \tag{2.49}$$

where the matrix gains are defined as

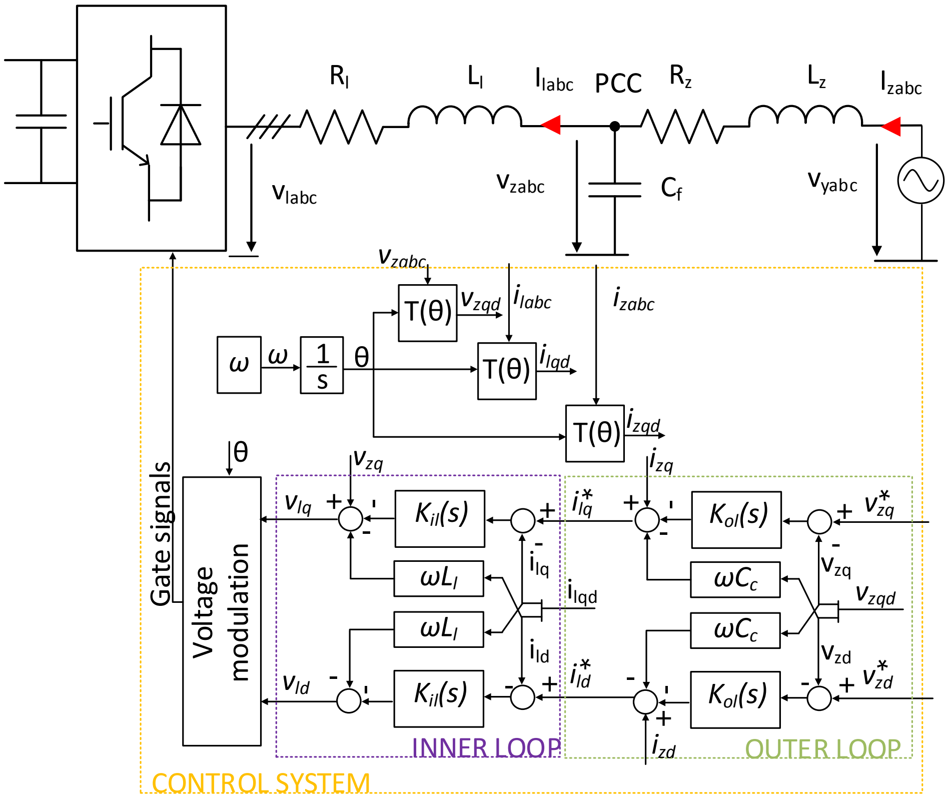

Figure 2.8: Scheme of the current and voltage control loop of a VSC connected to the AC grid by means of an LC coupling filter

$$B_{ol} = \begin{bmatrix} -1 & 0 & 1 & 0 \\ 0 & -1 & 0 & 1 \end{bmatrix} \tag{2.50}$$

$$C_{ol} = \begin{bmatrix} k_{i-ol} & 0 \\ 0 & k_{i-ol} \end{bmatrix} \tag{2.51}$$

$$D_{ol} = \begin{bmatrix} -k_{p-ol} & 0 & k_{p-ol} & -\omega C_f & 1 & 0 \\ 0 & -k_{p-ol} & \omega C_f & k_{p-ol} & 0 & 1 \end{bmatrix} \tag{2.52}$$

ev_{zqd} is the voltage error and v^*_{zqd} are the voltage references.

2.7 DC Voltage Control

The DC voltage regulator is required to control the voltage of the DC bus ensuring power balance between the incoming power to the DC grid and the power injected to the grid. The output of the DC voltage controller is provided the i_{lq}^* reference for the current loop. Several controllers can be used for HVDC systems [18] but the most predominant in the literature are the PI controller and a kind of proportional controller called Droop. PI controller is mainly used in HVDC links in order to control the DC voltage at a constant level, due to the integral gain that permits to have zero steady state error. Droop controller is suggested to be used [19] in MT-HVDC schemes and DC grids. The purpose of the droop control is to ensure an adequate power transmission and it should be decentralized so that the control law applied by an HVDC converter only depends on local measurements made by that converter and does not need to rely on long distance communications between different terminals. The common formulation of this controller is the so-called droop control concept [20]. The droop controller is a proportional control law that regulates the DC voltage and provides power sharing between the different power converters.

The output of the DC voltage controller is the current that should be injected by the VSC in the DC side, I_{in1}^*, but for the inner loop an AC current reference is needed. I_{in1}^* can be transformed to i_{lq}^* AC reference as

$$I_{lq}^* = \frac{2I_{in1}^* E_1}{3v_{zq}} \tag{2.53}$$

2.7.1 PI Controller design

The PI-based controller is exemplified in the case of a DC bus voltage regulator design for the VSC1 converter of back-to-back connected to the grid by means of an L coupling filter presented in subsection 2.4.1, but it can be extended in the other presented schemes [21]. Figure 2.9 shows and scheme of the DC voltage control implementation. From equation 2.12 is deduced the following decoupling structure

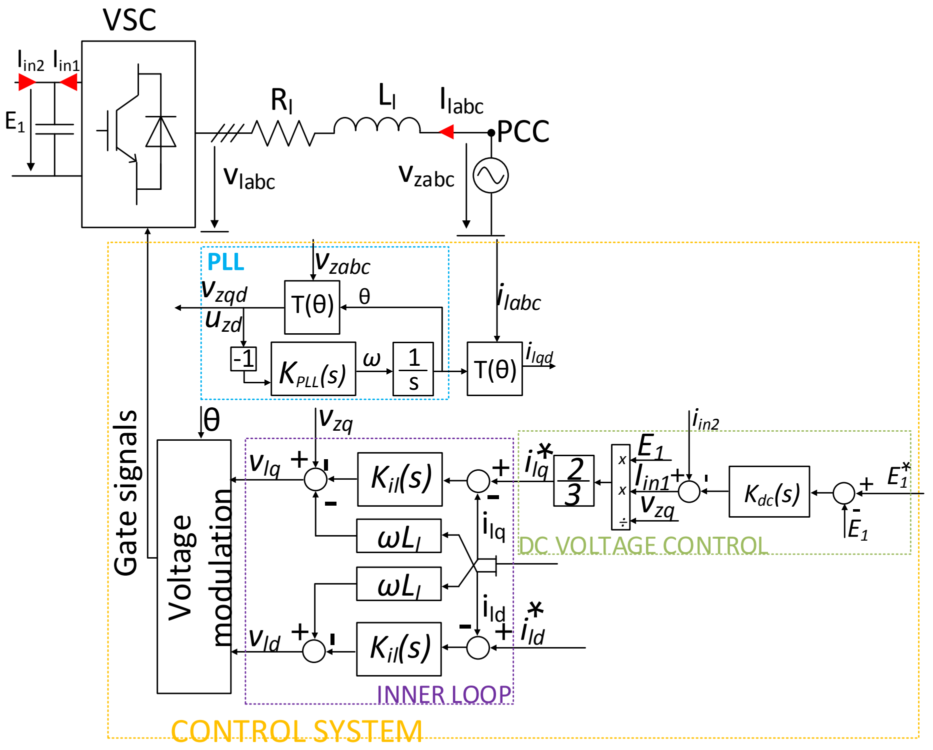

Figure 2.9: Scheme of the DC voltage and current control loop of a VSC connected to the AC grid by means of an L coupling filter

$$I_{in1} = \hat{I}_{in1} - I_{in2} \tag{2.54}$$

where $\hat{I}_{in1}$ is the voltage controller output. Substituting in equation

$$\hat{I}_{in1} = C\frac{dE_1}{dt} \tag{2.55}$$

Applying the Laplace transformation the transfer function between the controlled current and the E_1 voltage is

$$E_1(s) = \frac{1}{C_1 s}\hat{I_{in1}}(s) \tag{2.56}$$

Applying the IMC methodology, the resulting controller is a proportional controller

$$K_{dc}(s) = K_{p-dc} \tag{2.57}$$

where K_{p-dc} is the proportional controller gain. It can be calculated as

$$K_{p-dc} = \frac{C_1}{\tau_{dc}} \tag{2.58}$$

where τ_{dc} is the desired close loop for the DC voltage loop. Note that this time constant should be between 3 and 5 times slower than τ_{il}. To enhance the system performance an integral gain is added. The new controller is

$$K_{dc}(s) = \frac{K_{p-dc}s + K_{i-dc}}{s} \tag{2.59}$$

where the constants can be calculated as

$$K_{p-dc} = 2C_1\xi_{dc}\omega_{dc} \tag{2.60}$$

$$K_{i-dc} = C_1\omega_{dc}^2 \tag{2.61}$$

where ω_{dc} is the outer loop closed loop angular speed and ξ_{dc} is the desired damping factor. ω_{dc} should be tuned to be at least three times slower than τ_{il}.

2.7.2 Droop controller design

Different implementations have been suggested for the droop control, mainly current or power based can be found in the literature [22]. In this thesis the current-based implantation is used. Figure 2.10 shows the DC voltage droop implementation. It is described as

$$I_{in}^* = k_{droop}(E_1 - E_1^*) \tag{2.62}$$

Regarding the controller design, it has been addressed in different papers.

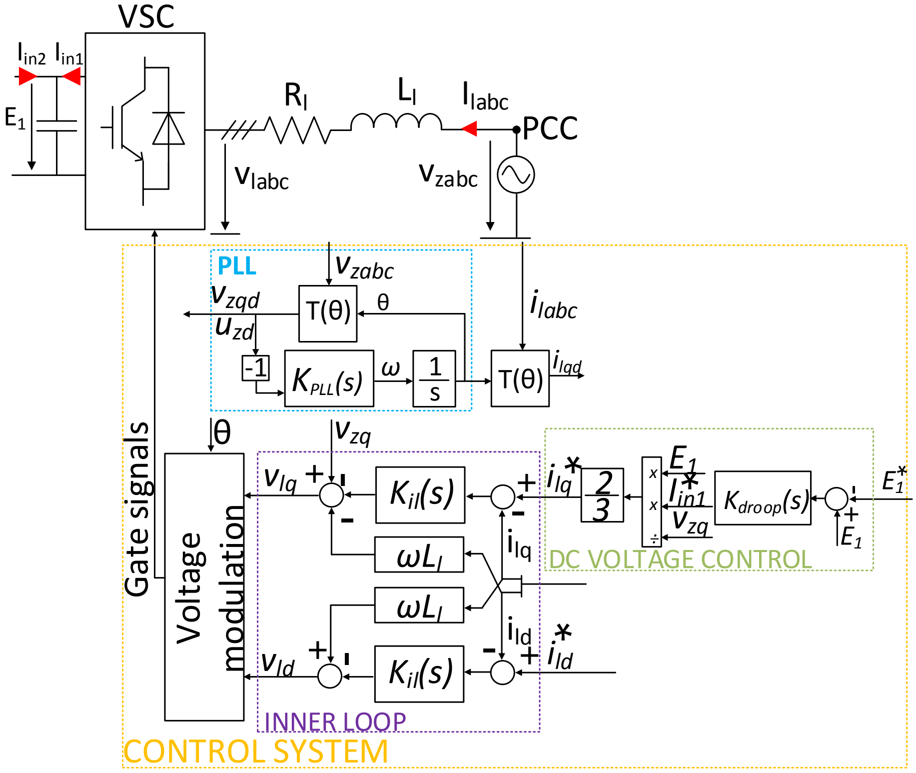

Figure 2.10: Scheme of the DC voltage droop implementation with a current control loop and a voltage loop of a VSC connected to the AC grid by means of an LC coupling filter

In [23], the controller tuning is based on the steady state characteristics and the resulting power flow sharing [24]. In [25] the influence of the DC grid dynamics and DC grid operational limitations are considered during the design stage. In this thesis the methodology introduced in [25] is used.

2.8 Others outer loop approach

Another proposed outer loop approach is proposed for power converters that do not regulate the DC voltage or the DC voltage controller is a power-based controller. This outer loop calculates the current reference component i_{lqd} in order to obtain the desired active power (P) and the amplitude of the voltage at the PCC (V_z) (alternatively the power at the DC side). A classic approach to the upper-level control consists of two independent PI controllers, one for each current component. Further details can be seen in [26]. A scheme of the aforementioned method is depicted in Figure 2.11.

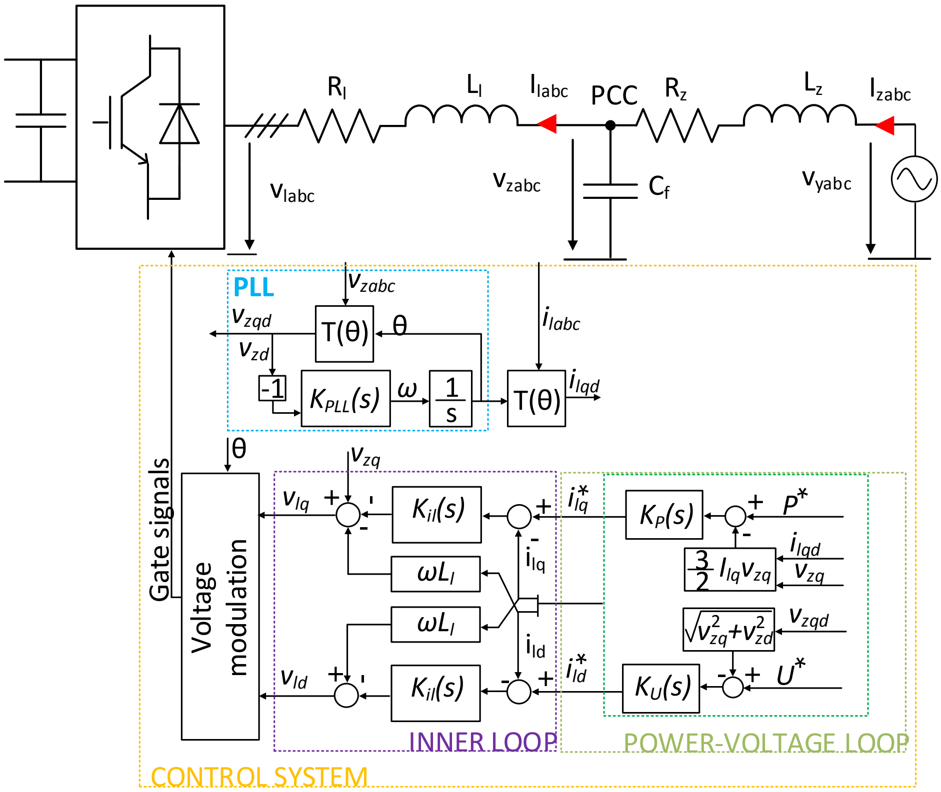

Figure 2.11: Scheme of the DC voltage droop implementation with a current control loop of a VSC connected to the AC grid by means of an LC coupling filter

The upper level controls is described as

$$i_{lq}^{*} = K_P(s)(P^{*} - P) \tag{2.63}$$
$$i_{ld}^{*} = K_U(s)(U^{*} - U) \tag{2.64}$$

where K_P and K_U are defined as

$$K_P(s) = \frac{k_{p-p}s + k_{i-p}}{s} \tag{2.65}$$

$$K_U(s) = \frac{k_{p-u}s + k_{i-u}}{s} \tag{2.66}$$

where k_{p-p} and k_{p-u} are the proportional gains and k_{i-p} and k_{i-u} are the integral gains for the active power and voltage controllers.

Chapter 3

MT-HVDC system operation

In this chapter, the steady-state operation characteristics of an MT-HVDC system based on droop DC voltage control for a four terminal and three lines system are described. These characteristics are defined according to VSC control and the power converter maximum current and voltage.

3.1 Studied multiterminal scheme

The system under analysis is an MT-HVDC transmission system [27] with four terminals: two offshore wind farms and two onshore main AC grid connections (see Figure 3.1). The two offshore wind farm VSC (WFC) power converters inject the power generated in each wind farm into the HVDC grid whereas the grid side VSC (GSC) power converters inject the power from the HVDC grid into the main AC grid. The HVDC grid consists of three submarine cables: two of them connect each wind farm to an onshore VSC while a third tie cable connects the two wind farms together in order to provide redundancy and share the power injected by each onshore converter.

3.2 MT-HVDC operation

During normal operation mode, the WFCs inject all the generated current into the HVDC grid while the GSCs maintain the DC voltage almost constant by means of the droop control law given by

$$I_{ink}^{*} = K_{droopk}(E_k - E_k^{*}), \quad k = 3, 4, \tag{3.1}$$

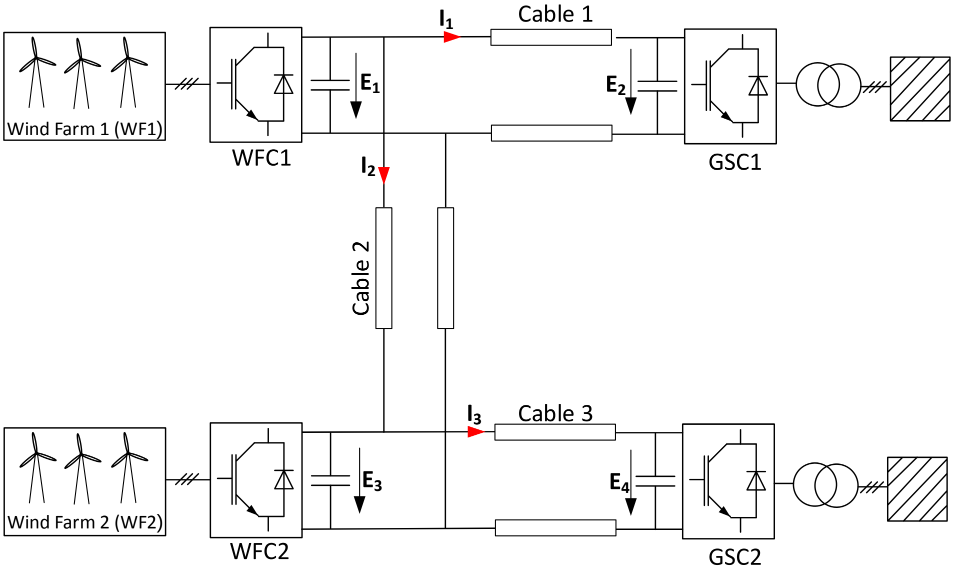

Figure 3.1: General scheme of the system studied

where I^*_{ink} and E_k are the DC current and the DC voltage in the converter k, respectively, K_{droopk} is the droop gain and E^*_k is a set-point voltage.

During severe terrestrial grid faults, the GSCs may not be capable of transferring all the power coming from the WFC into the terrestrial grid as the AC current needed would exceed the rating of the GSCs. In such conditions, the GSCs enter current limitation mode, extracting only a constant current value. If the power injected from the wind farm side is higher than the power extracted for the grid side, the voltage of the HVDC grid would start to increase as a result of the power imbalance. This behavior is illustrated by static current-voltage curve in Figure 3.2. The current limitation mode corresponds to the hyperbola and line to normal operation (when the droop control is applied), where V_{AC} is the AC voltage. Notice that the maximum current I_{gsH} that can be extracted by the GSCs depends on the AC grid voltage, thus for a 50% voltage drop in the AC grid, the maximum current would drop by 50%.

In order to prevent the DC voltage from increasing beyond the allowed limits, the WFCs must also switch their operating mode to power reduction mode when the DC voltages reach the limits E_{wfL}. Thus, the WFCs reduce

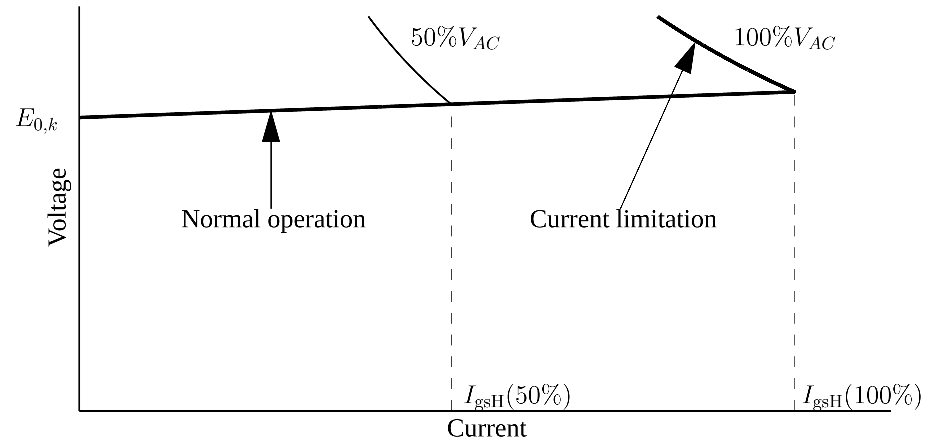

Figure 3.2: Static current-voltage characteristic of a GSC. The thin line shows the characteristic under a voltage sag of 50%

the power injected into the HVDC grid by using a droop control law

$$I_{in}^{*} = -K_{droopk}(E_k - E_k^{*}), \quad k = 1, 2. \tag{3.2}$$

The static current-voltage for WFCs is illustrated in Figure 3.3. The two operating regions of the WFCs can be seen: droop power reduction and normal operation (power injection). In addition, the WFCs also present a current limitation mode to set the current at I_{wfH} in case of an excess of power coming from the wind turbines. A implementation of the WFCs control can be seen in [28].

The controller adaptation is done automatically by the converters obeying static voltage-current characteristics as illustrated in the previous figures [20]. The droop gains K_{droopk} must be designed in order to ensure stability and performance under any possible operating modes and also during the transitions between them. That means that the decentralised control law must ensure stability and performance for a time-varying system.

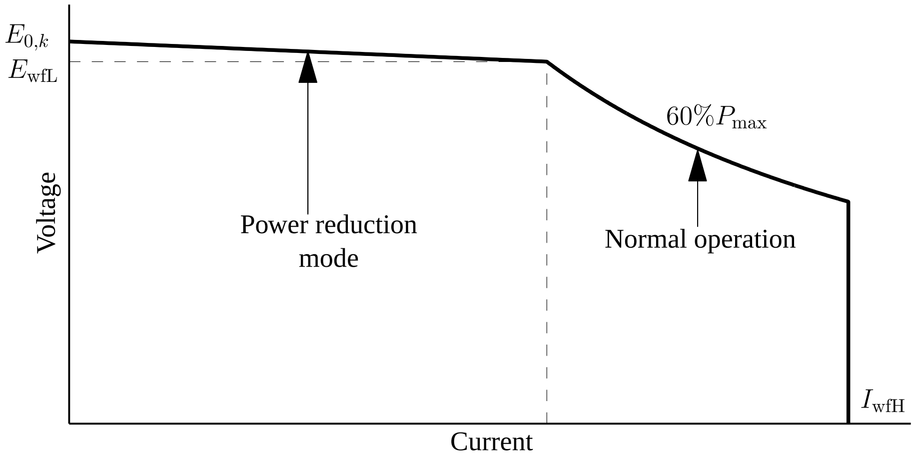

Figure 3.3: Static current-voltage characteristic of a WFC

Chapter 4

MT-HVDC experimental development and validation

In this chapter, the design of an MT-HVDC experimental platform and the verification of the system by means of simulations are addressed. First, the platform design and performance is widely discussed. The electrical part has been built using electrical hardware (converters, electrical machines) and the wind turbine aerodynamics is emulated via a PC. Furthermore, all the electrical and mechanical variables are supervised using an SCADA system. The aerodynamics emulation and the SCADA are installed on a PC. The PC collects all the variables status from the system and sends the wind references by means of a DAQ system. Some tests regarding the voltage control and wind farm emulation have been carried out and compared with the simulation results.

4.1 Developed experimental platform

An experimental platform has been designed in order to test and verify the control and operation of HVDC systems. The developed setup emulates the behaviour of the system described in Section 3.1. The system consist of four VSC converters connected in the DC side by means of a DC grid. The wind farm is emulated using a squirrel cage induction motor which is mechanically coupled to a squirrel cage induction generator which is connected to the wind farm VSC. A photograph and a scheme of the system can be seen in Figure 4.1 and Figure 4.2.

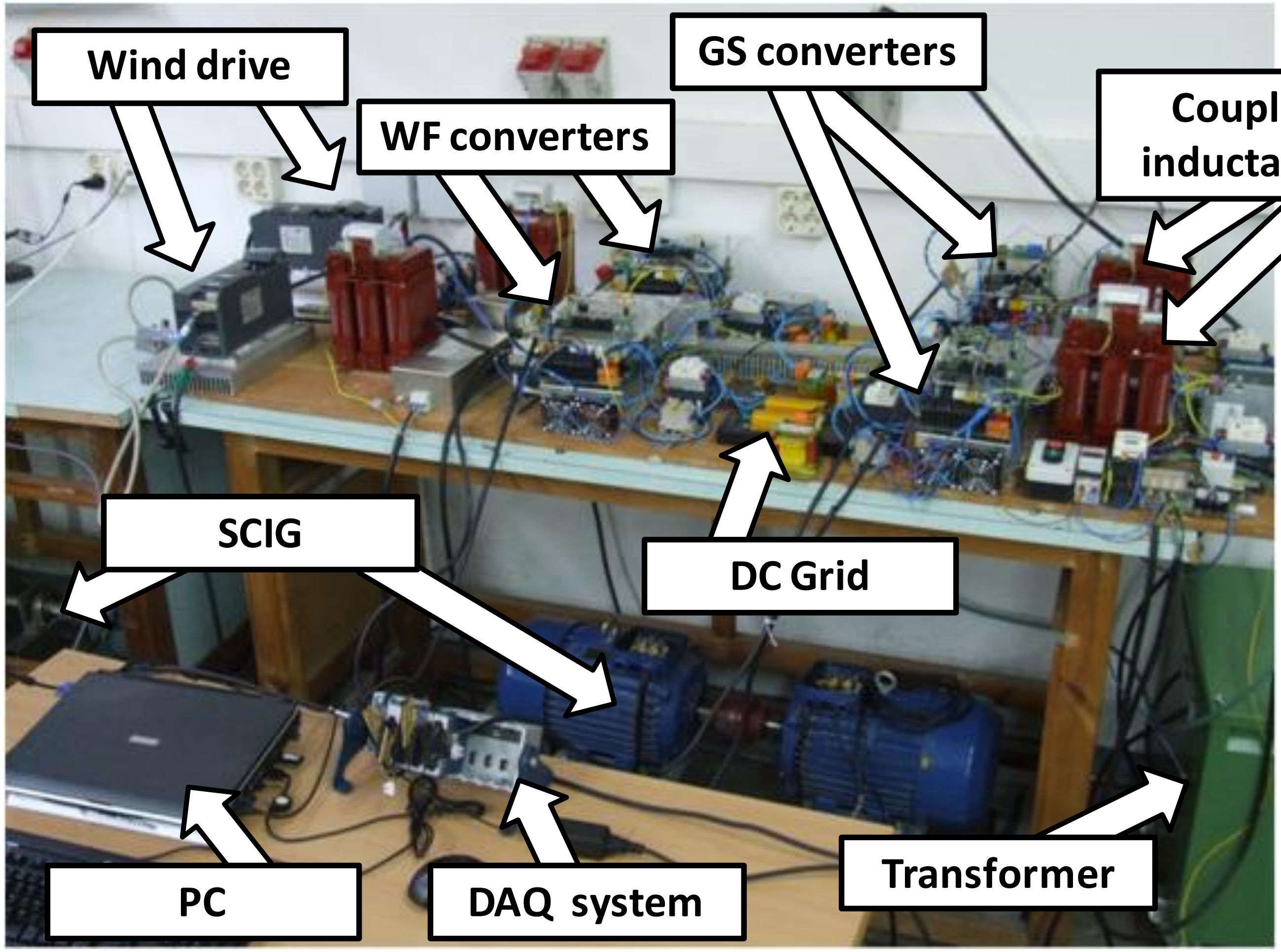

Figure 4.1: Photograph of the experimental platform

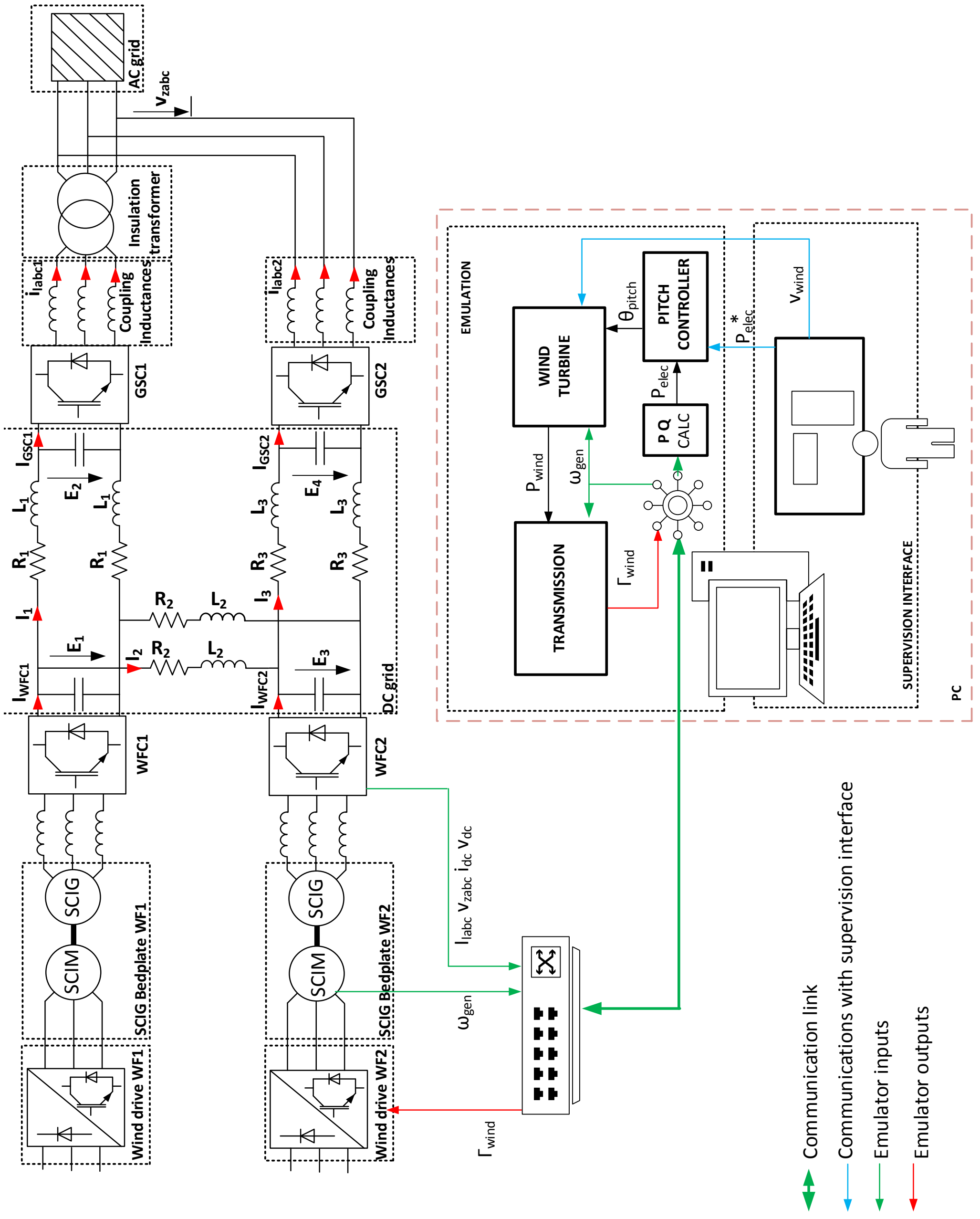

Figure 4.2: Scheme of the experimental platform

4.1.1 Power converter

The VSC power converter used is a two-level converter based on IGBTs (Insulated Gate Bipolar Transistors). The whole device is composed of three boards: the power board, the drivers board and the control board. The control board is based on a Texas instrument Digital Signal Processor (DSP) TMS320F2808. DSP interacts with the IGBTs by means of a driver board that provides the necessary gate-excitation signals also introducing the dead-time. In addition, the drivers board has analogue-based protection, which disconnects the power converter in case of excess current, overheating, excess voltage or driver error. Each grid side power converter is connected to the AC grid by means of an inductance. Nominal values of the system can be seen in Table 4.1.

Characteristic	Value
Nominal DC Voltage	800 V
Nominal AC current	15 A
Maximum switching frequency	20 kHz
Coupling Inductance	4.6 mH

Table 4.1: Parameters of power converter characteristics

The power board is composed by a module of three legs of IGBT's with an additional branch to provide brake capability. The available measurements include two AC voltages, two AC currents and the DC current and voltage. Furthermore, an AC switch allows to connect the power converter once it is synchronised with the AC grid. A DC switch allows to connect each power converter with the other converters of the experimental setup. The power board elements are sketched in Figure 4.3.

4.1.2 Wind farm emulation

Squirrel cage induction machines (SCIM) have been used to emulate the wind farm. Each wind farm is emulated by a SCIM which is mechanically coupled to a squirrel cage induction generator which is connected to the wind farm VSC. The SCIM that emulates the wind farm is driven by a commercial converter with torque control capability. The wind farm VSC is

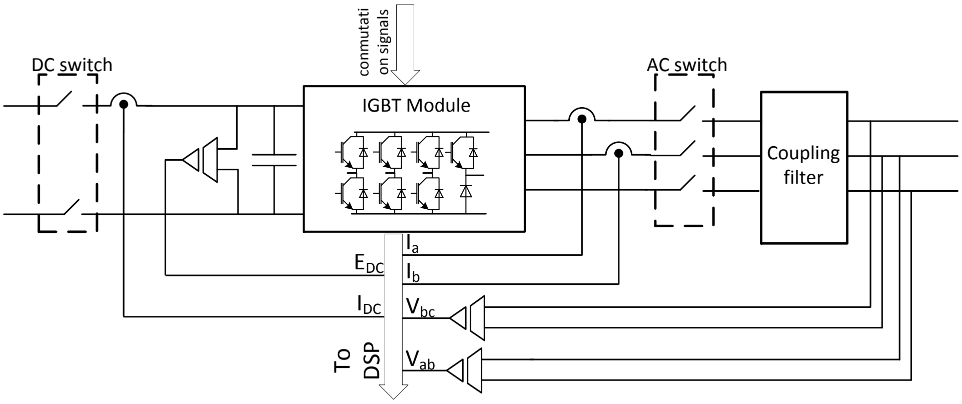

Figure 4.3: Scheme of the power board

based on the power converter previously described where the control scheme is implemented. The characteristics of the SCIG machines used can be seen in 4.2.

Characteristic	$WF1$	$WF2$
Nominal power	2200 W	7500 W
Nominal speed	1470 min^{-1}	1465 min^{-1}

Table 4.2: Parameters of wind farm emulation SCIM

WFC rectifies all the generated power to the grid, but when the wind is blowing above the nominal speed the wind turbine must reduce the wind captured from the wind. This power reduction method is achieved by means of increasing the pitch angle.

4.1.3 DC Grid

Transmission cables have been emulated using a π equivalent. As the power converter has an important amount of capacitance, it has been considered that the capacitance of the π equivalent cable is integrated into the converter capacitance. An inductance and a resistance have been added to emulate each cable as shown in Table 4.3.

The experimental platform has been scaled according to the following

Cable	Inductance	Resistance
Cable 1 (from WFC1 to GSC1)	1 mH	0.22 Ω
Cable 2 (from WFC1 to WFC2)	0.5 mH	0.1 Ω
Cable 3 (from WFC2 to GSC2)	1.5 mH	0.44 Ω

Table 4.3: Parameters of DC grid

criteria. The DC capacitance for each VSC converter has been chosen to maintain the time constant $\tau_{wp} = W/P$ as in the simulated system, where $W = \frac{1}{2}CE_{dc}^2$ and P is the converter nominal power. The obtained τ_{wp} for both cases is 22.5 ms. For the selected capacitance, the line inductances have been chosen to obtain the same resonance frequency as in the simulations. For example, in cable 1 the resonance frequency obtained is of 157.59 Hz for both cases. The line resistance have been chosen to maintain the $\tau_{lr} = L/R$ time constant. For example, in cable 1 the time constant τ_{lr} yields 4.5 ms for both cases. Furthermore, the controls have been tuned considering the same time constants.

4.2 Aggregated wind farm emulation

In the lower part of Figure 4.2 the implemented aggregated model of the aerodynamic and mechanical part of the wind power farm can be seen . In this case, the emulated wind farm consist of a Squirrel Cage Wind Turbine power plant where the electrical frequency is fixed by the WFC and the wind drives produce wind equivalent torque.

The mechanical part of the wind turbine has been modelled as a power source, where the inputs are the wind speed, the pitch angle and the angular velocity of the wind turbine.

$$P_{wind} = \frac{1}{2}\rho c_p A v_{wind}^3 \tag{4.1}$$

where ρ is the air density, c_p is the power coefficient, A is the swept wind turbine area, and v_{wind} is the wind speed. The c_p varies in function of the wind turbine aerodynamics and is particular for a wind turbine type. The c_p is a non-linear function defined as

$$C_p = c_1(c_2\frac{1}{\Lambda} - c_3\beta - c_4\beta_4^c - c_6)e^{-c_7\frac{1}{\Lambda}} \tag{4.2}$$

$$\frac{1}{\Lambda} = \frac{1}{\Lambda + c_8\beta} - \frac{c_9}{1+\beta^3} \tag{4.3}$$

$$\lambda = \frac{\omega_m R}{v_{wind}} \tag{4.4}$$

where ω_m is the rotational speed of the wind turbine, β is the pitch angle and $c_1 ... c_9$ are the wind turbine power coefficients. The wind turbine inertia is considered in order to smooth the torque that is sent to the wind drive as

$$\Gamma_{wind}(s) = \frac{1}{J_{wt}s+1}\frac{P_{wind}}{\omega_m}(s) \tag{4.5}$$

where J_{wt} is the system inertia.

4.3 System supervision and monitoring

The system is supervised by means of a LABVIEW SCADA that resides in the same computer as the wind emulation structure. Figure 4.4 shown an screenshot of the electrical variables of the GSC1. The SCADA is used to monitor the electrical variables, DC and AC current and voltages, of the GSC1, GSC2, WFC1 and WFC2 and the mechanical variables as, the rotational speed, pitch angle and torque of wind farm 1 and 2. Furthermore, the user can select the desired wind speeds for both wind farms.

4.4 MT-HVDC experimental validation

An experimental validation has been conducted to evaluate the system operation and the droop control strategy. Furthermore, the emulated results have been compared with the simulated results. The following cases have been analysed:

1. Wind farm power change

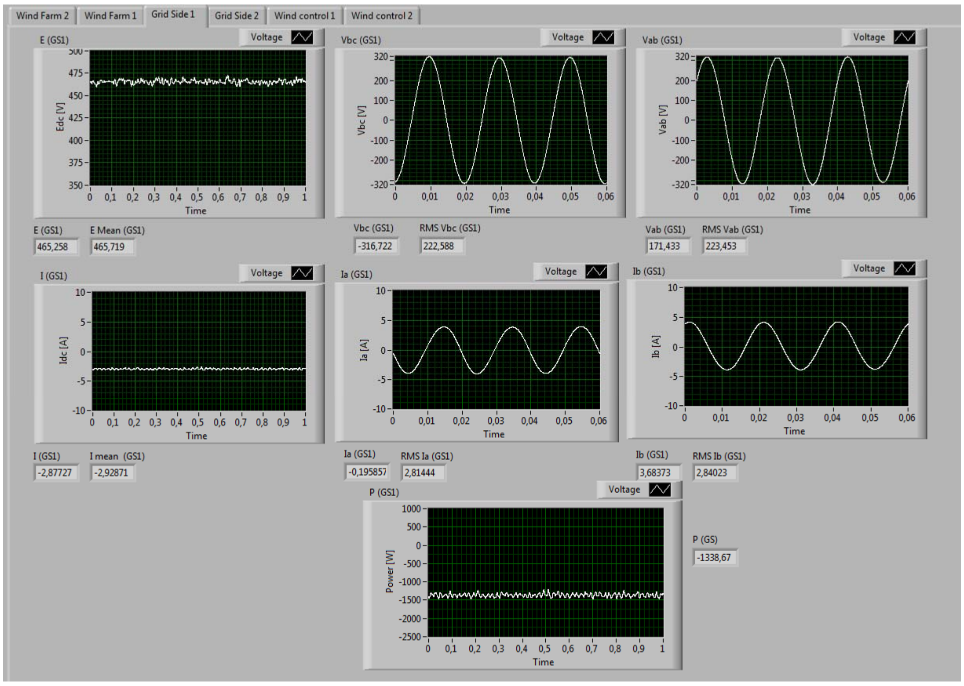

E (GS1) 465,258
E Mean (GS1) 465,719
Vbc (GS1) -316,722
RMS Vbc (GS1) 222,588
Vab (GS1) 171,433
RMS Vab (GS1) 223,453
I (GS1) -2,87727
I mean (GS1) -2,92871
Ia (GS1) -0,195857
RMS Ia (GS1) 2,81444
Ib (GS1) 3,68373
RMS Ib (GS1) 2,84023
P (GS) -1338,67

Figure 4.4: SCADA screenshot for the GSC1

2. Grid side converter disconnection
3. Wind farm converter disconnection

4.4.1 Wind power change case

In this case, the power in the WF2 changes whereas the power in WF1 remains constant. In this situation, the multiterminal grid works in normal operation. During this operation mode, only the droop controls in both grid side converters are active in order to regulate the DC voltages and ensure adequate transmission of the power generated in the wind farms.

Figure 4.5 shows the voltages and currents at each extreme of the experimental DC grid. When the wind speed is increased, more incoming current is injected to the MT-HVDC system, consequently, the DC voltage starts to rise and more power is injected to the AC grid. It can be observed that the droop control is able to maintain the voltage within the range of 10% error with highly damped behaviour. Figure 4.5 shows the current in both GSC increases in the same proportion to extract the increase of the power coming from the WF2. Once the wind speed has returned to its previous level the system returns to work in the previous operation point. The power at each node of the multiterminal DC grid and the AC currents of the GSC2 can be seen in Figure 4.6. As the voltages remain almost constant during the power increase, the evolutions of the currents are similar to the current ones in Figure 4.5.

4.4.2 Grid side disconnection case

The second case analysed corresponds to the disconnection of GSC1 while both wind farm converters remain injecting the same power level.

Figure 4.7 shows the DC voltages and currents at each extreme of the multiterminal grid. It can be observed that the currents in WFC1 and WFC2 are nearly constant whereas the current in GSC1 falls suddenly to zero at 0.5 s. The current in GSC2 increases to extract the sum of the currents coming from the WFCs. As a consequence of the disconnection of GSC1, all the generated power must be extracted by the GSC1. For this reason, the voltage in GSC1 E_2 increases rapidly in order to increase I_{GSC1} and thus maintaining I_{WFC1} and I_{WFC2} almost constant. The wind power generation does not change during the disconnection.

In Figure 4.8, the power in each converters and the AC current in GSC2 can be seen. Again, the power evolutions are similar to the DC currents because the voltage changes are small.

4.4.3 Wind farm converter disconnection

In the last case, the WFC1 is disconnected whereas the WFC2 remains injecting the same power level. As a result of the disconnection, the total power injected into the multiterminal grid reduces suddenly. Figure 4.9 presents the DC voltages and currents in each converter. It can be observed that current in the WFC1 fall to zero and the voltages decrease in all nodes. The droop control causes a reduction of the voltages which permits to decrease the currents extracted by each GSCs and thus maintaining the power balance. It is interesting to note that the responses are well damped as in previous cases, the current overshoots observed in Figure 4.9 are caused by the implementations of the disconnection of the WFC1. Power and AC currents are shown in Figure 4.10.

4.5 Wind farm emulation experimental validation

An emulated case has been done in order to test and check the control scheme and the experimental platform performance. In this case, a wind speed change has been carried out in the WF1. In order to make the experiment more understandable a wind farm has been connected only. Figure 4.11 shows the wind speed profile that changes from 11.1 m/s to 13.1 m/s, above the nominal wind speed, at time instant 2.8 s.

Figure 4.12 shows the evolution of the DC voltage and current and the electrical power respectively at the power converters. Before the step change the WF was injecting a power of about $0.55p.u.$ This power was shared between the two power converters as their droop controller has been tuned with the same droop constant. The small difference between the two injected power is due to the different DC cable impedances. As the system is transmitting the wind farm generated power,the DC grid voltage on the wind farm side is higher than in the grid side. At time $t = 2.8$ s the wind step up is produced and the system starts to generate more power. According to the droop control, as more power is injected to the grid the DC voltage is increased in order to inject more AC current. The dynamics of the injected current to the DC grid are fixed by the wind turbine dynamics. Once the system achieves the nominal power the pitch controller starts to react and the pitch angle is increased, consequently, the power extracted from the wind is decreased and maintained constant at 1pu. Due to the slow pitch dynamics there is an small power overshot.

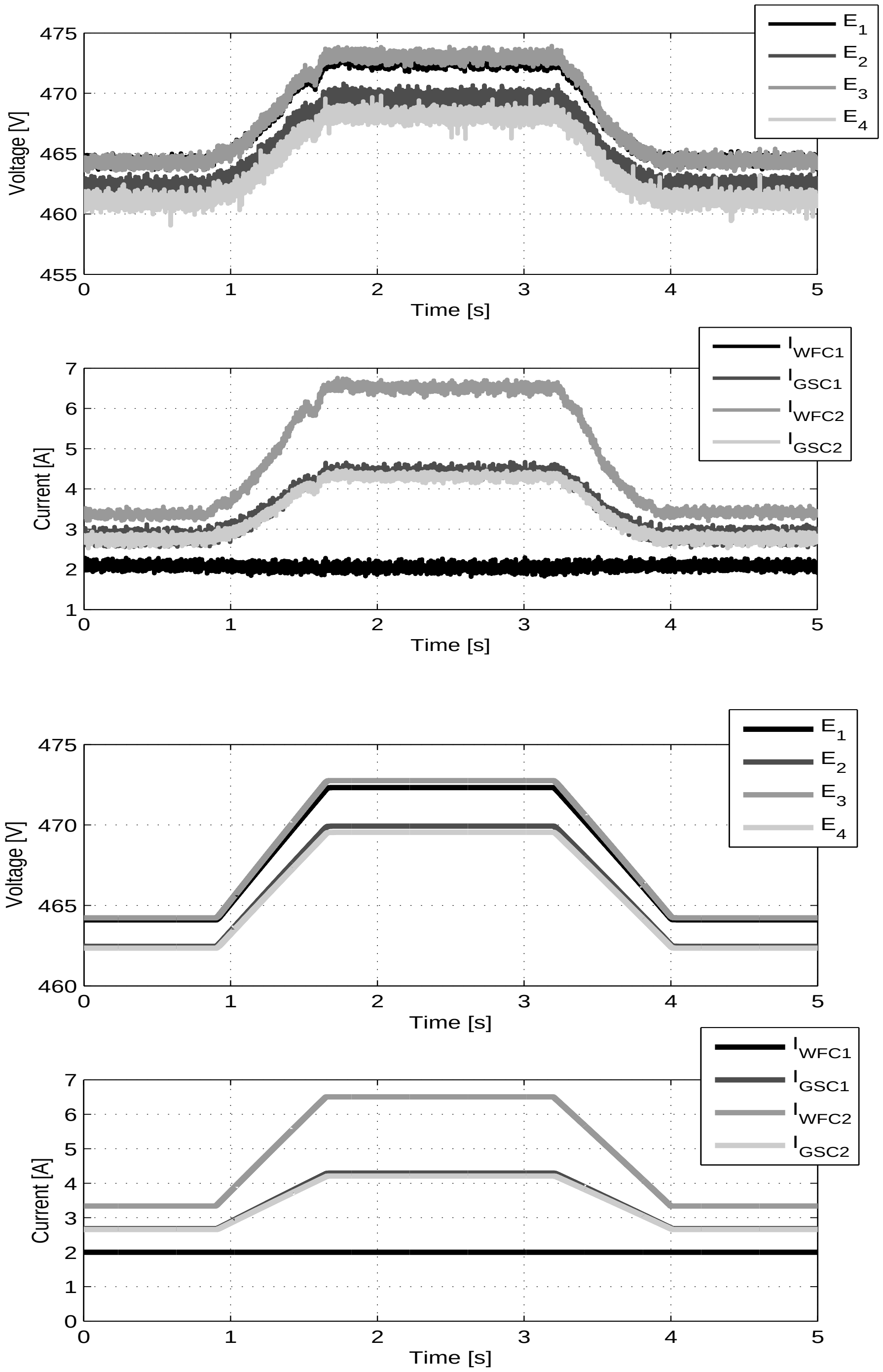

Figure 4.5: DC Voltages and currents during a change in the power reference at the WF2 (Real system: left, Simulated system: Right)

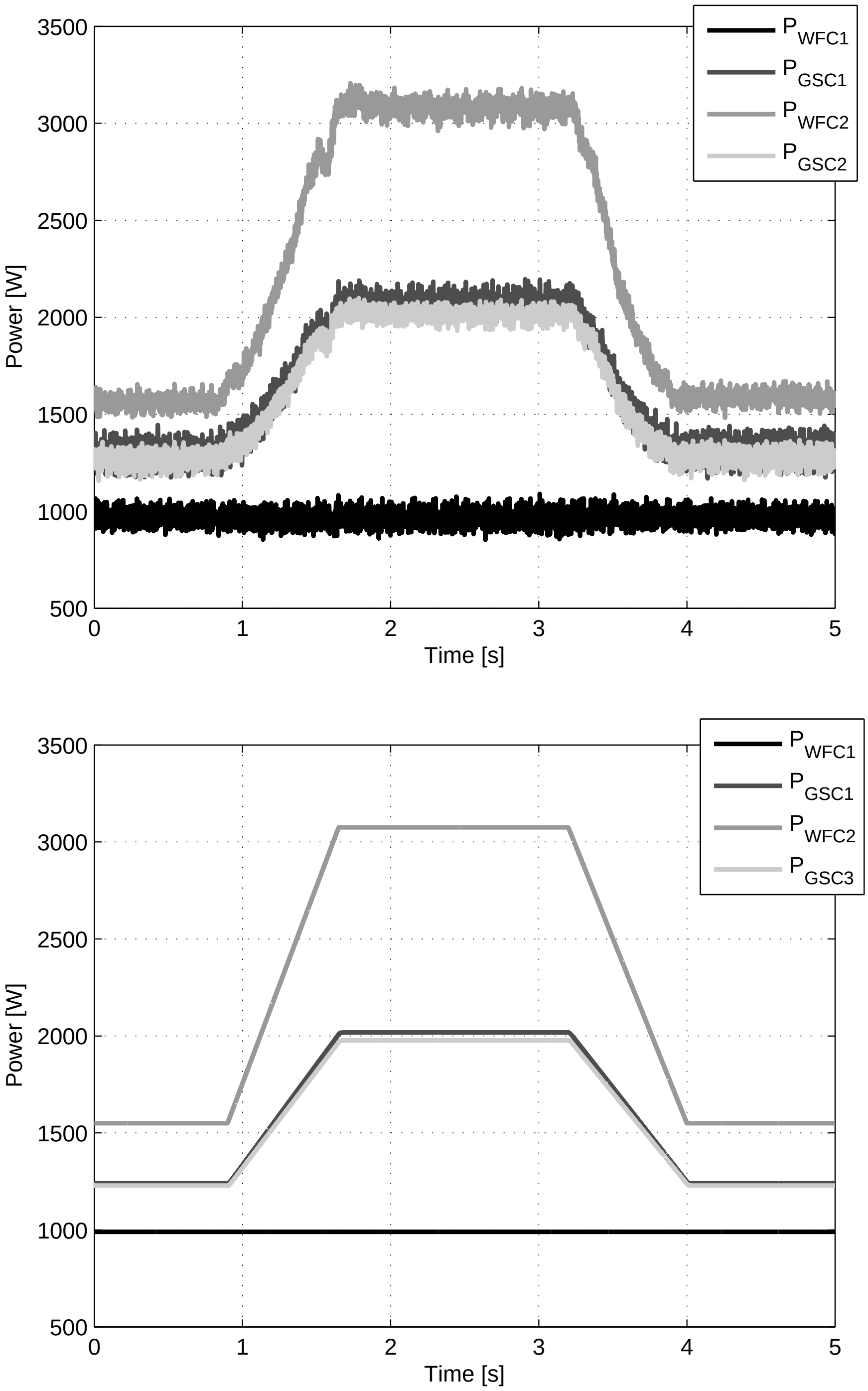

Figure 4.6: Power and AC currents at GSC2 during a change in the power reference at the WF2(Real system: left, Simulated system: Right)

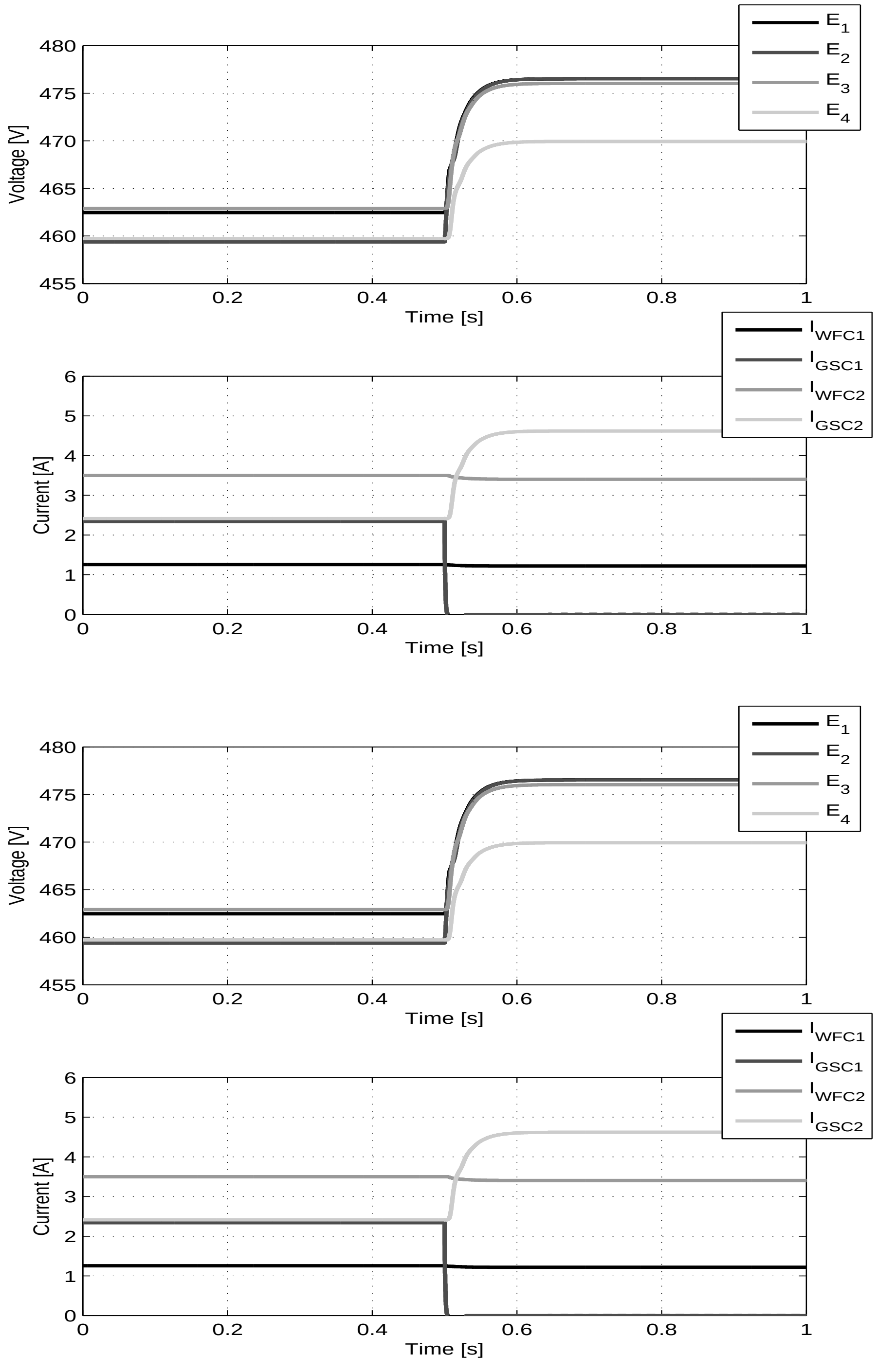

Figure 4.7: DC Voltages and currents during the disconnection of the GSC1

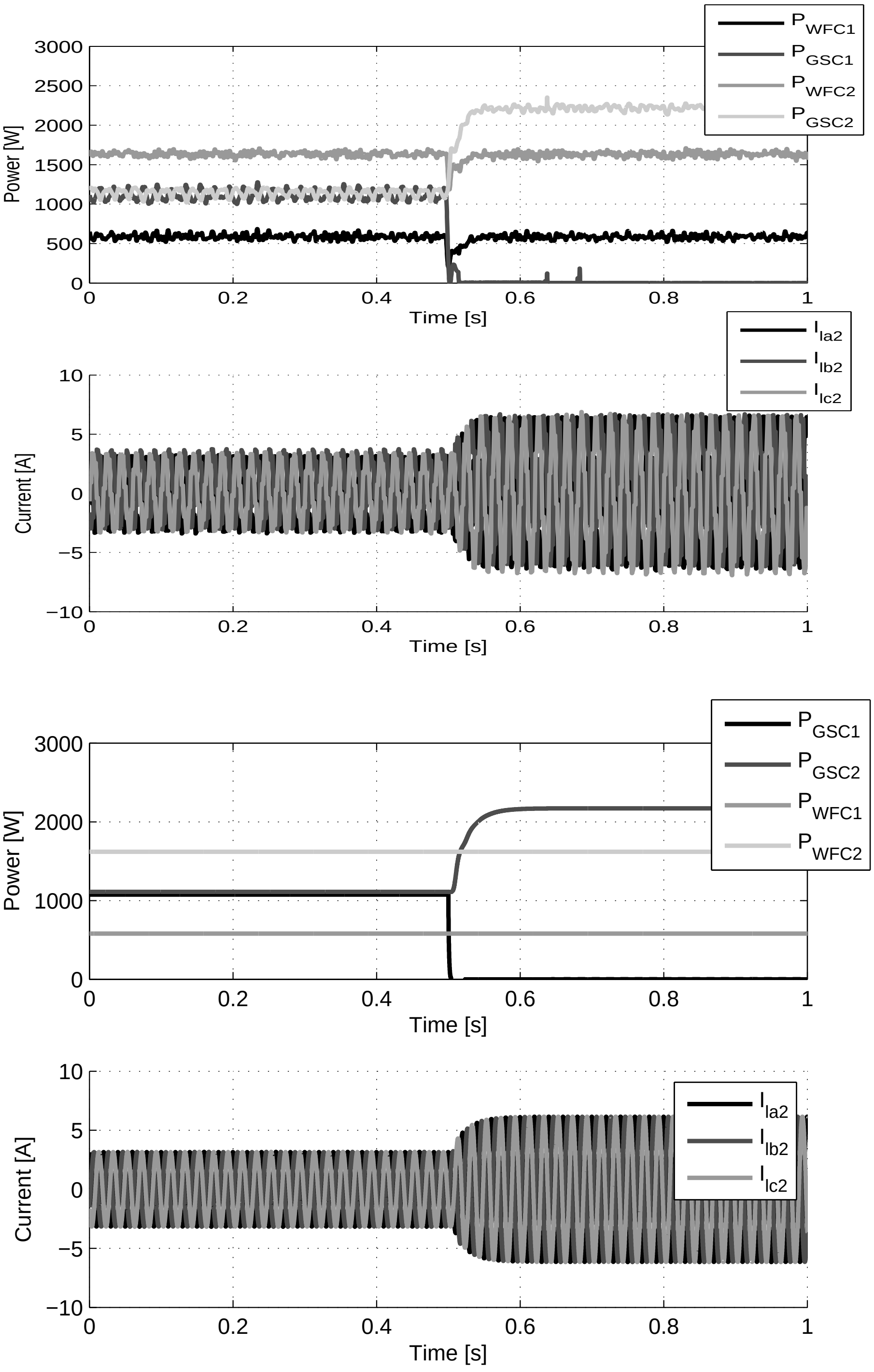

Figure 4.8: Power and AC currents in the GSC2 during the disconnection of the GSC1

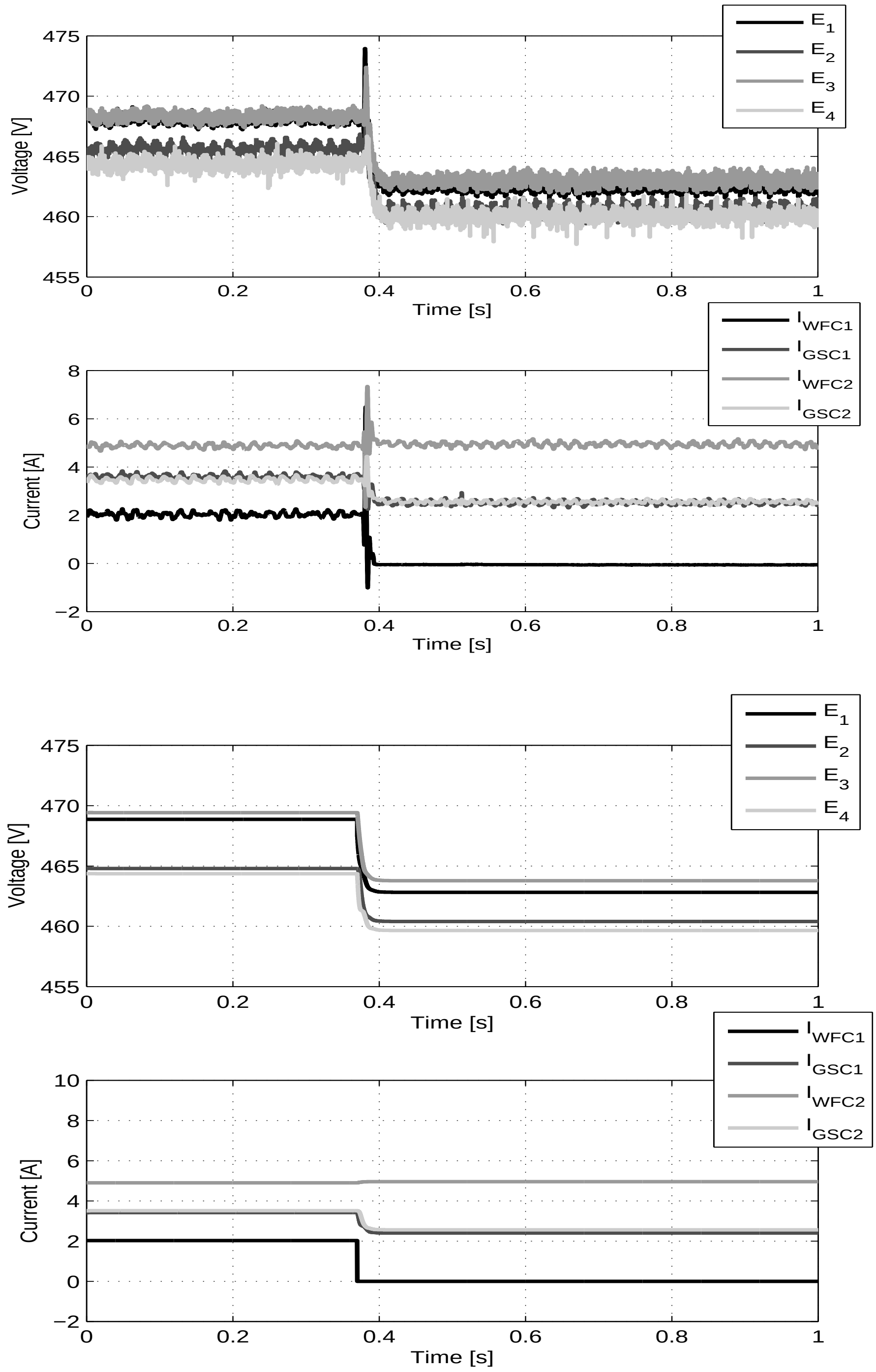

Figure 4.9: DC voltages and currents during the disconnection of the WFC1

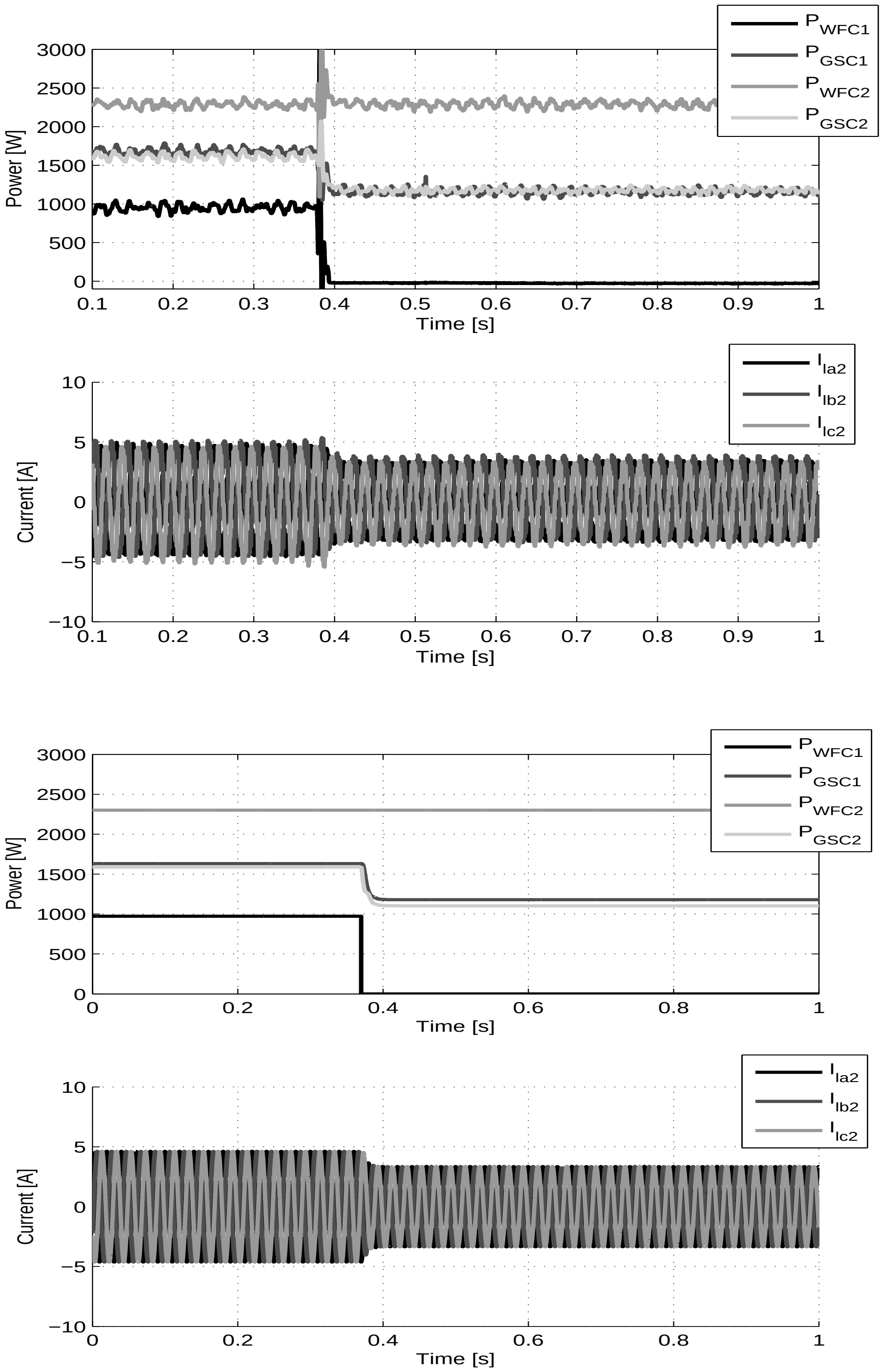

Figure 4.10: Power and AC currents of the GSC2 during the disconnection of the WF1

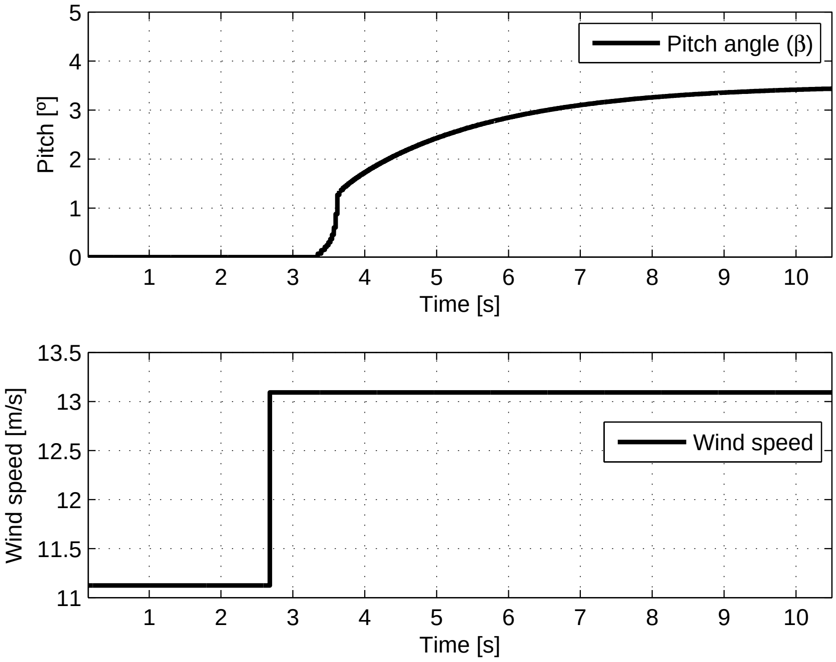

Figure 4.11: Wind speed and pitch angle evolution in front of a wind speed change

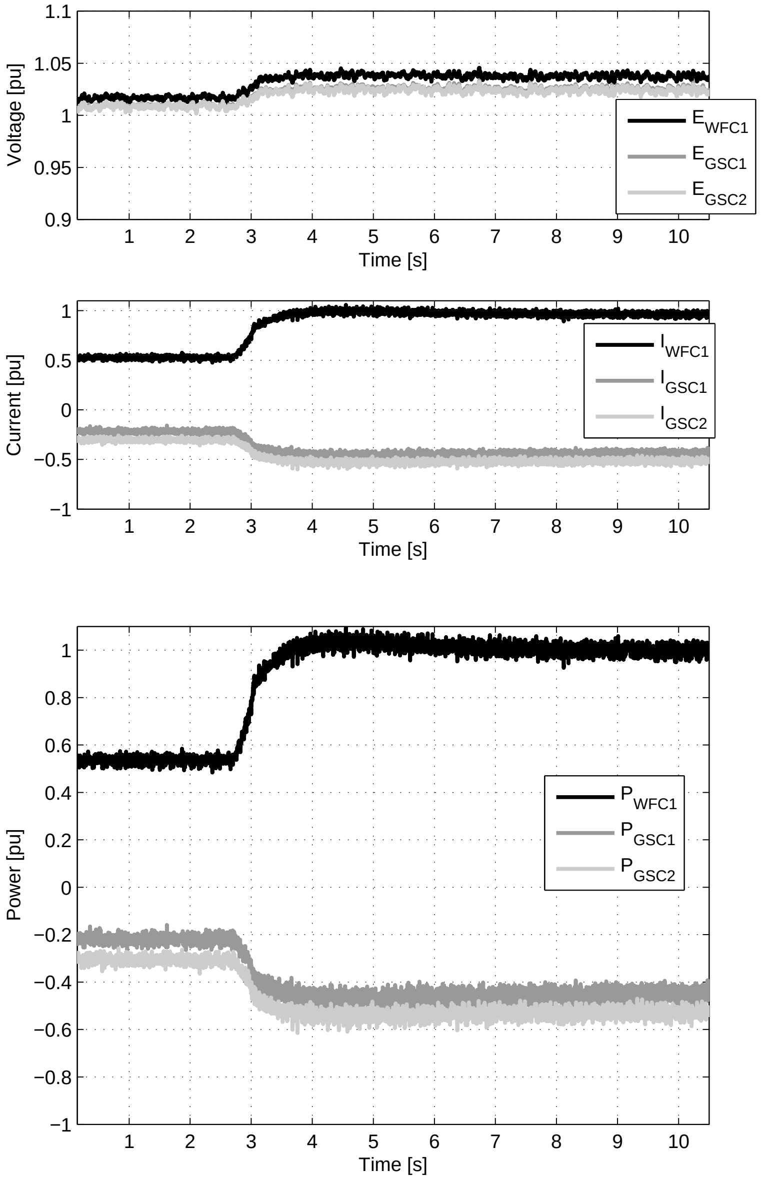

Figure 4.12: DC currents and voltages and powers in front of a wind step change

Chapter 5

Coordinated power reduction control for operation and fault conditions

5.1 Introduction

The objective of the present chapter is to introduce a coordinated power reduction scheme for offshore HVDC transmissions. When an AC contingency takes place, all the generated power might not be injected to the AC grid because the power converter current limit is reached. In these situations, the power that cannot be injected to the AC system is stored in the capacitors, and the DC voltage starts to rise. Consequently, the DC voltage must be using other methods. A possible solution is the use of a Dynamic Braking Resistor (DBR) installed in the GSC that permits the dissipation of the excess power. Another solution consists in the power reduction generated by the wind farms.

In this chapter a combined scheme where a short term power reduction based on an HVDC-DBR permits to right-through short contingencies, as voltage sags, is proposed. If the fault lasts more than a traditional fault, the wind farm reduces the generated power (Wind Turbine - DBR (WT-DBR) or the pitch system can be used). Especially, it is studied the design of the power controllers in order to avoid limit cycles or maintained oscillations. Limit cycles appear as a consequence of the interaction of the inappropriate gain controller and the plant when the control action is saturated. In the studied case, the HVDC-DBR and WT-DBR are limited by the maximum power that can dissipate. The tool selected to establish a design criteria is the describing function. It consists of a non-linear analysis tool that permits to study the existence of limit cycles, mainly in SISO (Single-input Single-Output) systems [29, 30]. The classical approach of the describing function is only valid for linear systems and the equations are linearised [31, 32].

5.2 Analysed system

The system under study consists of an HVDC link based on VSC technology that connects an offshore wind farm with the main AC grid. GSC is connected to the AC grid by means of an inductive coupling reactor. Furthermore, the GSC is equipped with an HVDC-DBR that permits to dissipate the power that cannot be injected during AC faults. The WFC is connected to the wind farm by means of an LC coupling filter. It allows the control of the wind farm voltage, as well as, the AC current in the inductance. The wind turbines are distributed in arrays and connected to the WFC via a collector. The wind farm is composed of full power converter wind turbines with an individual WT-DBR and a pitch system. The wind turbine power converter facing the offshore grid is named Wind Turbine Converter (WTC) and the power converter facing the electrical generator is called Wind Generator Converter (WGC). A sketch of the studied scheme can be seen in Figure 5.1.

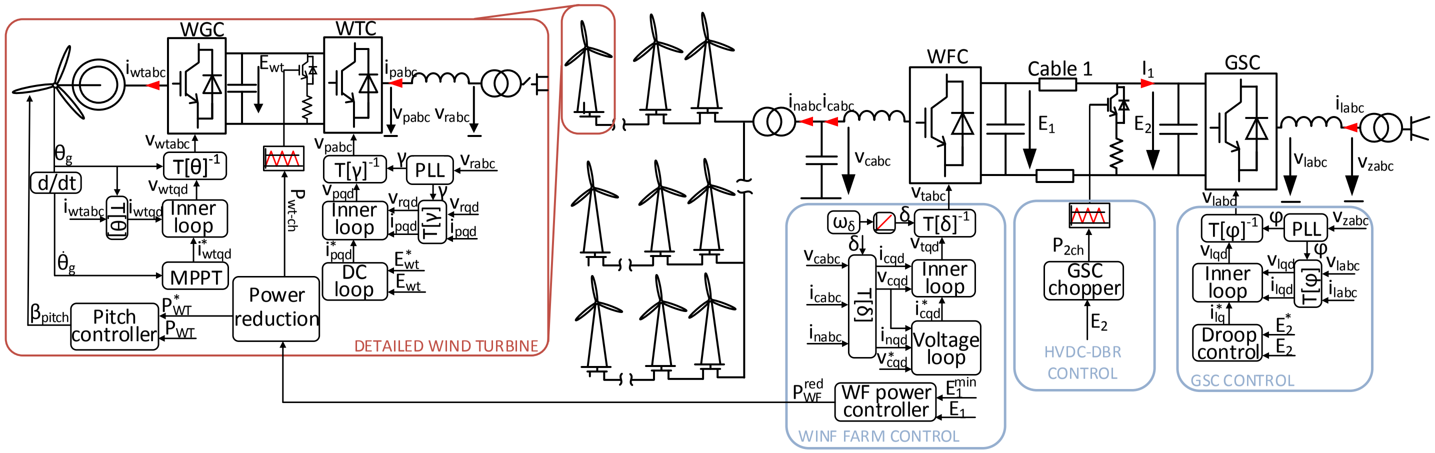

Figure 5.1: Analysed system and power converter control scheme

5.3 Electrical system modelling

Two electrical models have been been developed in order to perform the study, one is an aggregated full detailed model used to evaluate the control performance by means of simulations, inspired in [33] and similar to the electrical scheme presented in Figure 5.1. The other one is a linearised model to study the system stability and the control setting. This model consists of: a wind turbine aggregated model, a wind farm grid aggregated model and a HVDC link. Power converters have been modelled by means of the average low frequency model, consisting of three AC voltage source on the AC side and a current source on the DC side [25]. Figure 5.2 shows the linearised electrical scheme.

As the studied control system only acts when an AC fault occurs, the AC contingency is modelled as a power unbalance between the aggregated wind turbine model and the GSC by means of a constant power source in the HVDC. From this assumption the GSC control and the WGC control are not required and the system to be studied is simplified.

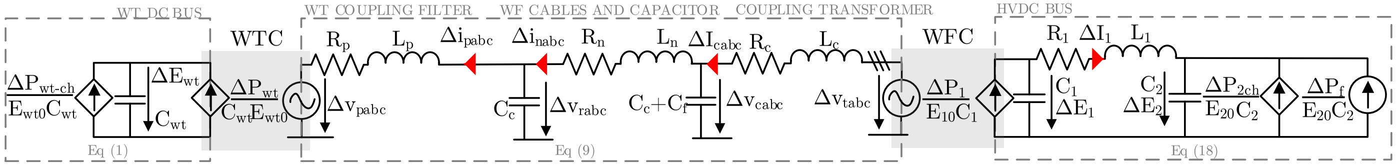

Figure 5.2: Single-phase and DC system linearised electrical model

5.3.1 Linearised wind turbine aggregated model equations

The linearised wind turbine aggregate consist of a model where the wind turbine DC bus, the WT-DBR and the wind turbine grid side converter have been modelled. WT-DBR is modelled as a linearised power source expressed as a current source. The wind generator and the machine side converter has been not modelled because the machine dynamics are slower compared to the rest of system dynamics due to the large rotor inertia [33]. The linearised wind turbine state-space model is defined as

$$\Delta\dot{x}_w = A_w\Delta x_w + B_w\Delta u_w \tag{5.1}$$

$$\Delta y_w = C_w\Delta x_w \tag{5.2}$$

where the matrix gains are

$$A_w = \begin{bmatrix} \frac{-P_{wt0}}{C_{wt}E_{wt0}^2} + \frac{-P_{wt-ch0}}{C_{wt}E_{wt0}^2} \end{bmatrix} \tag{5.3}$$

$$B_w = \begin{bmatrix} \frac{1}{C_{wt}E_{wt0}} & \frac{1}{C_{wt}E_{wt0}} \end{bmatrix}^T \tag{5.4}$$

$$C_w = \begin{bmatrix} 1 \end{bmatrix} \tag{5.5}$$

where the state, inputs and output vectors are

$$\Delta x_w = [\Delta E_{wt}] \tag{5.6}$$

$$\Delta u_w = [\Delta P_{wt}\ \Delta P_{ch-wt}]^T \tag{5.7}$$

$$\Delta y_w = [\Delta E_{wt}] \tag{5.8}$$

where E_{wt} is the wind turbine DC bus voltage, P_{wt} is power injected by the wind turbine converter, P_{ch-wt} is the power injected by the WT-DBR.

5.3.2 Wind farm grid linearised model

The linearised wind farm grid is modelled in qd reference frame and consists of an aggregated wind turbine inductive coupling filter impedance $\underline{Z_p} = R_p + \jmath\omega L_p$, an aggregated π equivalent cable model, where C_c is the shunt capacitor and $\underline{Z_n} = R_n + \jmath\omega L_n$ is the line impedance and the LC coupling filter for the WFC, where C_f is the shunt HVDC capacitor and in the HVDC inductive filter impedance $\underline{Z_n} = R_n + \jmath\omega L_n$. The state space that models the system is

$$\begin{aligned} \Delta\dot{x}_{wf} &= [A_{wf1}|B_{wf2}]\Delta x_{wf} + B_{wf}\Delta u_{wf} && (5.9) \\ \Delta y_{wf} &= \left[\frac{I_{10}}{C_{wf1}}\right]\Delta x_{wf} + \left[\frac{0_{10,4}}{D_{wf1}}\right]\Delta u_{wf} && (5.10) \end{aligned}$$

$$A_{wf1} = \begin{bmatrix} -\frac{R_p}{L_p} & -\omega & \frac{1}{L_p} & 0 & 0 \\ \omega & -\frac{R_p}{L_p} & 0 & \frac{1}{L_p} & 0 \\ -\frac{1}{C_f} & 0 & 0 & -\omega & \frac{1}{C_f} \\ 0 & -\frac{1}{C_f} & \omega & 0 & 0 \\ 0 & 0 & -\frac{1}{L_n} & 0 & -\frac{Rn}{L_n} \\ 0 & 0 & 0 & -\frac{1}{L_n} & \omega \\ 0 & 0 & 0 & 0 & -\frac{1}{C_c+C_f} \\ 0 & 0 & 0 & 0 & 0 \\ 0 & 0 & 0 & 0 & 0 \\ 0 & 0 & 0 & 0 & 0 \end{bmatrix} \tag{5.11}$$

$$A_{wf2} = \begin{bmatrix} 0 & 0 & 0 & 0 & 0 \\ 0 & 0 & 0 & 0 & 0 \\ 0 & 0 & 0 & 0 & 0 \\ \frac{1}{C_f} & 0 & 0 & 0 & 0 \\ -\omega & \frac{Rn}{L_n} & 0 & 0 & 0 \\ -\frac{R_n}{L_n} & 0 & \frac{Rn}{L_n} & 0 & 0 \\ 0 & 0 & -\omega & \frac{1}{C_c+C_f} & 0 \\ -\frac{1}{C_c+C_f} & \omega & 0 & 0 & \frac{1}{C_c+C_f} \\ 0 & -\frac{1}{L_c} & 0 & -\frac{R_c}{L_c} & -\omega \\ 0 & 0 & -\frac{1}{L_c} & \omega & -\frac{R_c}{L_c} \end{bmatrix} \tag{5.12}$$

$$B_{wf} = \begin{bmatrix} -\frac{1}{L_p} & 0 & 0 & 0 \\ 0 & -\frac{1}{L_p} & 0 & 0 \\ 0 & 0 & 0 & 0 \\ 0 & 0 & 0 & 0 \\ 0 & 0 & 0 & 0 \\ 0 & 0 & 0 & 0 \\ 0 & 0 & 0 & 0 \\ 0 & 0 & 0 & 0 \\ 0 & 0 & \frac{1}{L_c} & 0 \\ 0 & 0 & 0 & \frac{1}{L_c} \end{bmatrix}$$

$$C_{wf1} = \begin{bmatrix} \frac{3}{2}v_{pq0} & \frac{3}{2}v_{pd0} & 0 & 0 & 0 & 0 & 0 & 0 & 0 & 0 \\ 0 & 0 & 0 & 0 & 0 & 0 & 0 & 0 & \frac{3}{2}v_{cq0} & \frac{3}{2}v_{cd0} \end{bmatrix} \tag{5.13}$$

$$D_{wf1} = \begin{bmatrix} \frac{3}{2}i_{cq0} & \frac{3}{2}i_{cd0} & 0 & 0 \\ 0 & 0 & \frac{3}{2}i_{cq0} & \frac{3}{2}i_{cd0} \end{bmatrix} \tag{5.14}$$

and the state and input vectors are,

$$\begin{aligned} x_{lc} = [&\Delta i_{pq}\ \Delta i_{pd}\ \Delta v_{rq}\ \Delta v_{rd}\ \Delta i_{nq} \\ &\Delta i_{nd}\ \Delta v_{cq}\ \Delta v_{cd}\ \Delta i_{cq}\ \Delta i_{cd}]^T \end{aligned} \tag{5.15}$$

$$u_{lc} = [\Delta v_{pq}\ \Delta v_{pd}\ \Delta v_{tq}\ \Delta v_{td}\ ]^T \tag{5.16}$$

$$\begin{aligned} y_{lc} = [&\Delta i_{pq}\ \Delta i_{pd}\ \Delta v_{rq}\ \Delta v_{rd}\ \Delta i_{nq} \Delta i_{nd} \\ &\Delta v_{cq}\ \Delta v_{cd}\ \Delta i_{cq}\ \Delta i_{cd}\ \Delta P_{wt}\ \Delta P_1]^T \end{aligned} \tag{5.17}$$

where v_{pqd} is the voltage at the WTC terminals, i_{pqd} is the current injected by the WTC, v_{rqd} is the voltage at the aggregated cable wind turbine starting, i_{nqd} is the current through the cable, v_{cqd} is the voltage at the coupling shunt capacitor, i_{cqd} is the current through the inductance coupling filter, v_{tqd} is the voltage applied by the WFC, P_1 is the power injected to the HVDC link.

5.3.3 HVDC link linearised equations

The HVDC link is modelled as π equivalent, where C_1 and C_2 are the shunt capacitors that is the sum of the DC capacitor filter at the converter terminals and the cable equivalent capacitor, and R_1 and L_1 is the equivalent cable resistance and inductance. The HVDC-DBR has been modelled as a linearised power source.

$$\begin{aligned} \Delta \dot{x} &= A_{hv}\Delta x_{hv} + B_{hv}\Delta u_{hv} && (5.18) \\ \Delta y &= C_{hv}\Delta x_{hv} && (5.19) \end{aligned}$$

where the matrix gains are

$$\begin{aligned} A_{hv} &= \begin{bmatrix} -\dfrac{P_{10}}{C_1E_{10}^2} & \dfrac{1}{C_!} & 0 \\ \dfrac{1}{L_1} & -\dfrac{R_1}{L_1} & -\dfrac{1}{L_1} \\ 0 & \dfrac{1}{C_2} & -\dfrac{P_{2ch0}}{C_2E_{20}^2} - \dfrac{P_{f0}}{CE_{20}^2} \end{bmatrix} && (5.20) \\ B_{hv} &= \begin{bmatrix} \dfrac{1}{C_1E_{10}} & \dfrac{1}{C_1E_{20}} \end{bmatrix}^T && (5.21) \\ C_{hv} &= \begin{bmatrix} 1 & 0 & 0 \\ 0 & 0 & 1 \end{bmatrix} && (5.22) \end{aligned}$$

where the state, inputs and output vectors are

$$\begin{aligned} \Delta x_{hv} &= [\Delta E_1 \ \Delta I_1 \ \Delta E_2]^T && (5.23) \\ \Delta u_{hv} &= [\Delta P_1 \ \Delta P_{2ch}]^T && (5.24) \\ \Delta y_{hv} &= [\Delta E_1 \ \Delta E_2]^T && (5.25) \end{aligned}$$

where E_1 is the DC voltage at the WFC terminals, I_1 is the current through the HVDC cable, E_2 is the voltage at the GSC terminals and P_{2ch} is the power injected by the HVDC-DBR. P_f pretends to simplify the linearised model, reducing the number of system inputs considering a three phase fault as a power unbalance between the power that can be injected to the AC grid and the generated power. To demonstrate the validity of this simplification Figure 5.3 shows a comparison of the DC bus voltage at GSC converter terminals (E_2) between the full detailed model under a three phase voltage sag and the simplified power constant source. During this fault the HVDC-DBR dissipates the power that can not be injected. The maximum error during the fault is below the 1.3%.

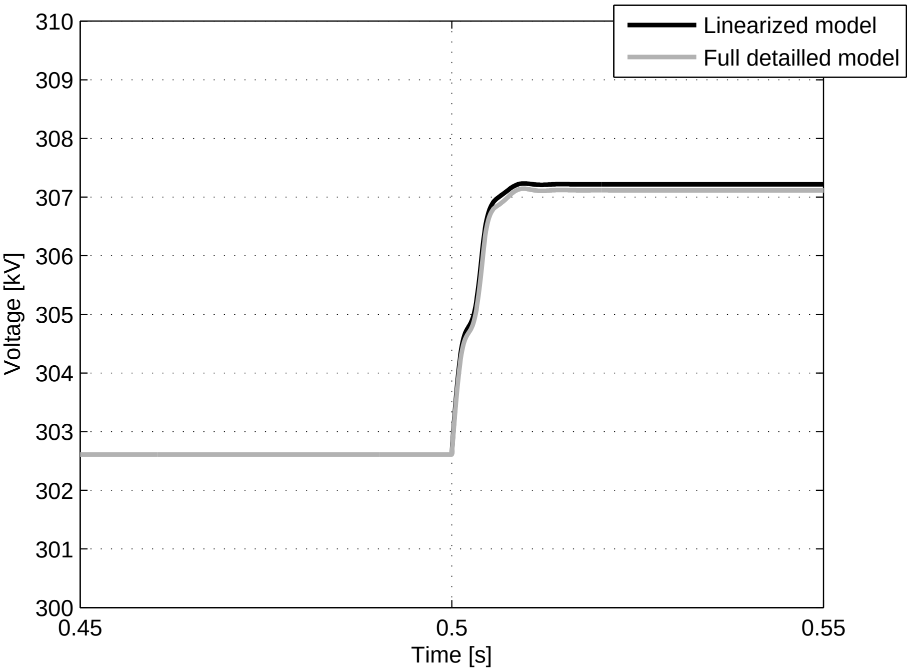

Figure 5.3: E_2 voltage comparison and error between the full model under a three-phase voltage sag and the linearised model using a constant power source for the fault.

5.4 System control description and linearised equations

In this section, a description of the different controllers and control strategies applied to the HVDC transmission and the wind farm are commented. An scheme summarising all the controllers can be seen in Figure 5.1.

5.4.1 Wind turbine control

Wind turbine control is divided between the electrical control and the mechanical control. The electrical control is composed of the WGC and the WTC control. The WGC control has an inner loop that controls the torque and the flux of the generator [34]. Torque references are given by the outer loop based on a Maximum Power Point Tracker (MPPT) algorithm that calculates the torque to extract the optimal power [35]. WTC controls the DC bus voltage and the reactive power injected to the AC grid. There is an inner current control that regulates the current thorough the coupling inductance and an upper level control based on a PI that controls the DC voltage. The controller is grid oriented using a PLL [17]. Furthermore, a WT-DBR is installed in each wind turbine. The mechanical control is a pitch controller that reacts when the electrical generated power (P_{wt}) exceed the power reference (P_{wt}^{*}), usually the nominal power [34].

5.4.2 Wind farm voltage control and HVDC Link Control

WFC controls the wind farm AC voltage at the coupling capacitor. The control is implemented using an inner current control that regulates the current through the inductive coupling filter and an outer control loop that controls the voltage at the shunt capacitor. The AC voltage frequency is fixed at a given frequency.

GSC is in charge of the DC link voltage control and the reactive power injected to the grid. The DC voltage is controlled by means of a droop voltage controller that is designed using the methodology presented in [25]. The droop voltage control is implemented as

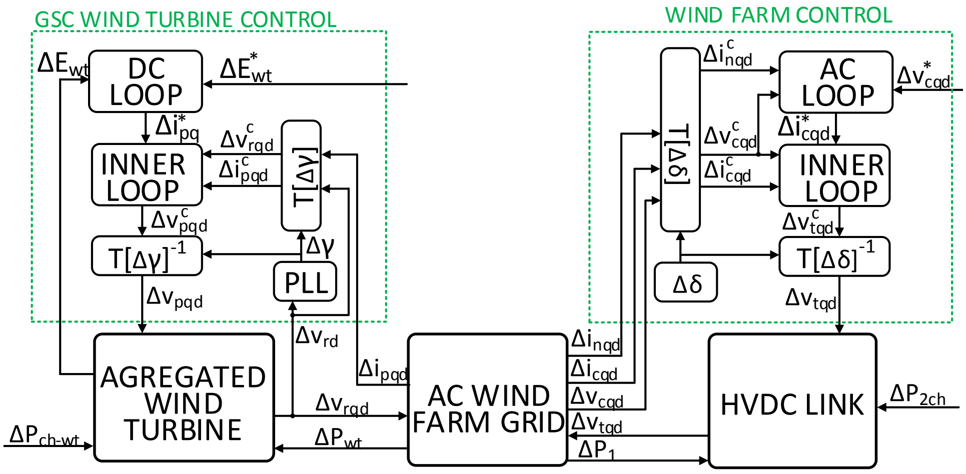

Figure 5.4: Connection of the electrical linearised equations and the control linearised equations

$$I^*_{in2} = K_{droop}(E_2 - E^*_2) \tag{5.26}$$

where I^*_{in2} is the DC current reference for the GSC and K_{droop} is the controller gain.

5.4.3 Linearised control equations

The control equations need to be linearised in order to use the classic control engineering tools. The majority of the applied controller are linear but the effect of the angle in the Park transformation or in the PLL should be taken in account. Control system equations are presented below. The connection between the linearised electrical model and the controllers is shown in Figure 5.4.

Linearised PLL equations

The PLL is used in order to orientate a control with the electrical grid angle. In the linearised model the PLL introduces the angle deviation when the linearised system is moved from the linearisation point. The PLL linearised transfer function representation is

$$\Delta\theta = -\frac{k_{p-pll}s + k_{i-pll}}{s^2 + v_{xq0}k_{p-pll}s + v_{xq0}k_{i-pll}} \tag{5.27}$$

where v_{xqd0} is a generic voltage, k_{p-pll} is the PLL proportional controller gain, k_{i-pll} is the integral controller gain and θ is a generic angle. The PLL has been linearised according to [36] and tuning following [17].

Linearised Park transformation and inverse-transformation equations

Park transformation allows the transformation of the three-phase *abc* quantities into the synchronous reference *qd* frame. It is linearised to take in account the effect of the angle variation. The linearised Park transformation is given by,

$$\left[x^c_{qd0}\right] = \left[T_{qd0}\right]\left[x_{qd0}\right] \tag{5.28}$$

where $T[\theta]$ is

$$\left[T_{qd0}\right] = \begin{bmatrix} \cos(\theta_0) & -\sin(\theta_0) & -\sin(\theta_0)\ x_{q0} - \cos(\theta_0)\ x_{d0} \\ \sin(\theta_0) & \cos(\theta_0) & \cos(\theta_0)\ x_{q0} - \sin(\theta_0)\ x_{d0} \end{bmatrix} \tag{5.29}$$

and the linearised inverse transformation is,

$$\left[x_{qd0}\right] = \left[T_{qd0}\right]^{-1}\left[x^c_{qd0}\right] \tag{5.30}$$

where $T[\theta]^{-1}$ is

$$\left[T_{qd0}\right]^{-1} = \begin{bmatrix} \cos(\theta_0) & \sin(\theta_0) & \cos(\theta_0)\ x_{d0} - \sin(\theta_0)\ x_{q0} \\ -\sin(\theta_0) & \cos(\theta_0) & -\cos(\theta_0)\ x_{q0} - \sin(\theta_0)\ x_{d0} \end{bmatrix} \tag{5.31}$$

where x is the transformed electrical variable. The transformed variables are indicated with the superscript '^{c}'.

Current loop equations

The vector current control allows to control the voltage through an inductance applying a given voltage in its terminals. It requires the measure of the current and the voltage on the ending terminals terminals. The state-space representation is,

$$\begin{aligned} \Delta \dot{x}_{il} &= B_{il} \Delta u_{il} && (5.32) \\ \Delta y_{il} &= C_{il} \Delta x_{il} + D_{il} \Delta u_{il} && (5.33) \end{aligned}$$

where the state variables, inputs and outputs are,

$$\begin{aligned} \Delta x_{il} &= [\Delta ei^c_{xq} \ \Delta ei^c_{xd}]^T && (5.34) \\ \Delta u_{il} &= [\Delta i^*_{xq} \ \Delta i^*_{xd} \ \Delta i^c_{xq} \ \Delta i^c_{xd} \ \Delta v^c_{hq} \ \Delta v^c_{hd}]^T && (5.35) \\ \Delta y_{il} &= [\Delta v^c_{lq} \ \Delta v^c_{ld}]^T && (5.36) \end{aligned}$$

The subscript "$_x$" refers to a generic controlled variable, v_{hqd} is the node with the highest voltage and v_{lqd} is the voltage with the lowest voltage. Δei_{xqd} is the current error, defined as the difference between Δi^*_{xqd} and Δi_{xqd}. The matrix gains are,

$$\begin{aligned} B_{il} &= \begin{bmatrix} -1 & 0 & 1 & 0 \\ 0 & -1 & 0 & 1 \end{bmatrix} && (5.37) \\ C_{il} &= \begin{bmatrix} k_{i-il} & 0 \\ 0 & k_{i-il} \end{bmatrix} && (5.38) \\ D_{il} &= \begin{bmatrix} -k_{p-il} & 0 & k_{p-il} & -\omega L_x & 1 & 0 \\ 0 & -k_{p-il} & \omega L_x & k_{p-il} & 0 & 1 \end{bmatrix} && (5.39) \end{aligned}$$

where k_{i-il} and k_{p-il} are the integral and proportional controller gains and L_x is a generic inductance where the current is controlled. The inner loop has been tune according to [37].

Voltage loop controller

The voltage loop is used to control the current across a shunt capacitor injecting a given amount of current. It requires the voltage of the capacitor and the output line current measures.

$$\Delta\dot{x}_{ol} = B_{ol}\Delta u_{ol} \tag{5.40}$$

$$\Delta y_{ol} = C_{ol}\Delta x_{ol} + D_{ol}\Delta u_{ol} \tag{5.41}$$

where the state variables, inputs and outputs are

$$\Delta x_{ol} = [\Delta ev_{xq} \ \Delta ev_{xd}]^T \tag{5.42}$$

$$\Delta u_{ol} = [\Delta v^*_{xq} \ \Delta v^*_{xd} \ \Delta v^c_{xq} \ \Delta v^c_{xd} \Delta i^c_{oq} \ \Delta i^c_{od}]^T \tag{5.43}$$

$$\Delta y_{ol} = [\Delta i^*_{iq} \ \Delta i^*_{iq}]^T \tag{5.44}$$

i_{iqd} is the current injected by the converter and i_{oqd} is the current at the output line. Δev_{xqd} is the voltage error, defined as the difference between Δv^*_{xqd} and Δv_{xqd}. The matrix gains are,
where the matrix gains are defined as

$$B_{ol} = \begin{bmatrix} -1 & 0 & 1 & 0 \\ 0 & -1 & 0 & 1 \end{bmatrix} \tag{5.45}$$

$$C_{ol} = \begin{bmatrix} k_{i-ol} & 0 \\ 0 & k_{i-ol} \end{bmatrix} \tag{5.46}$$

$$D_{ol} = \begin{bmatrix} -k_{p-ol} & 0 & k_{p-ol} & -\omega C_x & 1 & 0 \\ 0 & -k_{p-ol} & \omega C_x & k_{p-ol} & 0 & 1 \end{bmatrix} \tag{5.47}$$

where k_{p-ol} and k_{i-ol} are the proportional and integral controller gains and C_x is the generic capacitor where the voltage is controlled.

DC Voltage loop controller

The DC bus voltage controller is based on a PI controller that calculates the i^*_{pq} current loop setpoint as

$$G_{e-wt}(s) = \frac{k_{p-DC}s + k_{i-DC}}{s} \tag{5.48}$$

where k_{p-DC} and k_{i-DC} are the proportional and the integral gains.

5.5 Proposed power reduction methods controller design

In this section, a coordinated power reduction method for fault or curtailment situations is proposed. In the case of an AC contingency, all the generated power could not be injected to the AC grid due to the GSC current limit. For short faults, it is enough to dissipate the excess power in the HVDC-DBR, but for long faults (e.g. the disconnection of a line) it is not possible to evacuate this power due to the HVDC-DBR decreasing heat exchange capability. It means that the power should be reduced by the wind turbines.

The proposed power reduction method is divided into two parts. The first part consist of a proportional controller that connects the HVDC-DBR to maintain the system stability during the fault first instants. If the fault lasts more than some seconds (t_f) a second DC voltage control is activated and reduces the power generated by the wind turbine. This controller measures the DC voltage at the WFC terminals and sends a power reduction reference to the wind turbines. The wind farm power reduction curve should be tuned to react at the voltage levels near the GSC saturation. In order to avoid interaction between the two power reduction methods, the HVDC-DBR characteristic should start react after the maximum power reduction of the wind farm power reduction characteristic. Figure 5.5 shows the GSC droop voltage control characteristic, the power reduction characteristic for the HVDC-DBR and the wind farm power reduction characteristic expressed at the DC terminals of the GSC.

The HVDC-DBR is controlled by means of a proportional control law, that dissipates the power according to the E_2 DC voltage. The percentage of the power reduction is defined as

$$P_{2ch}^{red} = \frac{E_2 - E_2^{min}}{E_2^{max} - E_2^{min}} = K_{HV}(E_2 - E_2^{min}) \tag{5.49}$$

where P_{2ch}^{red} is the percentage of power needed to reduce, E_2^{min} is the minimum voltage threshold, E_2^{max} is the maximum voltage threshold. This two

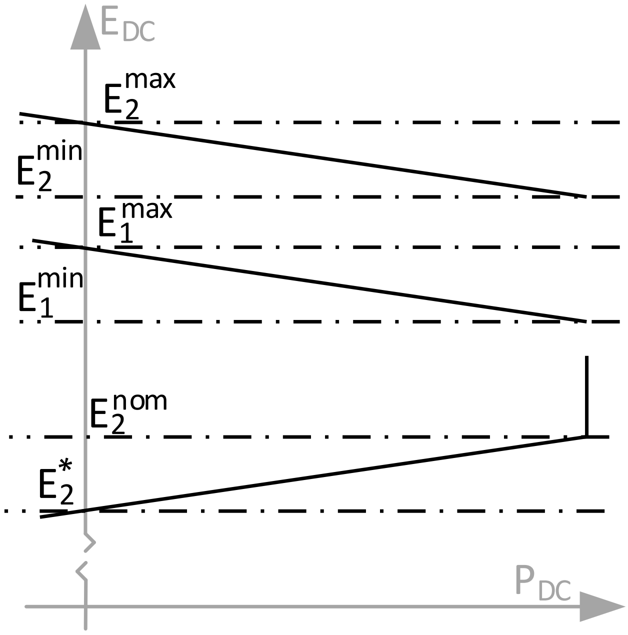

Figure 5.5: GSC droop, HVDC-DBR and WT-DBR characteristics

voltages define the controller gain $K_{HV} = \frac{1}{E_2^{max} - E_2^{min}}$. The control action of this controller is saturated between 0 and 1 due to the power dissipation capability of the HVDC-DBR. P_{2ch}^{red} matches with the duty cycle that is sent to the transistors that controls the HVDC-DBR. For the wind farm power reduction it is proposed to use a proportional power reduction curve similar to the GSC-HVDC characteristic. It is defined as

$$P_{wf}^{red} = \frac{E_1 - E_1^{min}}{E_1^{max} - E_1^{min}} = K_{WF}(E_1 - E_1^{min}) \tag{5.50}$$

where P_{wf}^{red} is the percentage of power need to we reduced by the wind farm, E_1^{min} is the minimum voltage action threshold, E_1^{max} is the maximum voltage threshold. This two voltages define the controller gain $K_{WF} = \frac{1}{E_1^{max} - E_1^{min}}$.

These gains should be tuned ensuring a good dynamic response and respecting the maximum voltage limits supported by the power converters and cables. One of the main drawbacks in the gain selection is the existence of limit cycles. In order to select a K_{WF} and K_{HV} the describing function analysis has been applied to the linearised system. A four-step methodology is presented to design the power reduction droops:

E_1^{min} Selection - E_1^{min} is selected to act the wind farm power reduction immediately after the saturation of the GSC if the fault lasts more than a few seconds. It means that E_1^{min} should be close to the maximum voltage that can be reach in normal operation. This value is calculated determining the maximum voltage E_2 during normal operation as

$$P_2^{nom} = I_{GSC} E_2^{nom} = K_{droop}(E_2^{nom} - E_2^{*}) E_2^{nom} \tag{5.51}$$

$$E_2^{nom} = \frac{\sqrt{4K_{droop}P_{nom} + E_2^{*2}} + E_2^{*}K_{droop}}{2K_{droop}} \tag{5.52}$$

where P_{nom} is the power converter nominal power and E_2^{nom} is the E_2 voltage when P_{nom} is injected. Once the maximum voltage E_2 is determined, the voltage at the WFC terminals, E_1, is calculated considering the voltage droop at the resistance. This value is the minimum value that E_1^{min} can have. It is calculated as

$$E_1^{min} \geq \frac{P_{max}}{E_2^{nom}} R_1 + E_2^{nom} \tag{5.53}$$

It is suggested to leave a dead-band between the calculated minimum level and the selected minimum value.

E_1^{max} Selection - E_1^{max} is the maximum voltage that defines the K_{WF}. This value is the most critical due to the possible DC voltage limit cycle due to the multiple different dynamics and controllers that are installed between the wind turbines and the WFC (an example of inappropriate tuning is field in Section 5.7). To ensure the appropriate gain selection, the describing function is used. This non-linear analysis tool allows to determine the existence of limit cycles (sustained oscillations) due to the system non-linearities [38]. It consists of studying the characteristic equation of the close loop transfer function (see Figure 5.6) of a linear function (G(jω)) and the describing function (N) of the non-linear element (eq. 5.54). If N and G(jω) intersect, a maintained oscillation may exist.

$$1 + NG(j\omega) \tag{5.54}$$

$$G(j\omega) = -\frac{1}{N} \tag{5.55}$$

A graphical way to identify limit cycles is to plot the Nyquist diagram of the linear plant and the describing function of the non-linear saturation in the imaginary axis and analyse the intersection. In the present article the analysed non-linearity is the maximum power that can be injected by the DBRs represented by means of a saturation, described as

$$N = \frac{2k}{\pi}\left(\sin^{-1}\left(\frac{S}{X}\right) + \frac{S}{X}\sqrt{1 - \left(\frac{S}{X}\right)^2}\right) \tag{5.56}$$

where S is the saturation amplitude and X is the input signal amplitude.

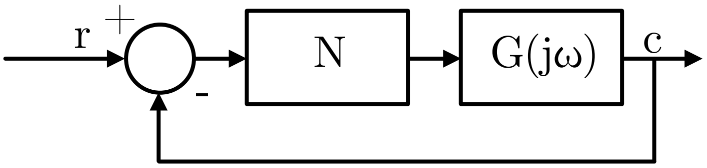

Figure 5.6: Generic non-linear close loop transfer function

The design of the K_{WF} is carried out considering that all the power is dissipated in the WT-DBT, at least for a certain period of time as it is explained in section 5.6. This means that the K_{WF} is designed considering that the DC voltage E_1 is controlled by means of the WT-DBR. To analyse this case the linear transfer function that links the power evacuated from the WT-DBR P_{wt-ch} and E_1 and can be deduced from the diagram presented in Figure 5.4. Figure 5.7 a) shows the block diagram of the studied close loop system. During the K_{WF} design phase is assumed that HVDC-DBR is not acting.

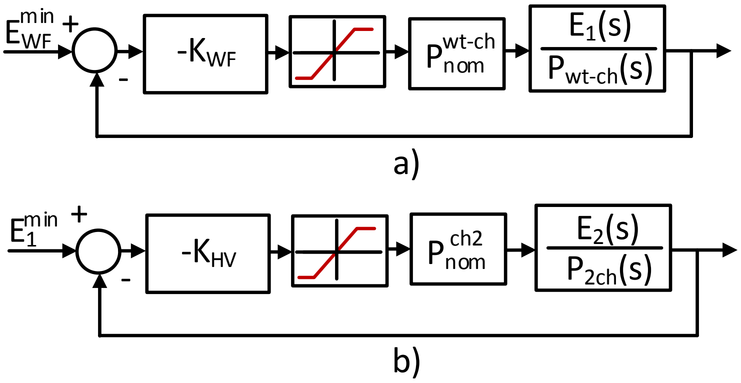

Figure 5.7: Block diagrams used to study the effects of the saturations

Figure 5.8 shows the frequency response of the transfer function, $\frac{E_1(s)}{P_{ch-wt(s)}}$, and the trajectory of the saturation describing function for different K_{WF} gain values. As can be observed, for values of K_{WF} smaller than 1/2700 the limit cycle disappears for the studied case (see parameters in section 5.7).

E_2^{min} **Selection** To avoid the connection ofHVDC-DBR during long faults, when the wind turbine power reduction is acting, the E_2^{min} should be tuned in order to start to act when the E_1^{max} is overpassed. E_2^{min} should be

$$E_2^{min} \geq \frac{\sqrt{E_1^{max} - 4P_{nom}R_{DC}} + E_1^{max}}{2} \tag{5.57}$$

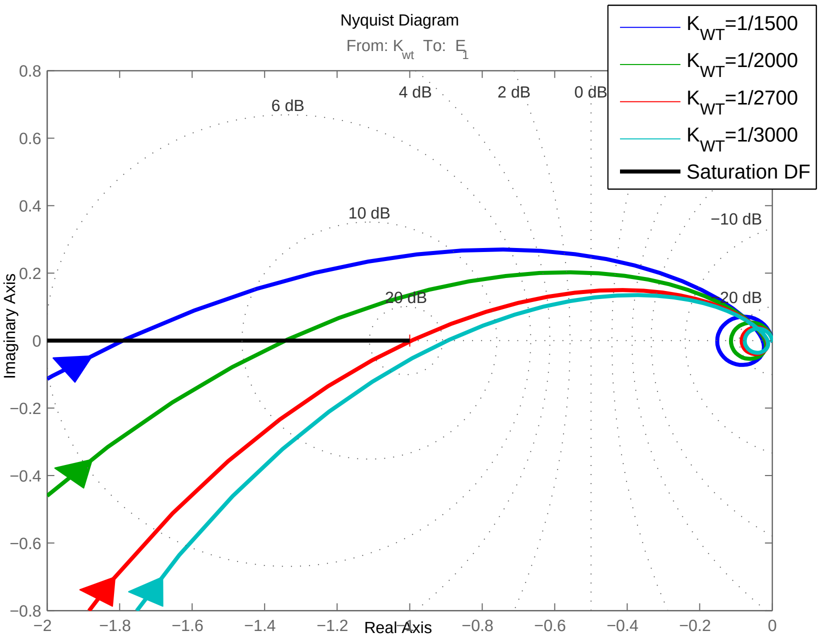

Figure 5.8: Nyquist plot used to determine the limit cycle limit for the K_{WT} gain.

A dead band is suggested to add to this minimum threshold in order to avoid interactions between controllers.

E_2^{max} Selection E_2^{max} is selected using the same procedure used to select E_1^{max}. In that case the studied transfer function is the relation between the HVDC bus voltage and the power dissipated by the HVDC-DBR $\frac{E_2(s)}{P2ch(s)}$. Figure 5.7 b) shows the block diagram of the studied close loop. As can be seen in Figure 5.9 the E_{wt}^{max} should be lower than $K_{HV} = \dfrac{1}{500}$ in order to avoid limit cycles.

5.6 Power reduction method implementation

The presented power reduction method needs a physical implementation in the offshore wind farm. A possible implementation is the generator torque

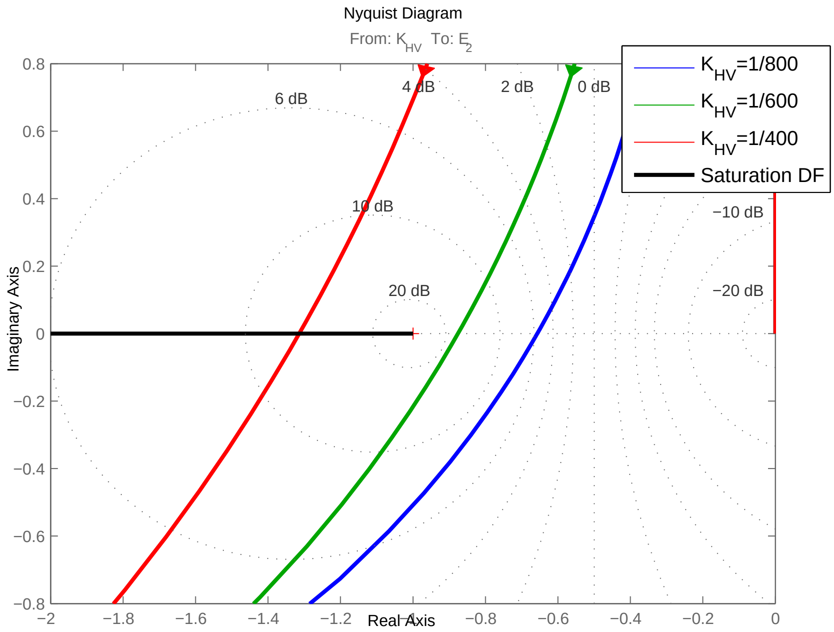

Figure 5.9: Nyquist plot used to determine the limit cycle limit for the K_{HV} gain.

reference reduction, but due to the considerable mechanical load effort on the wind turbine is suggested acting the pitch angle. Pitch angle is combined complementary with the WT-DBR that dissipates the power that cannot be reduce by the pitch mechanism due to its slow dynamics. The power reduction method modifies the pitch controller reference as

$$P^*_{wt} = P^{wt}_{nom} P^{red}_{wf} \tag{5.58}$$

where P^{wt}_{nom} is the wind turbine nominal power. The WT-DBR is controlled complementarily to the pitch system reducing the amount of power that cannot be reduced by the pitch. The power dissipated by the WT-DBR is calculated as

$$P_{ch-wt} = P_{wt} - P^*_{wt} \tag{5.59}$$

Furthermore, the power dissipated in the HVDC-DBR is calculated as

$$P_{2ch} = P_{2ch}^{red} P_{nom}^{2ch} \tag{5.60}$$

where P_{nom}^{2ch} is the HVDC-DBR nominal power. The wind farm power controller can be shown in Figure 5.1 as an extension of the wind farm control.

5.7 Simulation results

To test the proposed control scheme a simulation scenario has been performed using the MATLAB/simulink©. This simulation scenario consists of a power restriction in the power that can be injected by the GSC of the 20 % (e.g. due to a trip line) during 20s, starting at t=5s and finishing at t=25s. The parameters used in the simulation are:

Value	Parameter	Unit
E_2^*	300	[kV]
P_{nom}	100	[MW]
$Z_p = R_p + \jmath\omega X_p$	$0.25 + \jmath 1.57$	[Ω]
$Z_n = R_n + \jmath\omega X_p$	$0.502 + \jmath 1.025$	[Ω]
$Z_c = R_c + \jmath\omega X_c$	$0.35 + \jmath 1.1$	[Ω]
C_f	15	[μF]
C_c	2.1	[μF]
C_1	150	[μF]
R_1	1.5	[Ω]
L_1	6.8	[mH]
k_{droop}	1/10	[A/V]
E_1^{max}	307	[kV]
E_1^{min}	304	[kV]
E_2^{max}	307.7	[kV]
E_2^{min}	307.1	[kV]
v_{wind}	12	[m/s]
t_f	1	[s]

Table 5.1: Electrical and control parameters used in the simulation

Figure 5.10 shows the voltage and the power during the pre-fault, the fault and the fault recovery. As can be observed before the fault, the droop control action is controlling the DC voltage normally. When the power restriction occurs, the DC voltage rises intermediately, and the HVDC-DBR starts to dissipate the power that cannot be injected. As the fault last more than 1 second, the WTC begins to reduce the generated power gradually. First, the pitch reference is changed to be adapted to the new power reduction reference. As the pitch mechanism has a slow dynamic, the WT-DBR dissipates the power difference that can not be reduced by the pitch during t=6s and t=10s. As can be observed, the WT-DBR is reducing gradually the dissipated power, since the non control action. At t=25s, the power restriction is cleared and the system returns to work to the normal conditions.

Figure 5.11 shows the voltage evolution on the power steady state characteristics. The main operation points are

(1) Before the fault the system is regulated by means of the GSC voltage droop.

(2) The power is not controlled anymore due to the GSC saturation and the injected power is reduced drastically.

(3) Once the E_2^{min} is overpassed the HVDC-DBR starts to dissipate power and a new equilibrium point is reached.

(4) As the fault lasts for more than t_f the WF power reduction starts to act and the DC voltage is moved from the HVDC-DBR control to the WF power reduction control. In point (4) a new steady-state is reached.

(5) Once the fault is cleared, the systems returns to be controlled by the GSC droop characteristic

(6) After some seconds the system returns to the original point (1).

Figure 5.12 shows the system dynamics with $k_{WT} = \frac{1}{1000}$. As it can be observed a cycle limit exist in the E_2 voltage due to the inappropriate gain selection. In this case only the WT-DBR is only considered. If the pitch power reduction is also introduced the system response is even worse.

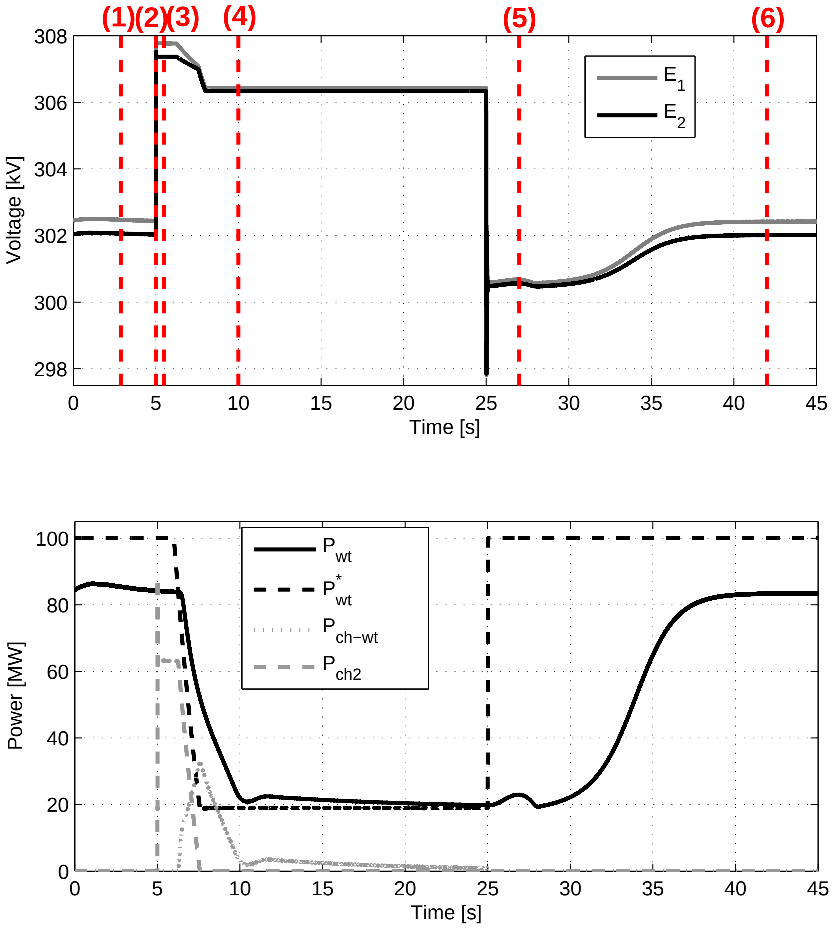

Figure 5.10: E_1 and E_2 voltage and power evolution

5.8 Conclusion

This chapter has introduced a coordinated power reduction method for faulty operation scenarios. The presented method allows the fault right through of an HVDC link for short and long faults using an HVDC-DBR and permits to reduce the generated power if the fault last in the time. To design the proportional controllers the non-linear describing function analysis tool has

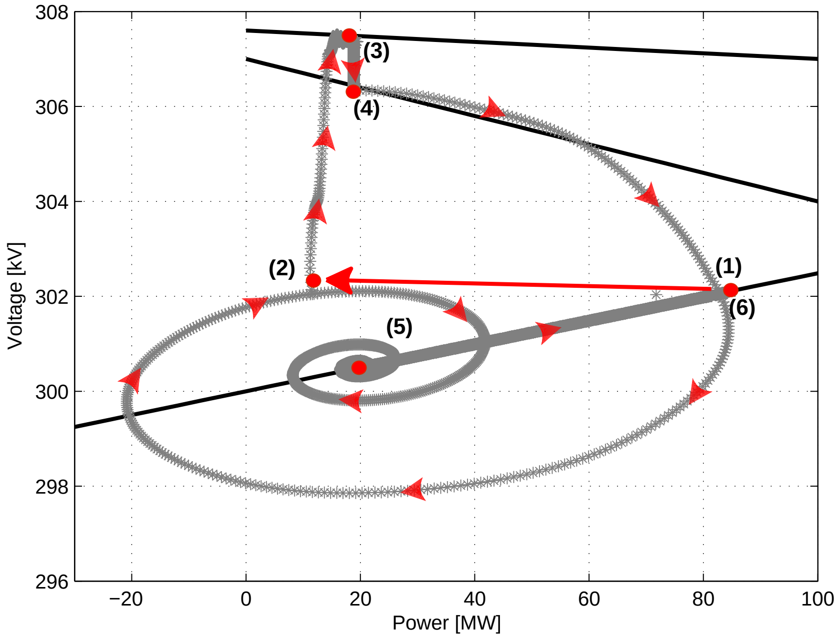

Figure 5.11: E_2 trajectory on the steady state characteristics (WF characteristic have been moved to E_2 values).

been used and a four-step methodology to determine the controller gains has been presented. The obtained controller have been evaluated under a dynamic simulation displaying good performance.

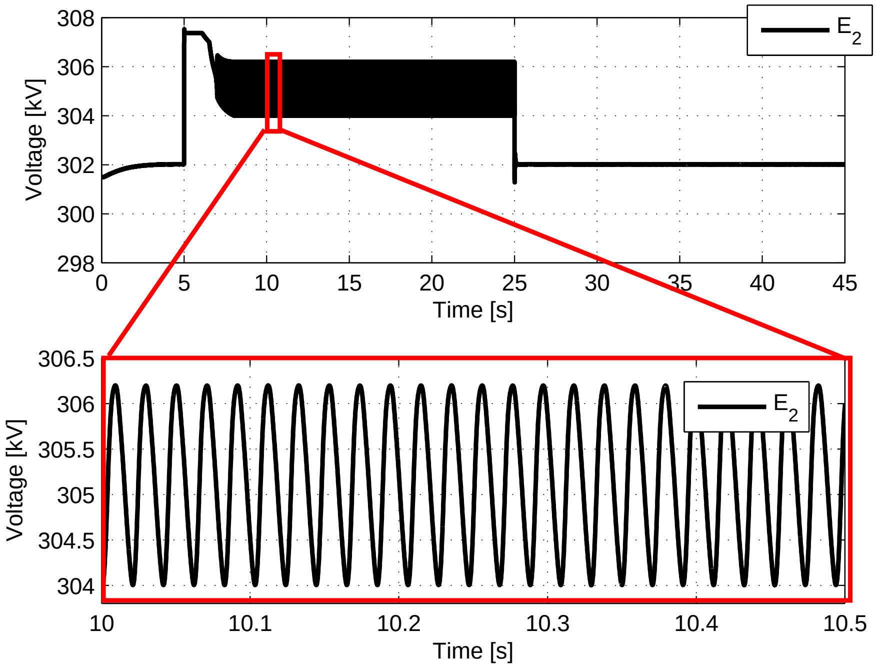

Figure 5.12: DC voltage at the GSC terminals, E_2, with a $k_{wt} = \frac{1}{1000}$

Chapter 6

Vector control for VSC connected to weak grids

6.1 Introduction

The connection point between the VSC and the AC system may be located remotely, leading to a weak or very weak SCR (<2). For HVDC systems based on Line Commuted Converters (LCC) there is a limitation on the minimum required SCR [39], but such a theoretical limit does not exist for VSC based systems [40]. This means that a VSC-HVDC converter is capable to interface with any kind of electrical grid and can potentially create a grid without synchronous generators (e.g. offshore wind power plants).

There are several proposed control techniques in order to inject power into an AC system using a VSC. One of the most widely used is the vector current control [41]. The vector current control is based on the control of two independent current components, q and d in the Synchronous Reference Frame (SRF) whilst the synchronization is provided by a PLL [17]. This control technique allows an independent control of active and reactive powers [42] with an fast dynamic response. Typically, the vector current control is considered as the inner control loop, and an outer control loop is added to manage the active power and the voltage/reactive power [26] for grid connected converters.

While this advantage from VSC over LCC is often mentioned when comparing both technologies, some studies have identified relevant drawbacks when vector current control is used in a low ($2 \leq \text{SCR} \leq 3$) or a very low (SCR<2) grid [43, 44, 45, 36]. First problem is the low frequency resonances that can interact with the vector current control [46]. Second problem is due to the PLL dynamics when the power converter is synchronized to a weak grid [36, 46]. Zhang et al. [36, 47, 48] proposed an alternative technique referred to as Power Synchronization Control (PSC), which does not require synchronization with a PLL) via emulating the behaviour of a synchronous machine. It is reported that PSC provides a good performance and fast dynamics for low SCR values. However, the main disadvantage of this topology is in dealing with faults in the AC grid, PSC switches to classical vector current control when the power converter current limit is reached [47].

The present chapter investigates the potential utilization of vector current control coordinated with an outer (voltage and power) control loop which is specially designed to enhance the VSC operation when connected to weak or very weak grids. The outer control scheme is based on the gain-scheduled multi-variable controller [46] - such gain-scheduling approach allows ensuring stable operation of the whole VSC operating range. A grid with SCR=1 is utilized as a benchmark. Recall that this value is related to the worst case scenario, for which the system stability and performance must be analysed and validated.

6.2 Analysed system

The analysed system is a VSC-HVDC power converter connected to a weak grid by means of an LC filter as shown in Figure 2.3.3. The grid is represented using a Thevenin equivalent and the overall system is to be modelled in the synchronous reference frame. The state space is composed by Eq.2.7 that reflects the dynamic equation and the system outputs are defined as

$$\Delta y_{lc} \quad = \quad C_{lc}\Delta x_{lc} \tag{6.1}$$

where y_{lc} is the electrical system output. It is defined as

$$y_{lc} = [\Delta V_z \ \Delta P]^T \tag{6.2}$$

where P is the active power at the PCC and V_z is the magnitude if the V_z voltage. The matrix C_{lc} is,

$$C_{lc} = \begin{bmatrix} 0 & 0 & \frac{\mathrm{v_{zq0}}}{\mathrm{V_{z0}}} & \frac{\mathrm{v_{zq0}}}{\mathrm{V_{z0}}} & 0 & 0 \\ 0 & 0 & \frac{3\,\mathrm{i_{lq0}}}{2} & \frac{3\,\mathrm{i_{ld0}}}{2} & \frac{3\,\mathrm{v_{zq0}}}{2} & \frac{3\,\mathrm{v_{zd0}}}{2} \end{bmatrix} \tag{6.3}$$

Table 6.1 summarizes the used parameters in the present study.

Parameter	Value	Units
Nominal Power	350	MW
Nominal Voltage	195	kV
SCR	1	
X_z/R_z	10	
Coupling inductance (L_l)	0.2	pu
Coupling resistance (R_l)	0.01	pu
Capacitor (C_f)	0.17	pu

Table 6.1: Parameters used in the study

For the phasor analysis presented in Section 6.3, the voltage $\underline{V_y} = V_{y\angle 0}$ of the grid Thevenin equivalent is considered as the slack and its angle is 0, $\underline{V_z} = V_{z\angle\delta}$ is the power converter voltage, $\underline{V_l} = V_{l\angle\theta}$ is the voltage at the PCC, $\underline{I_z}$ is the current through the grid and $\underline{I_l}$ is the current through the coupling filter. A sketch of the phasor analysed system can be seen in Figure 6.1

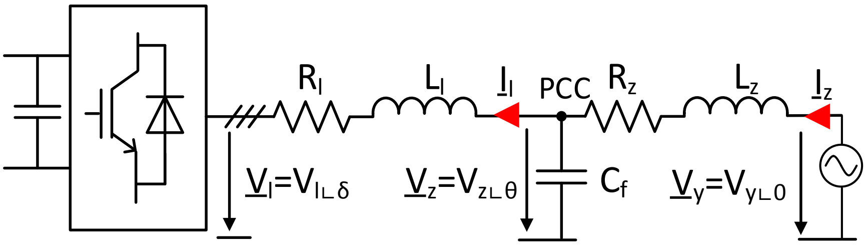

Figure 6.1: Model of the phasor analysed system.

6.3 Steady state capability

VSC-HVDC connected to strong grids present some limitations due to physical restrictions of the power converter, particularly maximum current and voltage. When VSC-HVDC is connected to a weak grid, the stability limit is also relevant. The steady state stability will determine the maximum amount of active and reactive powers that can be exchanged between the grid and the power converter.

Figure 6.2 shows the active power as a function of the angle δ ($\delta = [-90°, 90°]$) keeping the amplitude of $\underline{V_z}$ constant. The relation between the active and reactive power and voltages $\underline{V_y}$ and $\underline{V_l}$ are defined by,

$$\begin{aligned}
\underline{V_z} &= \frac{\underline{V_z}\,\underline{Z_f}\,\underline{Z_z} + \underline{V_y}\,\underline{Z_l}\,\underline{Z_f}}{\underline{Z_z}\,\underline{Z_f} + \underline{Z_z}\,\underline{Z_l} + \underline{Z_l}\,\underline{Z_f}} && (6.4)\\
\underline{I_l} &= \frac{\underline{V_z} - \underline{V_l}}{\underline{Z_l}} && (6.5)\\
\underline{S} &= P + \jmath Q = 3\underline{V_z}conj(\underline{I_l}) && (6.6)
\end{aligned}$$

where $\underline{Z_l} = R_l + \jmath\omega L_l$, $\underline{Z_z} = R_z + \jmath\omega L_z$ and $\underline{Z_f} = 1/(\jmath\omega C_f)$. As can be seen, the maximum power that can be inverted is different from the maximum power that can be rectified. When the power converter is in rectifier mode, the 90° are reached below $P = 1$ pu and when it is operating in inverter mode, the $-90°$ are reached above the active power unity. This restriction is caused due to the effect of the resistances [49].

From the voltage point of view, Figure 6.3 shows the relation between the amplitude of the voltage at the PCC, V_z, and the magnitude of the voltage at the power converter terminals, V_l, for different power factors and active power. As depicted in Figure 6.3, if 1 pu of active power has to be inverted, a large amount of capacitive reactive power is needed. Therefore, the power converter must be oversized (or alternatively an external reactive power source should be installed). For this reason, an LC coupling filter is used to provide reactive power support.

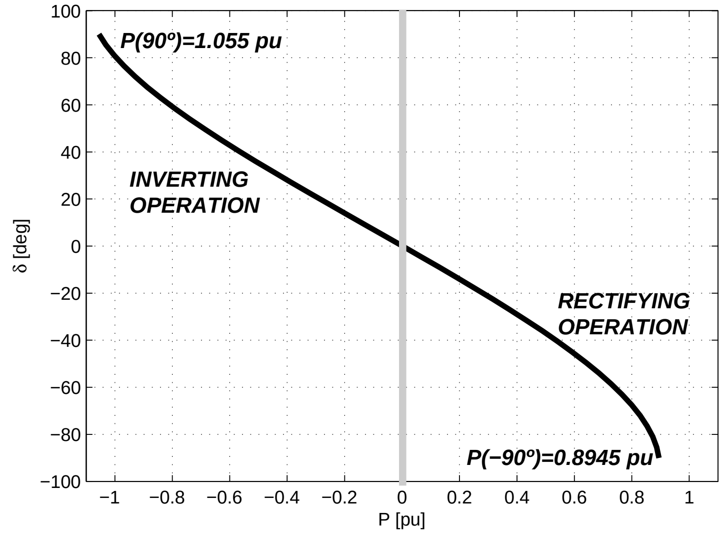

Figure 6.2: Active power exchanged between the VSC-HVDC terninals and PCC for a $\delta = [-90°, 90°]$.

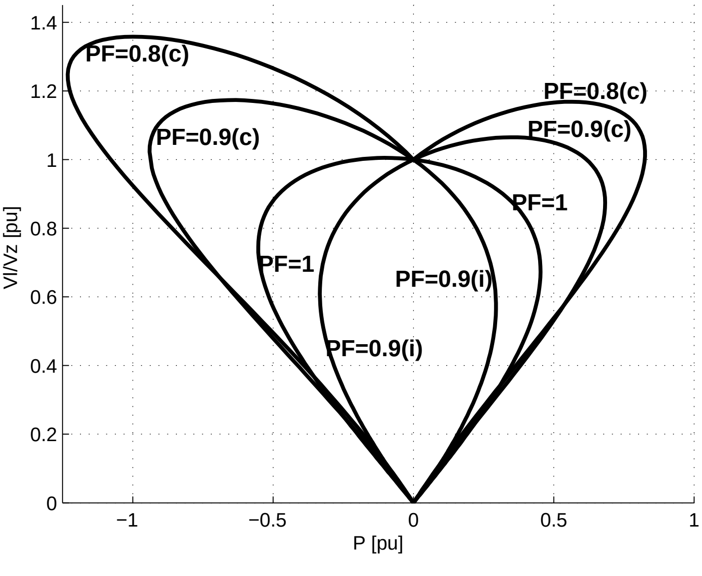

Figure 6.3: V_l/V_z curves as function of different power factors and active power.

6.4 Classic control approach

A classical control structure of the power converter for grid integration purposes based on vector current control is developed in two control levels, the lower level control (inner loop) and the upper level control (outer loop). The inner control is in charge of the regulation of the *qd* components of the current through the coupling filter. The outer control is in charge of the control of the active power and the magnitude of the voltage at the PCC. A sketch of the general structure is presented in Figure 6.4 and it is detailed in Section 2.8.

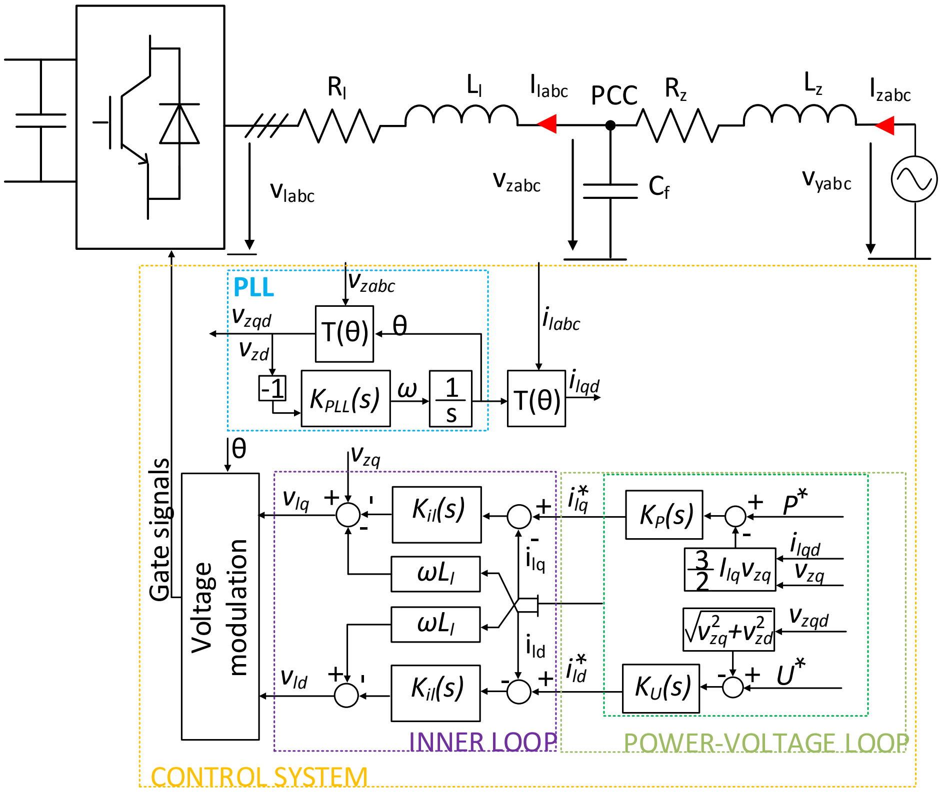

Figure 6.4: Scheme of the DC voltage droop implementation with a current control loop of a VSC connected to the AC grid by means of an LC coupling filter

6.5 Dynamic analysis with conventional VCC

Since the analysed system presents non-linearities, the dynamic equations are to be linearised in order to obtain and realize the stability studies. Such non-linearities are related to the active power (P), the magnitude of the voltage at the PCC (V_z) and the effect of the angle on the Park transformation and the inverse Park transformation. The linearised equations are the same as have been used in Chapter 5. The outer loop equations can be seen in Subsection 2.8. Figure 6.5 shows the connection of the linearised blocks.

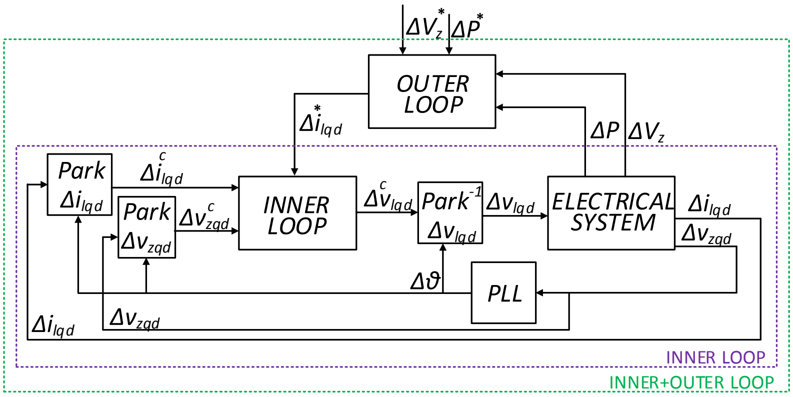

Figure 6.5: Scheme of the connection of the linearised system.

6.5.1 Frequency response and stability analysis of the inner loop

Figure 6.6 shows the poles and zeros configuration of the VSC-HVDC system using the inner loop only for different power values. Please note in this figure that the direction of the arrows start from P=-1 (inverting) to P =0.9 pu (rectifying). The system inputs are the current references i_{lq}^* and i_{ld}^*. The plant dynamics are linearised around the desired equilibrium points, in association with the operating points that permit the injection of the desired amount of power, yet retaining the voltage amplitude constant. As illustrated in Figure 6.6, the system poles are all located at the Left Hand Plane (LHP). Consequently, the vector current control and the PLL tuned using classical control approaches is stable for the full range of operation.

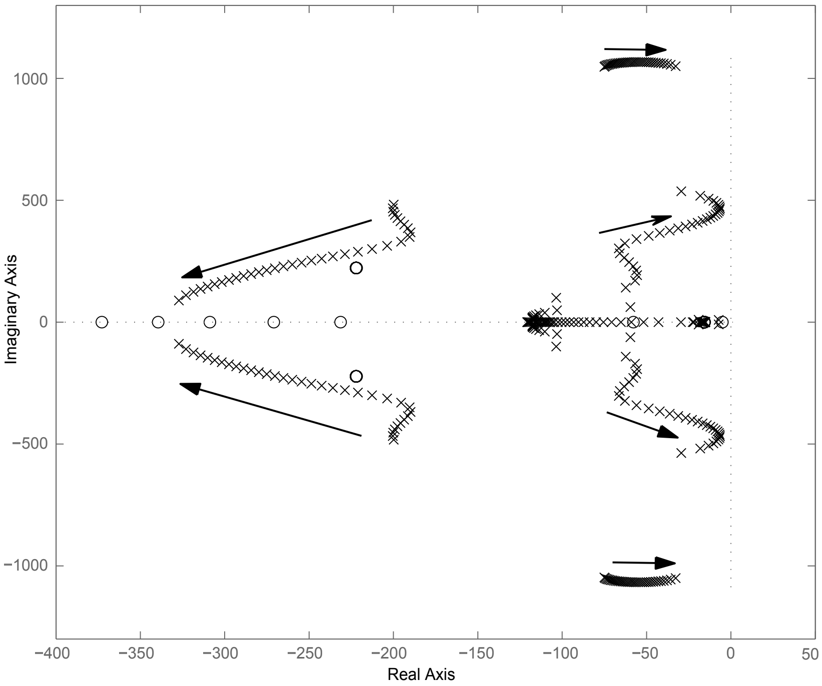

Figure 6.6: Poles and zeros map of the current loop dynamic system subject to variation of P =[-1,0.89] pu.

From the generic frequency analysis of the system, when a VSC-HVDC is connected to a strong grid the variation effect of the i_{lq}^* are mainly observed on the active power response and the variation effect of the i_{lq}^* are mainly observed on the voltage response. Consequently, it is assumed that the active power and the voltage amplitude at the PCC can be controlled independently.

Figure 6.7 shows the frequency response of the studied system. This frequency response is shown in four plots, the first column shows P and U response subjected to a i_{cq}^* component variation and the second column shows the same variables subject to a i_{ld}^* component variation. From the bode analysis at low frequency region, it is deduced that for small power values, the independent control between i_{ld}^* and U and i_{lq}^* and P is preserved, but when the power demand is higher the cross terms effects are not negligible and the independent component control is lost. In particular when the system is

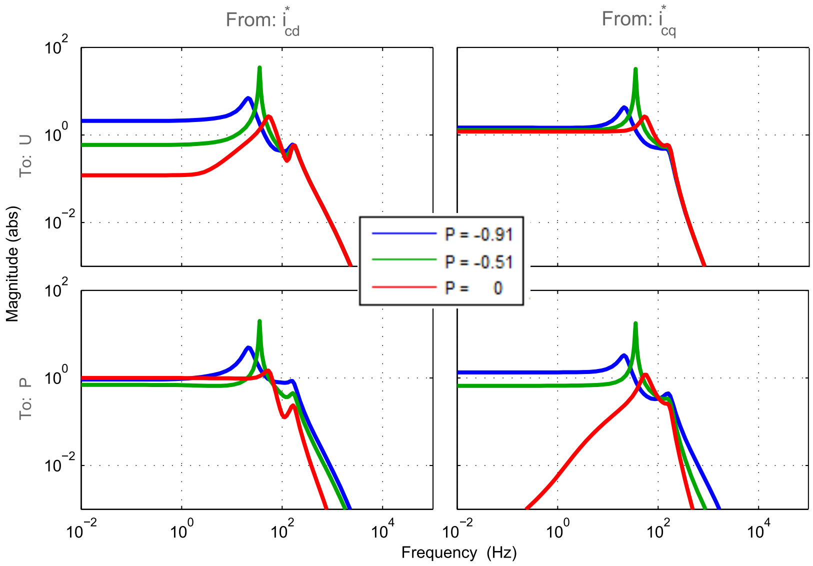

Figure 6.7: Bode frequency response of the system at different active power operation points (in PU).

operating near P =-1 pu (inverting mode), the effect of i^*_{lqd} changes on the power and voltage are almost identical. In other words, when a VSC-HVDC is connected to a weak grid there exists system non-linearities that do not permit an independent and decoupled control for high power values. This phenomenon is due to the large δ angle when the high active power is injected. Traditionally, as the power system is operating with δ below 30°, the system is considered to be linear as well as the voltage control is assumed through the reactive power control, but in the presence of a weak power system, this assumption can potentially be violated because the power and voltage control are mutually coupled.

6.5.2 Stability of the closed-loop system

Figure 6.8 shows the poles and zeros plot of the VSC-HVDC controlled by an inner current loop plus an outer current loop for inverting (upper graph) and rectifying mode (lower graph). The outer current loop is designed for the linear operation area ($\delta < 30°$). The arrow indicates the poles movement from P = -1 pu to P = 0 pu for the inverting operation mode and from

P = 0 pu to P =0.89 pu for the rectifying mode. For low power values (near the linear area) the system is stable in the inverting operational mode, but for higher values it is unstable, that is, the stability margin is located around P = -0.74 pu. This means that an outer loop designed for low power operations points is not suitable for the high power values due to the system non-linearities. A similar instability behaviour could result in the rectifying mode.

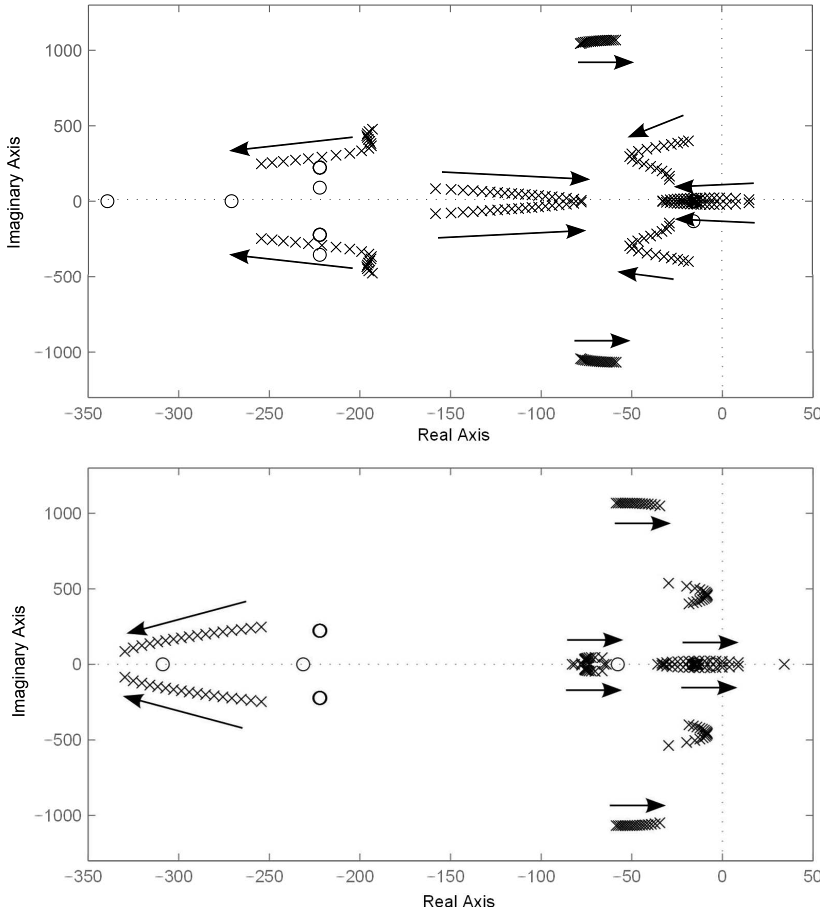

Figure 6.8: Poles and zeros map of the system using the classical upper level control at $P = [-1, 0]$ pu (upper plot) and $P = [0, 0.89]$ pu (lower plot).

6.6 Proposed advanced vector current control

From section 6.5, it is concluded that the vector current control, using a classical PLL, is stable and can drive the power converter in the operational envelope described in section 6.3. However, the classical outer loop for high power values is unstable. From this analysis, it can be deduced that the classical outer control is not appropriate for weak grids. To this end, a new upper level control considering the system non-linearities is introduced.

The proposed upper-level control consists of additional four decoupling gains between the voltage magnitude and power errors, e_u and e_p, before being processed by the PI. Furthermore, to overcome the non-linearities and obtain similar responses, a parameter-varying control scheme based on the gain-scheduling technique, is proposed for the decoupling gains and the PI controllers. The aim of the proposed control scheme is to robustly handle the interactions between the active power and voltage control. A block diagram of the proposed controller is shown in Figure 6.9.

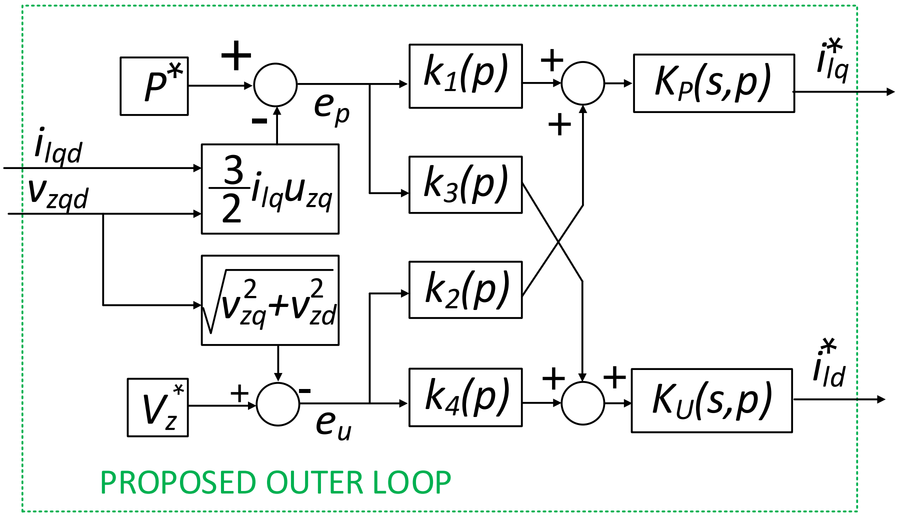

Figure 6.9: Proposed advanced outer loop control.

The controller can be described as

$$i_{lq}^* = K_P(s,p)(k_1(p)e_p + k_2(p)e_u) \tag{6.7}$$

$$i_{ld}^* = K_U(s,p)(k_3(p)e_p + k_4(p)e_u) \tag{6.8}$$

where, $k_1(p)$, $k_2(p)$, $k_3(p)$ and $k_4(p)$ are the decoupling gains (proportional gains) and $K_P(s,p) = (k_{p-p}(p)s + k_{i-p}(p))/s$ and $K_U(s,p) = (k_{p-u}(p)s + k_{i-u}(p))/s$ are proportional-integral (PI) power and voltage controllers.

With reference to Figure 6.9, the proposed advanced control system is indeed a multivariable (two-input two-output) dynamical system, whose inputs are $e_p(t)$ and $e_u(t)$ and outputs are i_{cq}^* and i_{cd}^*. Non-linear nature of the plant under investigation, this controller needs to be operating in the manner of gain-scheduling so as to handle the acquired number of feasible operational conditions. In fact, since the plant dynamics is highly non-linear due to the variation of the operating conditions, the control system performance degrades or closed-loop system even becomes unstable if the non-linearities are not taken into account. In this regard, a justified number of local controllers are to be designed accordingly for such operating points to provide weak AC system with robust stability (and robust performance, if any). For the purpose of the presented study, 35 local robust controllers have been designed based on the same number of operating points of the linearized dynamics that cover active power transmission distributed at $P = [-1.03, 0.89]$ pu.

There are eight control gains i.e. $k_1(p)$, $k_2(p)$, $k_3(p)$, $k_4(p)$, $k_{p-p}(p)$, $k_{i-p}(p)$, $k_{p-u}(p)$, and $k_{i-u}(p)$ that are tuneable gains (as design parameters) being tuned at particular operating condition. Remember that all these control gains are parameter-varying as functions of the scheduling parameter (p). Such scheduling parameter (p) in the design methodology is chosen to be active power at PCC (P). It is also possible to include other grid scheduling variables such as the voltage at PCC, which are not considered in this work and are remained as our future works.

For the purpose of tuning the above eight design parameters towards a gain-scheduling robust control system, the so-called H-infinity fixed-structure control design methodology is used [50, 51]. In fact, the H-infinity norm of the closed-loop transfer function is minimized using fixed-structure control systems using the H-infinity methodology at every operating condition. It turns out that robust stability and performance are effectively achieved at every operating condition, given the scheduling parameter i.e. active power (P). In order to solve this challenging control problem, the proposed approach is to utilise the gain scheduling approach with fixed-structure H-infinity controllers. To this end, first the plant dynamics are linearised at any particular operating points, and then relevant Linear Time Invariant (LTI) models are obtained. After obtaining this set of linearised plants, a set of fixed-structure H-infinity controllers are designed accordingly. Using a scheduling mechanism as a parameter feedback, the controller dynamics are smoothly changed based on the variation of the operating condition. The generalized plant dynamics will be also gain-scheduling as a function of operating conditions. For more information, interested readers are referred to [52] and other references therein.

It is worthwhile to emphasise that the H-infinity fixed-structure control design methodology, for a given operating condition, tunes eight design parameters at a single design. However, in fact it tunes four gains along with two PI controllers in one design. To this end, if the desired number of the plants is given (35 in the studied case), it is required to design an appropriate set of controllers for those plants, respectively, so that the gain-scheduling control system could provide robustly operation over the operating envelope. The number of chosen local controllers is a compromise between the complexity of the global control system and the overall system performance [53].

In the next step the designed global gain-scheduling H-infinity control system performance is tested and validated through numerical simulations.

6.6.1 Stability of the proposed control system

The stability of the proposed control system is analysed based on the eigenvalues of the linearised plant, as depicted by the pole-zero map in Figure 6.10. The arrows indicate the moving direction of the poles from $P =$ -1pu to $P =$ 0.89 pu. As it can be seen, the proposed control stabilises the system by retaining all the poles at the LHP.

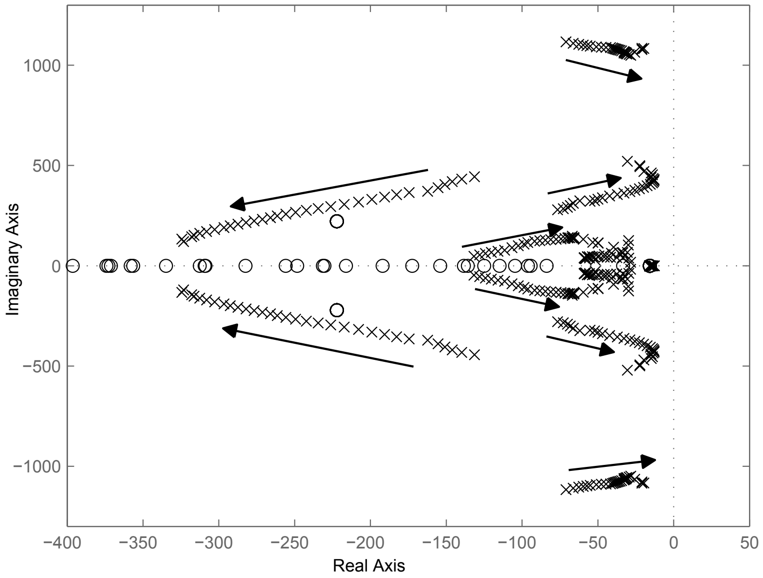

Figure 6.10: The system pole-zero map using the proposed advanced control based at P=[-1,0.89] pu.

6.7 Simulations results

Two simulation scenarios have been carried out to validate the proposed control system using MATLAB/Simulink modeling packages. The first simulated scenario is an active power ramp change and the second one is an active power step change scenario. An average VSC model is used for the purpose of validation of the proposed concepts throughout our simulations [42]. The variable gain controllers are dynamically implemented using lookup tables, meaning that the parameters change according to the power reference. For this simulations the controllers has been tune at: The current loop time constant have been tuned at $\alpha = 0.01$ ms. The PLL gains are $k_{p-pll} = 0.0028$ and $k_{i-pll} = 0.6199$. For the classical outer control loop the gains are: $k_{p-p} = -1.38e-7$, $k_{i-p} = 0.1017$,$k_{p-u} = -0.1143$ and $k_{i-u} = -0.1769$. The controller gains for the proposed control loop are specified in Tables 6.2 and 6.3.

P [pu]	k1	k2	k3	k4
-1.03	3.4×10^{-6}	3.4×10^{-6}	-1.1×10^{-7}	3.6×10^{-4}
-0.97	3.5×10^{-6}	3.5×10^{-6}	-6.5×10^{-8}	5.1×10^{-4}
-0.91	4.0×10^{-6}	4.0×10^{-6}	-5.5×10^{-8}	4.3×10^{-4}
-0.86	4.7×10^{-6}	4.7×10^{-6}	-4.8×10^{-8}	3.6×10^{-4}
-0.80	4.9×10^{-6}	4.9×10^{-6}	-4.4×10^{-8}	3.2×10^{-4}
-0.74	5.1×10^{-6}	5.1×10^{-6}	-4.8×10^{-8}	2.9×10^{-4}
-0.69	5.3×10^{-6}	5.3×10^{-6}	-5.1×10^{-8}	2.7×10^{-4}
-0.63	5.5×10^{-6}	5.5×10^{-6}	-5.3×10^{-8}	2.6×10^{-4}
-0.57	5.5×10^{-6}	5.5×10^{-6}	-5.1×10^{-8}	2.5×10^{-4}
-0.51	5.5×10^{-6}	5.5×10^{-6}	-4.8×10^{-8}	2.4×10^{-4}
-0.46	5.5×10^{-6}	5.5×10^{-6}	-4.6×10^{-8}	2.3×10^{-4}
-0.40	5.5×10^{-6}	5.5×10^{-6}	-4.4×10^{-8}	2.3×10^{-4}
-0.34	5.3×10^{-6}	5.2×10^{-6}	-4.0×10^{-8}	2.1×10^{-4}
-0.29	5.1×10^{-6}	5.1×10^{-6}	-3.9×10^{-8}	2.1×10^{-4}
-0.23	5.2×10^{-6}	5.2×10^{-6}	-3.7×10^{-8}	2.0×10^{-4}
-0.17	5.2×10^{-6}	5.2×10^{-6}	-3.6×10^{-8}	1.9×10^{-4}
-0.11	5.5×10^{-6}	5.5×10^{-6}	-3.6×10^{-8}	1.8×10^{-4}
-0.06	5.6×10^{-6}	5.5×10^{-6}	-3.6×10^{-8}	1.7×10^{-4}
0	5.6×10^{-6}	5.6×10^{-6}	-3.7×10^{-8}	1.7×10^{-4}
0.06	5.6×10^{-6}	5.6×10^{-6}	-3.8×10^{-8}	1.6×10^{-4}
0.11	6.0×10^{-6}	6.0×10^{-6}	-4.1×10^{-8}	1.5×10^{-4}
0.17	6.5×10^{-6}	6.5×10^{-6}	-4.4×10^{-8}	1.5×10^{-4}
0.23	7.0×10^{-6}	7.0×10^{-6}	-4.9×10^{-8}	1.4×10^{-4}
0.29	7.7×10^{-6}	7.7×10^{-6}	-5.2×10^{-8}	1.4×10^{-4}
0.34	8.3×10^{-6}	8.3×10^{-6}	-5.1×10^{-8}	1.3×10^{-4}
0.40	8.6×10^{-6}	8.6×10^{-6}	-4.6×10^{-8}	1.3×10^{-4}
0.46	9.5×10^{-6}	9.5×10^{-6}	-4.4×10^{-8}	1.3×10^{-4}
0.51	1.0×10^{-5}	1.0×10^{-5}	-3.6×10^{-8}	1.2×10^{-4}
0.57	9.9×10^{-6}	9.9×10^{-6}	-2.1×10^{-8}	1.1×10^{-4}
0.63	8.7×10^{-6}	8.7×10^{-6}	-6.2×10^{-9}	9.8×10^{-5}
0.69	8.4×10^{-6}	8.4×10^{-6}	3.9×10^{-9}	8.3×10^{-5}
0.74	9.1×10^{-6}	9.1×10^{-6}	1.4×10^{-8}	6.2×10^{-5}
0.80	1.1×10^{-5}	1.1×10^{-5}	3.0×10^{-8}	3.1×10^{-5}
0.86	1.3×10^{-5}	1.3×10^{-5}	5.0×10^{-8}	1.4×10^{-5}
0.89	-3.8×10^{-7}	-3.8×10^{-7}	-7.6×10^{-8}	1.2×10^{-3}

Table 6.2: Gains k_1, k_2, $k_3$and k_4 used in the simulations for the proposed control system depending on the power

P [pu]	k_{p-p}	k_{i-p}	k_{p-u}	k_{i-u}
-1.03	2.08	96.05	-39.98	-11496.55
-0.97	1.86	107.87	-33.43	-14211.97
-0.91	1.47	101.83	-29.09	-14090.54
-0.86	1.15	89.91	-25.29	-14081.28
-0.80	1.02	90.14	-21.20	-14075.20
-0.74	0.93	96.33	-15.67	-14022.22
-0.69	0.89	97.31	-12.38	-14022.21
-0.63	0.87	98.60	-9.42	-14022.19
-0.57	0.81	99.52	-6.08	-14022.19
-0.51	0.75	100.49	-2.91	-14022.19
-0.46	0.71	102.06	0.13	-14022.19
-0.40	0.65	103.29	3.05	-14022.19
-0.34	0.60	108.34	7.14	-14021.91
-0.29	0.58	113.17	10.08	-14021.80
-0.23	0.53	112.80	13.09	-14021.80
-0.17	0.50	114.83	16.07	-14021.80
-0.11	0.44	112.83	18.92	-14023.51
-0.06	0.41	115.01	21.05	-14027.49
0.00	0.39	118.41	22.91	-14024.16
0.06	0.39	125.39	24.55	-14023.98
0.11	0.36	125.88	25.89	-14023.96
0.17	0.34	126.36	26.90	-14023.90
0.23	0.33	129.22	27.64	-14023.36
0.29	0.30	128.79	28.41	-14022.68
0.34	0.27	128.15	29.54	-14022.59
0.40	0.24	129.15	30.91	-14022.55
0.46	0.19	128.36	32.61	-14021.81
0.51	0.16	128.29	34.31	-14023.13
0.57	0.16	127.86	35.40	-14023.09
0.63	0.17	128.40	35.28	-14023.06
0.69	0.17	128.84	34.43	-14029.27
0.74	0.17	128.66	31.20	-14028.93
0.80	0.15	131.62	24.63	-14028.78
0.86	0.13	125.52	3.11	-14143.88
0.89	9.63	51.76	32.41	-14712.57

Table 6.3: gains k_{p-p}, k_{i-p}, k_{p-u} and k_{i-u} used in the simulations for the proposed control system

6.7.1 Power ramp change

Figure 6.11 and Figure 6.12 show the active power, the voltage at the PCC (V_z) and the q and d components of the current in response to an active power ramp with a slope of 5 pu/s. Between $t = 0$ s and $t = 0.25$ s the system is injecting a power of 0.25 pu and the voltage V_z is kept constant. At time instant $t = 0.25$ s the injected power reference is changed and the system is tracking the reference satisfactorily. From the voltage point of view, there is a small increase of 0.04 pu. As is presented in section 6.3 the maximum power that can be inverted to the grid is 1 pu and this level is achieved successfully at $t = 0.8$ s. At time instant $t = 1$ s the active power reference is changed again and the system starts to reduce the inverted power and at $t = 1.35$ s the system achieves the maximum power that can be rectified, i.e. $P = 0.89$ pu for the system studied. During the transient, the power is followed with a reduced tracking error, but from the voltage point of view, a minimum voltage of 0.92 pu has occurred during the power reference change. Recall that this reduced level of voltage is due to high power demand rate ($5pu/s$) that could be very rare in practical applications. Although the performance of the overall system is acceptable, for slower power reference rates, however, the level of the voltage will be better than such worst-case value raised due to such high power demand rate. From the currents point of view, the i_{lq} component variation, during the ramp change, follows the active power reference change. The i_{ld} component is also following the voltage requirements satisfactorily.

6.7.2 Step change

Figure 6.13 shows the active power and the magnitude of the voltage U at the PCC during the power step change. From time instant $t = 0.25$ s, a step change is applied over a period of 200 ms. From the power point of view, it can be seen that the reference is tracked and the new power point is reached in less than 50 ms. From the voltage point of view, however, a small damped oscillation is realised around ± 0.07 pu, as expected.

Figure 6.14 shows the same step pattern of the active power and the amplitude of the PCC voltage V_z at the PCC in Figure 6.13 but using the conventional Vector Current Control. As it can be observed, both controllers

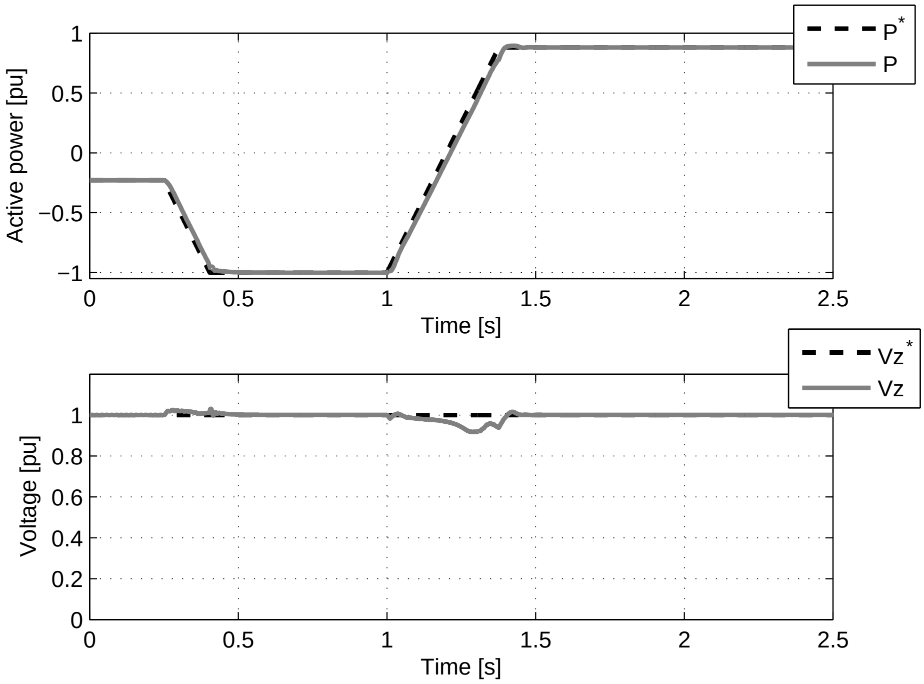

Figure 6.11: Active power and V_z voltage magnitude subject to a ramp change.

result in acceptable behaviour for low powers, approximately below 0.7 pu, but for higher power values the convectional control is unstable. This confirms the conclusion draw in Section 6.5.2, in the validation of the fact that the system is unstable for power values above 0.74 pu.

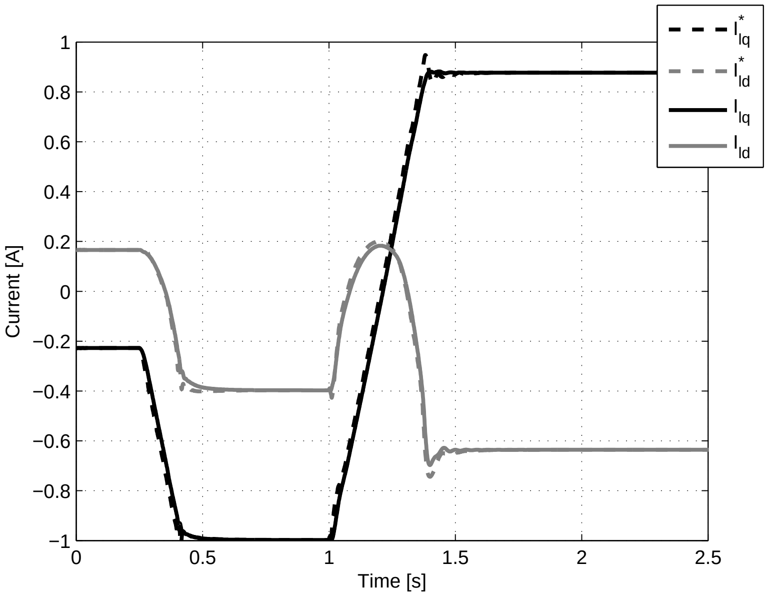

Figure 6.12: Reference and real value of the current component q and d.

6.8 Conclusions

This chapter has addressed an advanced gain-scheduling control system design methodology for VSCs connected to weak AC grids. Each controller can be designed in a way to guarantee robust stability and performance for any operating condition. As a result, the outcome of such advanced control is to provide an extended operational area of a VSC for a weak grid operation.

This chapter has explored and clarified that conventional vector current control systems have severe shortcomings in dealing with high-power demands at the weak grids. This is mainly due to severe system non-linearities as well as highly-coupled active power/voltage interactions, which makes the control of the VSC in connection with weak AC grids a very challenging problem. The simulation results illustrate that the proposed advanced control seems to be a very promising approach in tracking such challenging control applications.

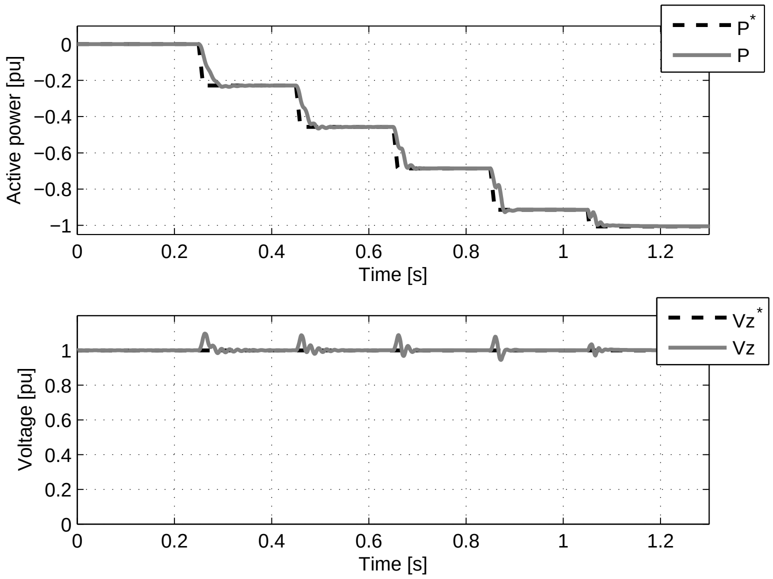

Figure 6.13: Active power and V_z voltage magnitude in response to changes in active power demand.

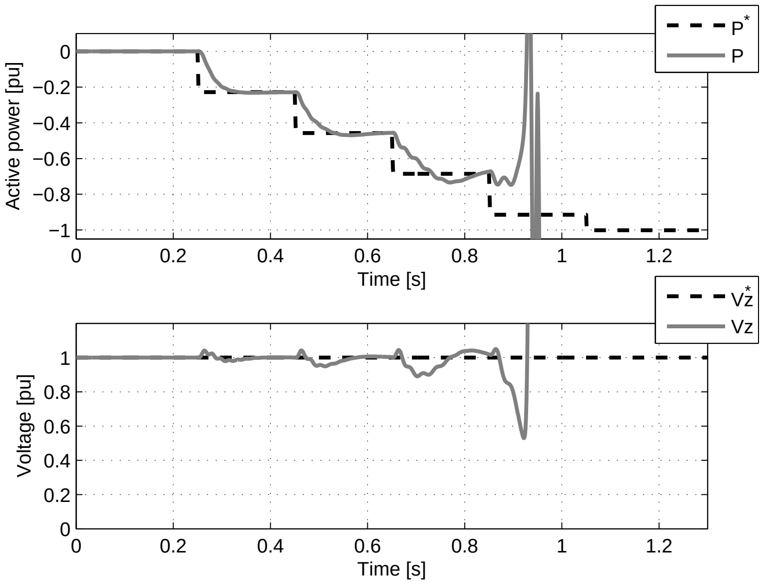

Figure 6.14: Active power and V_z voltage module in front of step change using the classical control structure.

Chapter 7

Hierarchical power control of multiterminal HVDC grids

Different ways to control the DC voltage in a DC grid have been described in literature, and there is a general tendency to favour droop-based control methods (an overview of the different methods is given in[22]). From the point of view of power flow control, the droop control as such does not allow to allow the power that is injected by a converter due to constant variations in operation points. If the droop control action is in effect, for example, after a converter outage, the powers change according to the droop characteristics and do no longer reflect the pre-fault values. For this reason, outer control loops are required to control the droop setpoints and thereby the converter powers. Some authors propose a centralised controller which sets optimized voltage references to the local controllers [54] using a fast communications system. Others propose to design the power controller based on droop regarding the power flow control in the steady state [19, 25].

In this chapter a hierarchical control scheme is presented. The objective of the proposed control structure is to allow power flow control in the DC network while ensuring that the terminal voltages are maintained stable within appropriate limits. This is achieved by designing a hierarchical control structure where the power flow (high level) controller sets the references for the voltage (low level) control. The proposed structure is comparable to the classical AC control system and allows for an integrated management of the MT-HVDC regarding the DC voltage and the power flow control. The cascaded interaction between controllers, considering slow communications, makes the implementation of the proposed control feasible in a real system.

Aspects such as the degraded operation or the power rescheduling after a contingency have been considered. First the DC voltage droop control is discussed. The resemblance with the AC primary control is shown. In the next step, the power control is introduced and discussed and its similarities with the AC secondary control mechanism are shown. Furthermore, the operating points and modes of the MT-HVDC are described. The proposed control structure also allows the introduction of a tertiary control mechanism, which is rather an optimization than a control in itself and therefore not dealt with in detail in this chapter. Finally, simulation results for various scenarios show the validity of the proposed method to control the power flows.

7.1 Control structure description

7.1.1 Balancing generation and load

One of the fundamental controls in electric grids manages the balance between generation and load. Put differently, the balance between the injected and withdrawn power in a grid must remain equal. In AC systems, this balance is reflected in the value of the frequency. The power balance is maintained by the frequency control mechanism. This mechanism adjusts the power outputs of the generation (or possibly the load) to assure a constant frequency. Although different implementations exist throughout the world [55], the control reactions can be generally subdivided in three time domains with different specific actions in each[1] (Figure 7.1 [56]).

The first control action is an automatic reaction of all activated generators after a deviation of the frequency from the nominal frequency. In a multi-zonal system, this results in a change of output power throughout the system. The power deviation is proportional to the frequency deviation (droop control). The primary control is activated in a very short time period (15-30 seconds) and acts to limit the frequency deviation. The set-point for the active power injections in the different generating units during the primary control action remains at the initial value. The primary control actions are available for only a limited time period (e.g. 15 minutes).

---

[1] Note that fourth control action, time correction, is not discussed here.

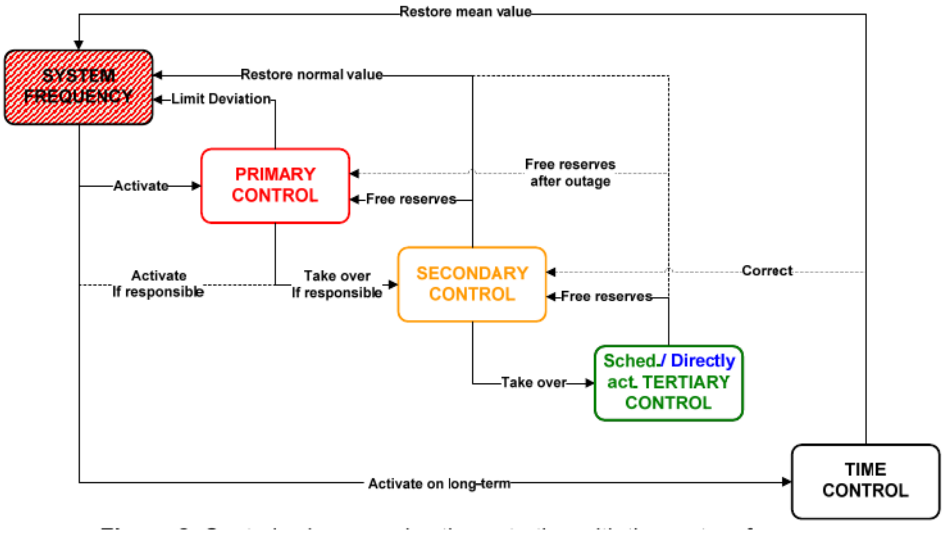

Figure 7.1: Different control actions in AC systems and their linkage.

The secondary control action restores the original exchanges between different zones, causing the ACE (Area Control Error) to get back to zero. The secondary control action changes the active power set-points in the area with a power deficit or excess to match the original schedule. Due to the change in set-point in the affected zone by the secondary control, the previously committed primary reserves are no longer required, and in fact overcompensate the initial fault. This effect is again automatically cancelled by the primary control action which moves back to the original value in the entire system, thus releasing the previously activated primary reserves. The tertiary control action shifts the power from the secondary reserves, which are available on a short time basis to more long term power generation, and is often manually activated by the system operator as the result of a system optimization.

7.1.2 Balancing injections to and from the DC grid

The power exchange to and from the DC grid have to be balanced in a similar manner as the AC system [57]. Where the AC system power balance is reflected in a constant frequency, the DC voltage perform a similar role in the DC system. The power-frequency control in the AC system is therefore very similar to the power-DC Voltage control scheme. Several control schemes have been proposed in literature [19, 58, 54]. The consensus seems to lead to a droop-controlled DC voltage [22, 25, 59, 60], much like the primary control actions which are used in AC systems. This shift complicates the power control in the system, making it not possible to copy the AC control methodology. Contrary to the AC system, which exhibits a significant inertia from the kinetic energy in the rotating machines, the stored energy in the DC system is very limited, with only the charge in the DC capacitors and cables. This makes that the voltages in the DC system change much faster than in the AC case (frequency power imbalance). The response of the controllers should therefore be equally fast. The time constant for the primary control loop is in the order of a ten's of milliseconds and is thus dictated by the DC grid characteristics. For the secondary control this can be relaxed as the primary response already aims at stabilizing the system voltage. Consequentially, this control can be in the order of seconds or tens of seconds. Traditional tertiary controllers are off-line algorithms that react between 20 minutes and 1 hour. Similarly as with the AC system, when a fault occurs (e.g. when a converter station is disconnected), the control of the DC voltage causes the different converter systems to adjust their power injections immediately, distributing the deficit according to the droop settings. As the voltage control at the DC side directly influences the power exchanges, there is a need to adjust the power injection set-points to meet the scheduled exchanges, especially if multiple zones or synchronous zones are connected to the DC grid. This requirement is very much in line with the secondary and tertiary control which is used in the AC system.

The proposed control scheme introduces an upper level controller to the HVDC voltage control which can be compared to classical AC grid controls, consisting out of a primary, secondary and tertiary control [61]. This structure allows the creation of an easy interaction between power dispatch and the lower controllers using a methodology which is well-accepted and known in the power sector.

A voltage controller is implemented in each VSC power converter and acts as a primary controller. Secondary control, or power control, is implemented

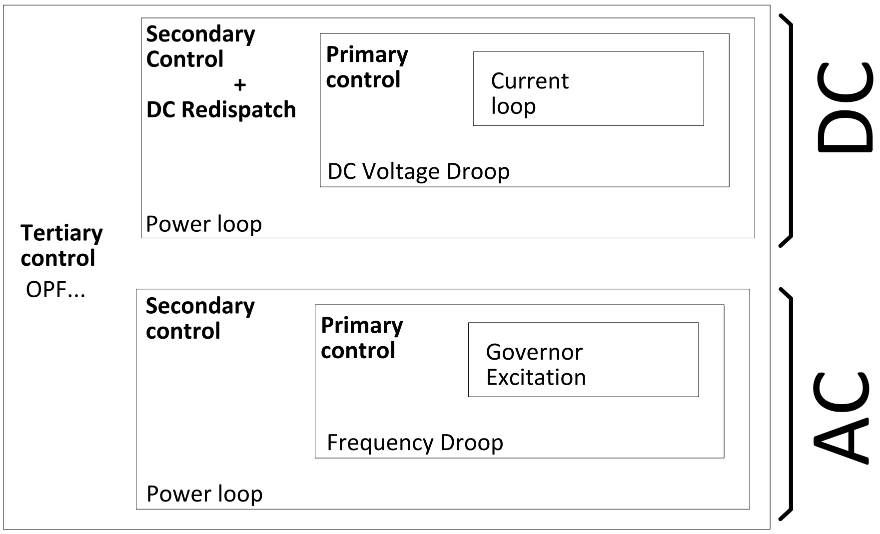

Figure 7.2: Comparison between AC and the proposed DC control approach.

to correct the exchanges so that the pre-disturbance conditions are restored. The practical implementation is a change of the voltage set-points in the affected VSC controllers. The new set-points are provided by a system-wide DC redispatch. Finally a tertiary control mechanism can be used to calculate the power reference according to a more optimal operation of a power system considering market, losses, security, current and voltage restrictions, environmental constrains, among others. Tertiary control can be based on OPF (Optimal Power Flow) algorithms considering AC and DC grids. Figure 7.2 shows a comparison between the AC and the proposed DC control approach.

7.2 Control implementation

7.2.1 Current loop

The current loop is the basic control loop for a VSC. This loop allow the injection of the desired active and reactive current to the electrical grid. Further information about the current loop can be seen in section 2.5.1.

7.2.2 Primary control

The primary control or voltage control is the controller in charge of the DC voltage in the case a droop controller is selected. It is a proportional control law that controls the DC current according to the DC voltage. More information can be seen in Subsection 2.7.2. The droop implementation for a rectifier and an inverter converter are defined respectively as

$$I^*_{in-rec} = k_{droop}(E^*_{rec} - E_{rec}), \tag{7.1}$$

$$I^*_{in-inv} = k_{droop}(E_{inv} - E^*_{inv}), \tag{7.2}$$

with I^*_{in} the reference current, k_{droop} the gain of the droop controller, E^*_{inv} the voltage offset for the inverter units and E^*_{rec} the voltage offset of the rectifier units.

Figure 7.3 shows the operation characteristic of the droop controller under inverter operation (a), and rectifier operation (b). Once the power converter current limit is reached the current is saturated and no more power is injected to the grid. The droop gain k_{droop} is calculated following the methodology presented in [59].

Wind farms connected to the DC grid are set to inject all the generated power in the DC grid. When an electrical fault occurs, it may result in the saturation of the power converter current limit and, consequently, not all the power can be injected in the grid. As such, the DC voltage will rise quickly. In order not to exceed the maximum permitted voltage, a wind farm power reduction method is needed. The power reduction method uses a droop characteristic that reduces the injected power. This power reduction can be physically implemented using a DC chopper or a wind turbine reference change. Using the last option, the power reduction control law is defined as

$$P^{red}_{wf} = P_{wf}(1 - K_{WF}(E_{DC} - E^{min}_{WF})), \tag{7.3}$$

where P_{wf} is the wind farm power, P^{red}_{wf} is the reduced wind farm power,

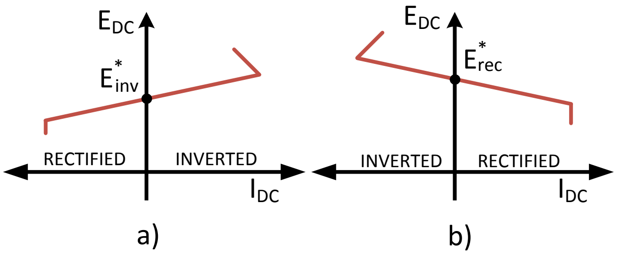

Figure 7.3: Droop characteristics depending on the operation of the system.

E_{DC} is the DC voltage and K_{WF} can be chosen as

$$K_{WF} = \frac{1}{E_{WF}^{max} - E_{WF}^{min}}, \tag{7.4}$$

where E_{WF}^{max} and E_{WF}^{min} are the upper and the lower thresholds of the DC voltage in terminals of the wind farm power converter.

7.2.3 Secondary control

The secondary control or power control can be described as a system that allows us to achieve the power setpoints provided by a tertiary control. Furthermore, the secondary control corrects the power references after a contingency. In steady state, the main objectives of the secondary control are to ensure the power references and the power exchanges between the areas. A conceptual scheme of the proposed system can be seen in Figure 7.4.

The secondary controller is the link between the tertiary and the primary control. The power controller is divided in two parts. The first part is located in the power converter and aims to achieve the given power references modifying the droop offset. This comes down to changing the intersection with the voltage axis E^* in Figure 4. The second part is located remotely and performs the calculations that allows us to calculate new power references in case of a change of the operational point.

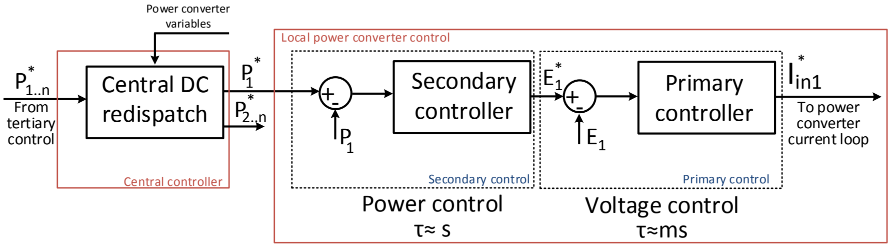

Figure 7.4: General scheme of the proposed control methodology

Local control structure

The local power control is based on a PI controller that achieves the desired power references without steady state error. The power controller regulates the power through the power converter by modifying the reference of the droop controller E_k^*. The output of the power controllers are saturated in order not to exceed converter voltage and current.

The power controller can be defined as $E_k^*/(P_k^* - P_k) = K_{p-pp} + K_{i-pp}/s$, where K_{p-pp} is the proportional gain of the controller and K_{i-pp} is the integral gain of the controller. The controller is tuned to obtain a time response in the order of seconds.

Central DC redispatch

The central DC redispatch recalculates the power references in case of a contingency (e.g. converter outage) or a deviation of the power references (e.g. change in power injection from an offshore wind farm). The central DC redispatch consists of a centralised controller that receives status information from the power converters, as well as the power references given by the tertiary control. The outputs are then sent new power references.

In normal operation, the sent power references match those provided by the tertiary control and no reference modifications are required. In case of a power converter disconnection, the given references cannot be maintained. In this case, the central DC redispatch tries to restore the power exchange between areas. This means that if one area is supplied by two power converters and one power converter is disconnected, the control objective is to

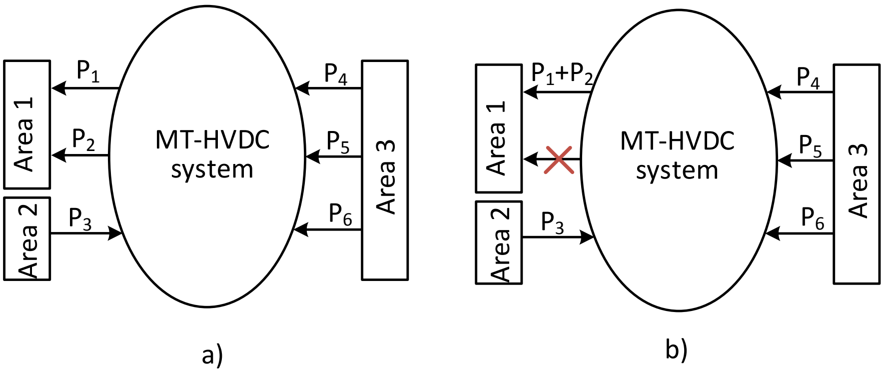

Figure 7.5: Example of power balancing developed by the reference calculation.

restore the scheduled power flow to or from this area. This is done by having the second converter take over the power from the converter facing an outage (as long as internal control limits are not hit). This is shown in Figure 7.5.

The operation of the mentioned central calculation structure requires a communication system between the local power converter and the central calculation itself. Compared to other systems [54, 19], the described system does not require a critical communication system due to the intrinsic safe operation characteristic of the droop-based primary control method.

Operating points

During normal operation, the power controllers modify the offset of the droop controller, i.e. the intersection with the voltage axis E^*, to achieve the desired power flow through the power converter. In normal operation the voltage can vary between a minimum and maximum value, as shown in Figure 7.6.

When the system operates in a degraded state, e.g. an AC voltage sag or a power converter disconnection, the power balancing in the system cannot be accomplished. In this case, the operation of the system moves to a fixed droop offset. The droop offset is limited in the upper region by the E_{max-i} and E_{max-r} and the lower region by the E_{min-i} and E_{min-r}. The subscript i

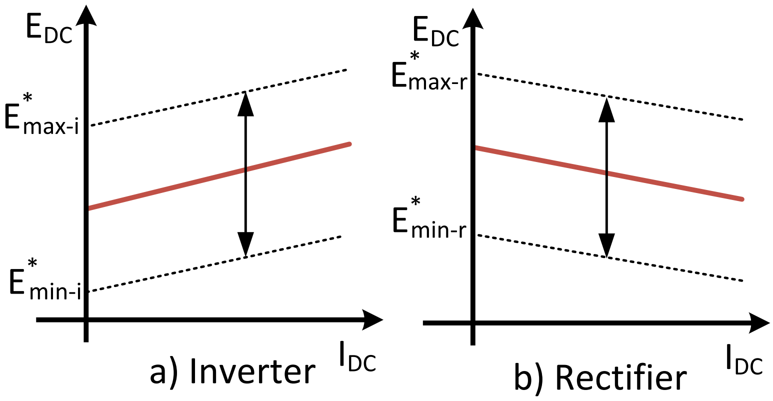

Figure 7.6: DC characteristic operation of the power converters for the proposed control methodology.

refers to inverter and r to rectifier. The appropriate selection of the described limits permits to operate the system under fault operation without exceeding the voltage limits while operating the system as an usual MT-HVDC droop controlled system.

7.2.4 Tertiary control

The tertiary control is the upper control level and schedules the injections according to a given objective function taking into account economical and technical aspects, as well as their constraints. The tertiary control can be based on OPF algorithms. The required tertiary control used in the presented scheme can be a classical tertiary control based on a power flow considering DC transmission systems [61]. Resistive losses are considered in this stage of the system and are included in the OPF calculation.

7.3 System modelling and controller design

In this section the DC grid and wind farm modelling are presented for a four terminals and three lines MT-HVDC scheme (Figure7.9). Furthermore, the linearised model used to study the system stability and select the control gains is introduced. The DC grid is connected to a strong AC grid, in order to simplify the study. Hence, only the DC grid dynamics are considered.

7.3.1 DC grid modelling

The DC grid cables are modelled as π equivalent cables and power converters are modelled as a current source [25]. For the devices that interconnect the DC grid with and AC grid the selected input variables are the DC currents (controller output) and the output variables are the DC voltages at the capacitor and the power in the converter terminals. For the device that interfaces a wind farm with the DC grid the selected input variable is the generated power and the output variable is the DC voltage. Equations 7.5 and 7.6 show the state space representation. As the power is the product of two variables, the system needs to be linearised in order to apply the traditional control design and analysis techniques. It is linearised as

$$\begin{aligned} \Delta\dot{x}_{dc} &= A_{dc}\Delta x_{dc} + B_{dc}\Delta u_{dc} && (7.5)\\ \Delta y_{dc} &= C_{dc}\Delta x_{dc} && (7.6) \end{aligned}$$

where the matrix gains are

$$A_{dc} = \begin{bmatrix} \frac{-P_{10}}{CE_{10}^2} & 0 & 0 & 0 & \frac{-1}{C} & \frac{-1}{C} & 0 \\ 0 & 0 & 0 & 0 & \frac{1}{C} & 0 & 0 \\ 0 & 0 & 0 & 0 & 0 & \frac{1}{C} & \frac{-1}{C} \\ 0 & 0 & 0 & 0 & 0 & 0 & \frac{1}{C} \\ \frac{1}{L_1} & \frac{-1}{L_1} & 0 & 0 & \frac{-R_1}{L_1} & 0 & 0 \\ \frac{1}{L_2} & 0 & \frac{-1}{L_2} & 0 & 0 & \frac{-R_2}{L_2} & 0 \\ 0 & 0 & \frac{1}{L_3} & \frac{-1}{L_3} & 0 & 0 & \frac{-R_3}{L_3} \end{bmatrix} \tag{7.7}$$

$$B_{dc} = \begin{bmatrix} \frac{1}{cE_{10}} & 0 & 0 & 0 \\ 0 & \frac{-1}{C} & 0 & 0 \\ 0 & 0 & \frac{1}{C} & 0 \\ 0 & 0 & 0 & \frac{-1}{C} \\ 0 & 0 & 0 & 0 \\ 0 & 0 & 0 & 0 \\ 0 & 0 & 0 & 0 \end{bmatrix} \tag{7.8}$$

$$C_{dc} = \begin{bmatrix} 1 & 0 & 0 & 0 & 0 & 0 & 0 \\ 0 & 1 & 0 & 0 & 0 & 0 & 0 \\ 0 & 0 & 1 & 0 & 0 & 0 & 0 \\ 0 & 0 & 0 & 1 & 0 & 0 & 0 \\ 0 & I_{in20} & 0 & 0 & 0 & 0 & 0 \\ 0 & 0 & I_{in30} & 0 & 0 & 0 & 0 \\ 0 & 0 & 0 & I_{in40} & 0 & 0 & 0 \end{bmatrix} \tag{7.9}$$

$$D_{dc} = \begin{bmatrix} 0 & 0 & 0 & 0 \\ 0 & 0 & 0 & 0 \\ 0 & 0 & 0 & 0 \\ 0 & 0 & 0 & 0 \\ 0 & E_{20} & 0 & 0 \\ 0 & 0 & E_{30} & 0 \\ 0 & 0 & 0 & E_{40} \end{bmatrix} \tag{7.10}$$

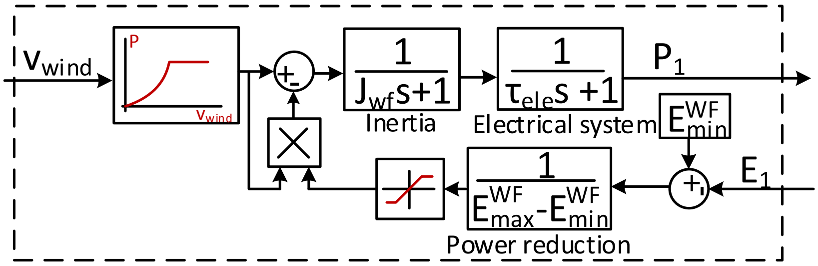

Figure 7.7: Wind farm simplified model

and the state, input and output vector are

$$x_{dc} = [\Delta E_1\ \Delta E_2\ \Delta E_3\ \Delta E_4\ \Delta I_1\ \Delta I_2\ \Delta I_3]^T \tag{7.11}$$

$$u_{dc} = [\Delta P_1\ \Delta I_{in2}\ \Delta I_{in3}\ \Delta I_{in4}\ ]^T \tag{7.12}$$

$$y_{dc} = [\Delta E_1\ \Delta E_2\ \Delta E_3\ \Delta E_4\ \Delta P_2\ \Delta P_3\ \Delta P_4]^T \tag{7.13}$$

where ΔI_{xin} is the converter injected current, ΔP_x is the power exchanged, ΔE_x is the voltage at the converter terminals and ΔI_x is the current through the cables.

7.3.2 Wind farm modelling

The wind farm has been modelled as a simplified power-aggregated model based on [62] and shown in Figure 7.7. The main objective of the proposed model is to reflect the power variation due to the wind speed variation. For this reason, the wind farm consist of a table that varies the injected power as a function of the wind speed according to a wind turbine power/wind speed characteristic [62]. After, this power is filtered by the rotor inertia dynamics ($G_{mec}(s) = 1/(J_{wf}s + 1)$), where J_wf is the rotor time constant inertia and the simplified electrical dynamics ($G_{ele}(s) = 1/(\tau_{ele}s + 1)$), where τ_{ele} is the electrical time constant. Furthermore, the power reduction described in subsection 7.2.2 is also implemented.

7.3.3 Control Design

The local secondary control structure presented in 7.2.3 is a cascade control structure where the inner loops are faster than the outer loops avoiding non-desired interactions between controllers. Figure 7.8 shows the connection of the DC grid linearised model and the power converter control. The current loop is tuned using the Internal Model Control (IMC) method, described in [63] ensuring a first order response with a τ_{il} time constant (see Subsection 2.5.1 for more tuning details). For the DC side point of view, if the power converter is in normal operation, the close loop dynamics is represented with the first order transfer function with a τ_{il} time constant. The primary or droop control is tuned in order to avoid DC grid resonances, and to minimise the droop's interaction with the other droop controls. More information about the droop tuning is found in [25]. The proposed secondary control is tuned in order to have a very smooth transient response. To have a reaction time around some ms, it should be almost 100 times slower than the primary control. In addition, a Low Pass Filter (LPF) has been added to the measures in order to filter the measurement noise.

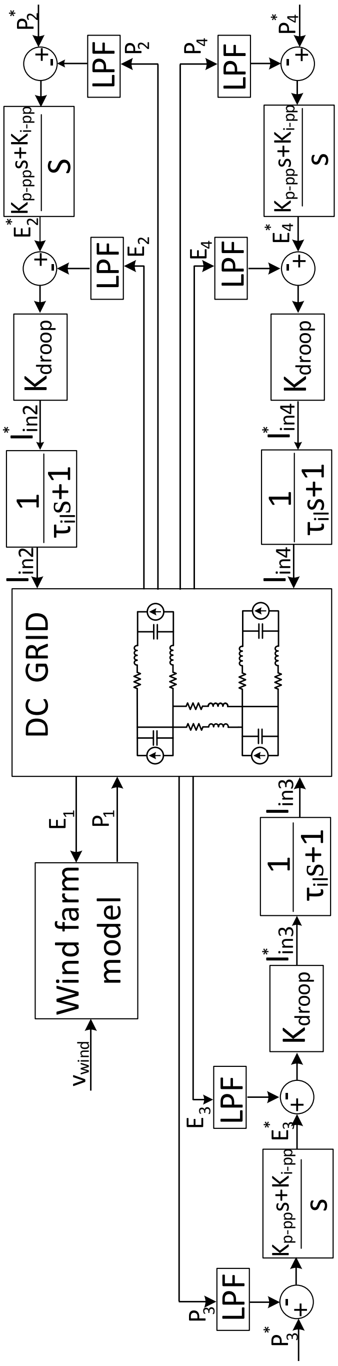

Figure 7.8: Linearised model scheme

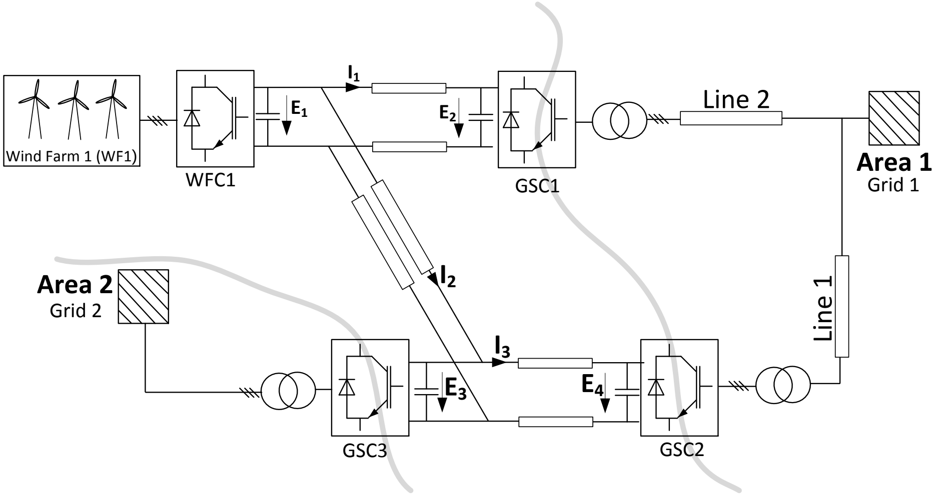

Figure 7.9: General scheme of the simulated multiterminal system

7.4 Simulation

Scenarios have been simulated with Matlab-Simulink in order to test and verify the proposed control scheme. The first simulated scenario is a change in the power reference and the second scenario is a grid side converter disconnection.

The analysed system is a four node MT-HVDC system. One power converter is connected to a wind farm (WFC1). Another power converter is connected to an AC grid (GSC3) and the two other power converter are connected to a second AC area (GSC1 and GSC2), considering an electrical distance between them in the grid side, represented as an AC line. In the studied case, the AC grids are modelled as Thévenin equivalent nodes. A sketch of the system can be seen in Figure 7.9. The parameters used in the simulations can be seen in Table 7.1.

From the operation point of view, GSC1 and GSC2 are connected to the same grid working as a unique area. Power converters and the secondary control are communicated each 20s. In the plotted results, the communication instant is indicated with a circle *com*. This time can be lower but has been selected at a higher value in order to demonstrate the viability of the

Parameter	Value	Units
Cable resistance	0.01	Ω/km
Cable inductance	0.1	mH/km
Power converter capacitance (including cable)	150	μF
Cable 1 length	100	km
Cable 2 length	20	km
Cable 3 length	90	km
Current loop time constant (τ_{il})	0.01	s
Droop controller gain	0.1	A/V
Maximum droop value for rectifiers E_{max-r}	165	kV
Maximum droop value for inverters E_{max-i}	152.4	kV
Wind farm lower voltage limit E_{WF}^{min}	159	kV
wind farm higher voltage limit E_{WF}^{max}	165	kV
Proportional gain power controller K_{p-pp}	5×10^{-7}	V/W
Integral gain power controller K_{i-pp}	3.5×10^{-5}	V/(Ws)
Low pass filter cut-off frequency	15000	Hz
Wind farm inertia time constant (J_{wf})	3	s
Wind farm electrical time constant (τ_{ele})	0.01	s
AC short-circuit power	700	MW
AC voltage	220	kV
AC line resistance R_{ac}	5	Ω
AC line inductance L_{ac}	50.8	mH
AC line 1 resistance R_{ac1}	1.3	Ω
AC line 1 inductance L_{ac1}	10.2	mH

Table 7.1: Parameters of the simulated scenario

Converter	Initial power	Final power	Behaviour
GSC2	30 MW	70 MW	Inverter
GSC3	40 MW	80 MW	Rectifier

Table 7.2: Initial and final power for the change of reference scenario

system operation in unfavourable scenarios. In the following example, the DC redispatch changes the GSC3 original active power set point (P_3^{ter}) sent from the tertiary control (P_3^{ter}) in order to assume the power variation due to the wind variability.

7.4.1 Change of reference

In the first scenario, a power reference change is simulated. At time instant t=120 s, a new power reference is sent to two grid side converters. The power changes are described in the Table 7.2. Figs. 7.11–7.10 show the voltage and the power. The actual values of the grid connected power converters are plotted in solid line and reference values in dashed line.

In the initial time instant t=0 s, the system follows the references shown Table 7.2. The real power is equal to the reference power and an equilibrium voltage points are reached. At time instant t=120 s, new power references are sent to the GSC1 (inverter) and GSC3 (rectifier). As can be seen in Figure 7.10 the power transmitted over the DC grid increases by 40 MW. The dynamics of the system show the typical first order response with a time constant of $1.2s$ which has been chosen as response time for the secondary controller. Depending on the grid requirements, this time constant can be decreased or increased. It can also be observed that the remote secondary controller is adjusting the GSC3 reference to accommodate the wind power variations (difference between the references sent by the tertiary control reference $P_{GSC^*}^{ter}$ and the adjusted reference P_{GSC^*} in Figure7.10).

Focusing on the power reference change, it is clear from Figure 7.11, that the actual voltages before and after the power reference change are relatively similar. The biggest change can be observed in the voltage offsets which are changed as a result of the secondary control action, aiming at achieving the new power references. Furthermore, it can be noted that the GSC3 power

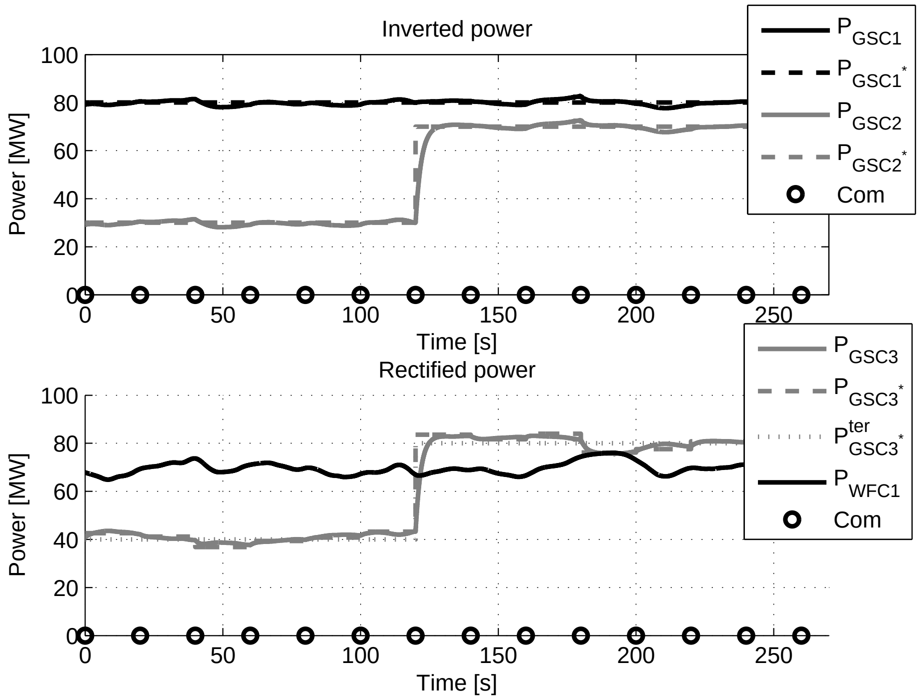

Figure 7.10: Power evolution during a reference change.

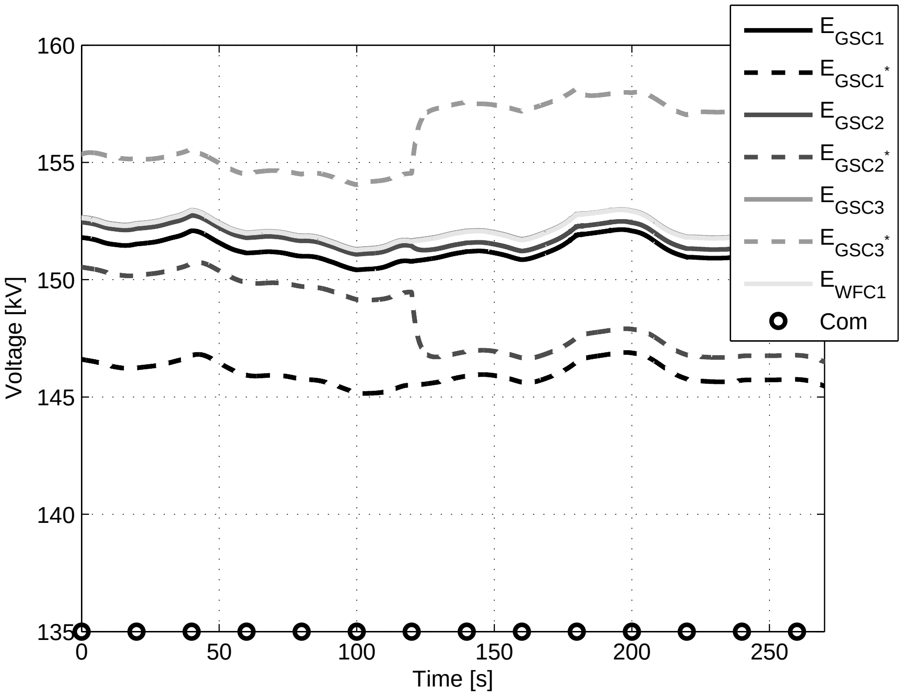

Figure 7.11: Voltage evolution during a reference change.

reference is adapted by the remote secondary action depending on the power injected by the wind farm. Figure 7.12 shows the poles and zeros map of the simulated system. It can be observed that the system is stable because all the poles are in the right hand side plane.

7.4.2 Power Converter Outage

In the second scenario, the grid side power converter, GSC1, experiences an outage at time instant t=10 s. Figs. 7.13–7.14 show the voltage and the power in the MT-HVDC grid.

Before the outage, power converter GSC1 inverts 50 MW, GSC2 inverts 25 MW, GSC3 rectifies 20 MW and the wind farm generates around 50 MW. Losses are assumed by the rectifying unit. At time instant t=40.5s, GSC1 is disconnected and the HVDC system power balance is not in equilibrium. Immediately after the fault, the droop action stops the voltage from rising

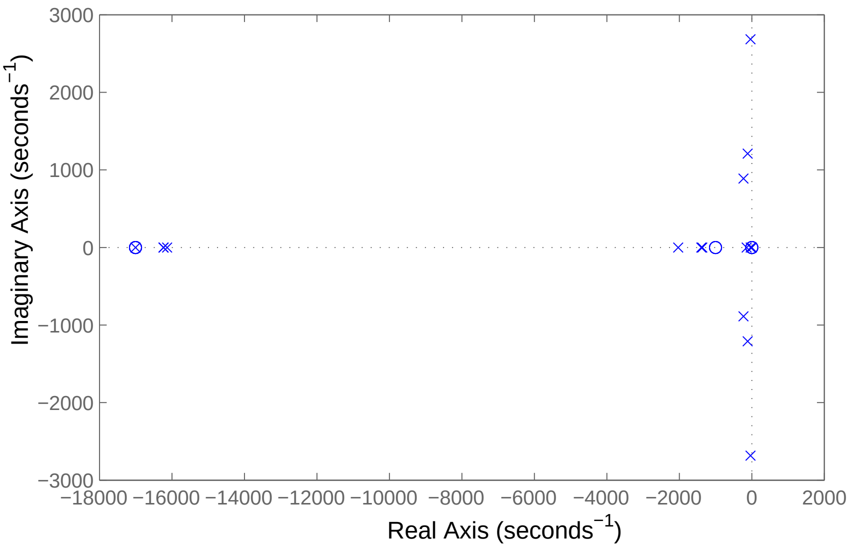

Figure 7.12: Poles and zeros map for the simulation scenario 1

and as a result GSC3 immediately reduces the rectified power and GSC2 increases the inverted power. After that, the secondary controllers start to move the system droop offsets. At time instant t=45 s, GSC2's secondary control is saturated at the maximum limit and the control acts as a droop with a fixed voltage offset.

Between time instants t=45 s and t=50 s, the rectifier unit GSC3 increases the droop offset until the power reference is achieved. At instant t=55 s, the system is working at a new equilibrium point (constant values of E^*) with a saturated droop characteristic at the inverter side (GSC2) and a non-saturated droop offset at the rectifier side (GSC3). This scenario shows that the system can work without issues or instabilities in this operation point. It can be observed that the reference of the disconnected GSC1 goes to the E_{min-i} threshold and the wind farm power reduction is not needed. After the time instant t=60 s, new power references considering the outage are sent. These new references match with the previous equilibrium point as far as the power converters were no saturated.

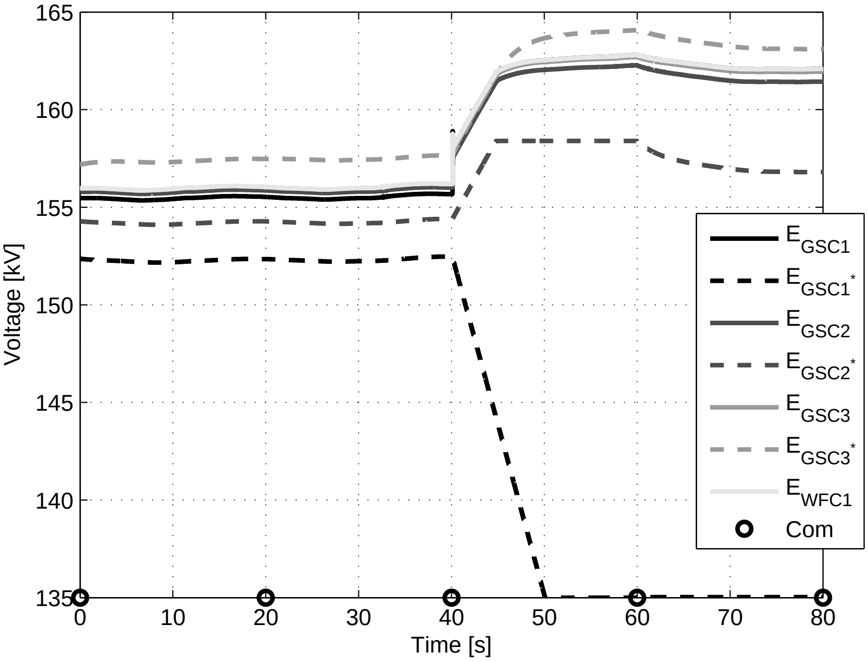

Figure 7.13: Voltage evolution during a reference change.

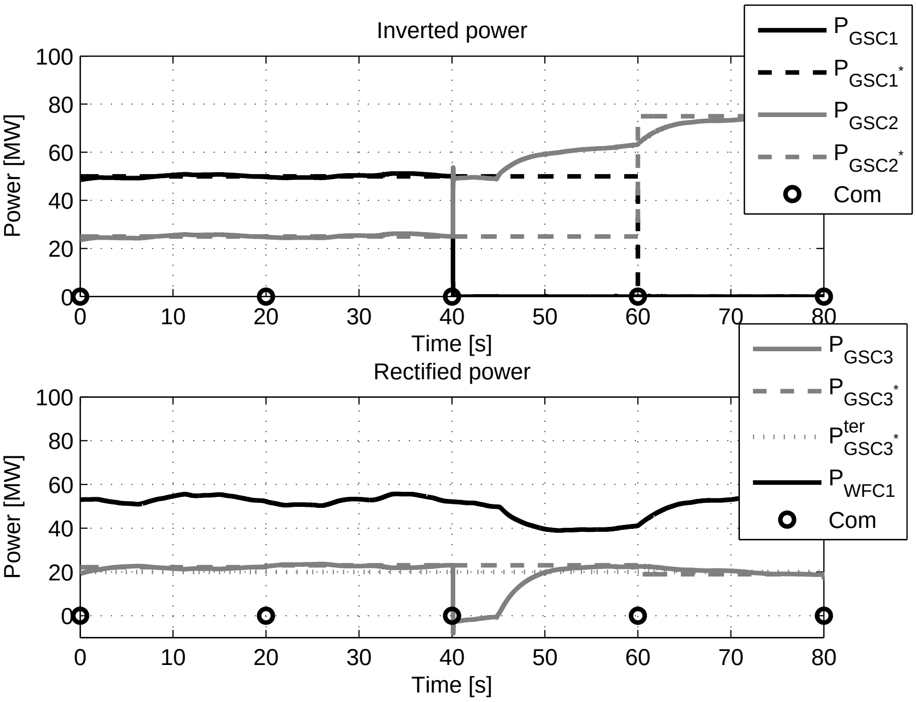

Figure 7.14: Power evolution during a reference change.

7.5 Conclusion

A new control structure for MT-HVDC grids has been presented. The presented scheme consist of a primary, a secondary and a tertiary control similar to the traditional AC grid controls. The primary control is in charge of the DC voltage stability. The secondary control allows us to achieve a given power setpoints, also after a contingency. The tertiary control permits a power scheduling regarding the AC and DC system.

The objective of the proposed control hierarchy is to provide a method that can be implemented in hybrid AC/DC systems with multiple converters connected to different AC and DC systems. The method is HVDC vendor-neutral. The methodology is expected to be well-accepted by industry as it is similar to existing AC control structures. As such, this method could serve as a base for schemes to be introduced into AC/DC grid codes. It is important to note that although the structure is similar to the AC control structures, the time constants differ significantly, specifically those of the inner loops. The operational points of the proposed method, under normal and converter outage have been described. Simulation scenarios, including a power converter disconnection show the validity of the proposed control method for MT-HVDC system.

Chapter 8

Control of a squirrel cage-based wind farm with a single power converter.

8.1 Introduction

Current wind farm are mainly based in Doubly Fed Induction Machine (DFIG) [64] or Permanent Magnet Synchronous Machine (PMSM) with full power converter [65]. These wind turbine concepts require a power converter for each wind turbine. From economics and reliability point of view [66, 67, 68], individual power converters for each wind turbine could be eliminated and a cluster of wind turbines could be controlled with a single VSC converter. Some authors have proposed this scheme using asynchronous [69, 67] and synchronous generators [70, 71].

The present chapter presents a control scheme for a wind turbine cluster with squirrel cage induction generators connected to a single VSC-HVDC. Comparing the SCIG wind turbine cluster to the synchronous generators concept presented in [70, 71], the SCIG wind turbine cluster can show more reduced cost and improved stability. The proposed configuration can be used in wind farms composed of multiple clusters of multiple wind turbines, and for entire offshore wind farms connected to the main grid using HVDC (where the power converter is already needed). Also, the proposed structure could be suitable to adapt constructed SCIG-based land wind farm, adding a back-to-back power converter to inject the power to the grid. The main advantage of the proposed configuration compared to classic wind turbines with individual power converter is that as no power converter is required for the individual wind turbines, the cost can be reduced and reliability increased. The chapter proposes a control scheme which extends the vector control of SCIG to a wind turbine cluster. The proposed vector control improves the dynamic performance of [69], where a scalar control was used for a SCIG wind turbine cluster. The proposed control scheme is based on computing the optimum electrical frequency depending on the different wind speeds and regulating the wind turbine cluster average mechanical speed by controlling the wind turbine cluster active and reactive power using vector control.

On the other hand, offshore wind farms connected by means of a HVDC require fault ride-through capability, which requires fast power reduction of the wind farms when a fault occur. Power reduction methods[72] can be designed using large resistances in VSC-HVDC to dissipate the excess of power, using fast communication systems to reduce the torque in the wind turbines or modifying the wind farm grid voltage or frequency to reduce the electrical power in the VSC. In the proposed scheme, the VSC-HVDC converter controls the active and reactive power of the wind turbine cluster, allowing to reduce the active power rapidly without needing resistances to dissipate the power excess. The reduction of the electrical power implies the need for a mechanical power reduction in each wind turbine which can be provided by the pitch control system by limiting the wind turbine speed.

8.2 Optimal average mechanical speed for wind farms

In [71], an optimal electrical frequency ω was computed for a synchronous generator based wind farm considering that for this type of machine, the turbine speed ω_t is related to the electrical frequency as $\omega_t = \frac{\omega}{PN_{mult}}$ where P is the pole pairs number and N_{mult} is the gearbox multiplication factor of the wind turbine.

In order to extend the same principle to a induction SCIG based wind turbine cluster, it is appropriate to compute the optimal average mechanical speed instead of the grid frequency, due to the asynchronous nature of induction generators.

As discussed in [71], the total power P_{wf} generated by a wind farm composed of N_{wt} identical wind turbines can be expressed as $P_{wf} = \frac{1}{2}\rho A \sum_{i=1}^{N_{wt}} C_P(\lambda_i) v_{wi}^3$

where A is the surface swept by the turbine blades, v_{wi} is the wind speed of the turbine i and $C_P(\lambda_i)$ is the so called power coefficient which is a function of the so called tip speed ratio λ_i. The tip speed ratio is defined as the relation between the speed of the tip of the blades and the speed of the wind $\lambda \triangleq \frac{\omega_t R}{v_w}$ where R is the radius of the turbine.

$C_p(\lambda)$ can be expressed as a polynomial of degree N_{pol} and coefficients a_j:

$$C_p(\lambda) = \sum_{j=0}^{N_{pol}} a_j \lambda^j = \sum_{j=0}^{N_{pol}} a_j \frac{(\omega_{ti} R)^j}{v_w^j} \tag{8.1}$$

As the generator mechanical speed is related to the turbine speed by $\omega_{mi} = N_{mult}\omega_{ti}$, the power generated by each turbine i can be expressed as:

$$P_{wt-i} = \frac{1}{2}\rho A v_{wi}^3 \sum_{j=0}^{N_{pol}} a_j \left(\frac{\omega_{mi} R}{N_{mult} v_{wi}}\right)^j \tag{8.2}$$

The power extracted by the whole cluster can be obtained as the sum of the power generated by each turbine. Rerranging the terms, the total generated power can be put as a function of the average generator mechanical speed $\omega_m = \sum_i \omega_{mi}/N_{wt}$:

$$P_{wf} = \frac{1}{2}\rho A \sum_{i=1}^{N_{wt}} \sum_{j=0}^{N_{pol}} a_j \left(\frac{R}{N_{mult}}\right)^j \omega_m^j v_{wi}^{3-j} \tag{8.3}$$

The optimal average generator speed ω_m^* can be calculated by finding the roots of the derivative of the total generated power as a function of the average speed:

$$\frac{dP_{wf}}{d\omega_m} = 0 \Rightarrow \sum_{j=1}^{N_{pol}} b_j \omega^{j-1} = 0 \tag{8.4}$$

where $b_j \triangleq \frac{1}{2}\rho A j a_j \left(\frac{R}{PN_{mult}}\right)^j \sum_{i=1}^{N_{wt}} v_{wi}^{3-j}$.

Solving (8.4), $N_{pol} - 1$ solutions are found. The obtained real solutions can be substituted in the total power equation (8.3) in order to determine which one corresponds to the absolute maximum.

8.3 Wind turbine cluster grid with a single power converter

The proposed concept can be used in an entire offshore wind farm (Figure 8.1) or in a wind turbine cluster (Figure 8.2). In both case, it consists of a set of wind turbines equipped with SCIG and a single VSC handling all the power captured by the wind turbine cluster (or wind farm). Each turbine is connected to the cluster AC grid by means of a transformer. This configuration permits to operate at variable frequency and thus tracking the optimal average mechanical speed ω_m^* introduced in the previous section. In the case of an entire wind farm with a single power converter, the power contributed by each turbine is gathered in a common connection point and transferred via a main transformer to the VSC-HVDC. The power is then transmitted through an HVDC submarine cable interfaced to the main AC grid by a VSC-HVDC inverter.

In the case of a wind turbine cluster, each cluster VSC collects the cluster power. A DC grid is necessary to collect the power from all the clusters and boost the voltage by means of a DC/DC converter to the required HVDC voltage level.

Although the proposed concept can be applied both to an entire wind farm or to a cluster of wind turbines, an entire wind farm is analysed in the present chapter. The results obtained could be extended to a configuration with multiple clusters.

8.3.1 Wind turbine cluster grid

The VSC can independently control the active and reactive power, which are related to the torque and the magnetising current of each generator, respectively. This is done by applying an appropriate voltage v_c^{abc} to control the currents i_c^{abc} flowing through the converter. The converter voltage v_c^{abc} and the generator voltages v_{si}^{abc} (for $i = 1 \cdots N_{wt}$) are related by the wind farm voltage equation which can be derived for any particular configuration using standard circuit analysis tools.

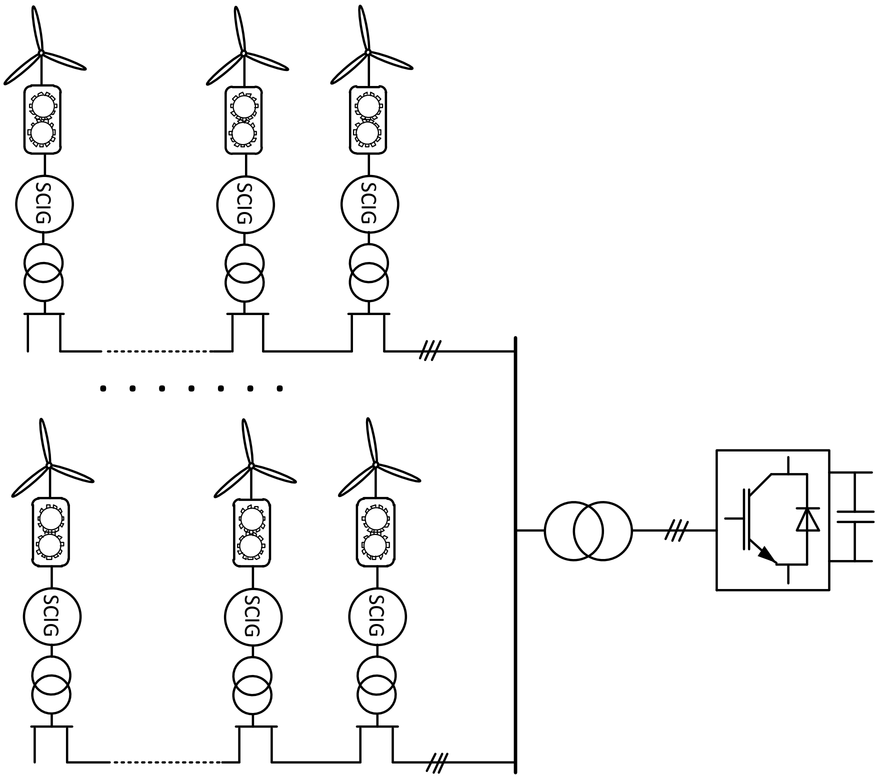

Figure 8.1: Proposed offshore wind farm grid with a single power converter

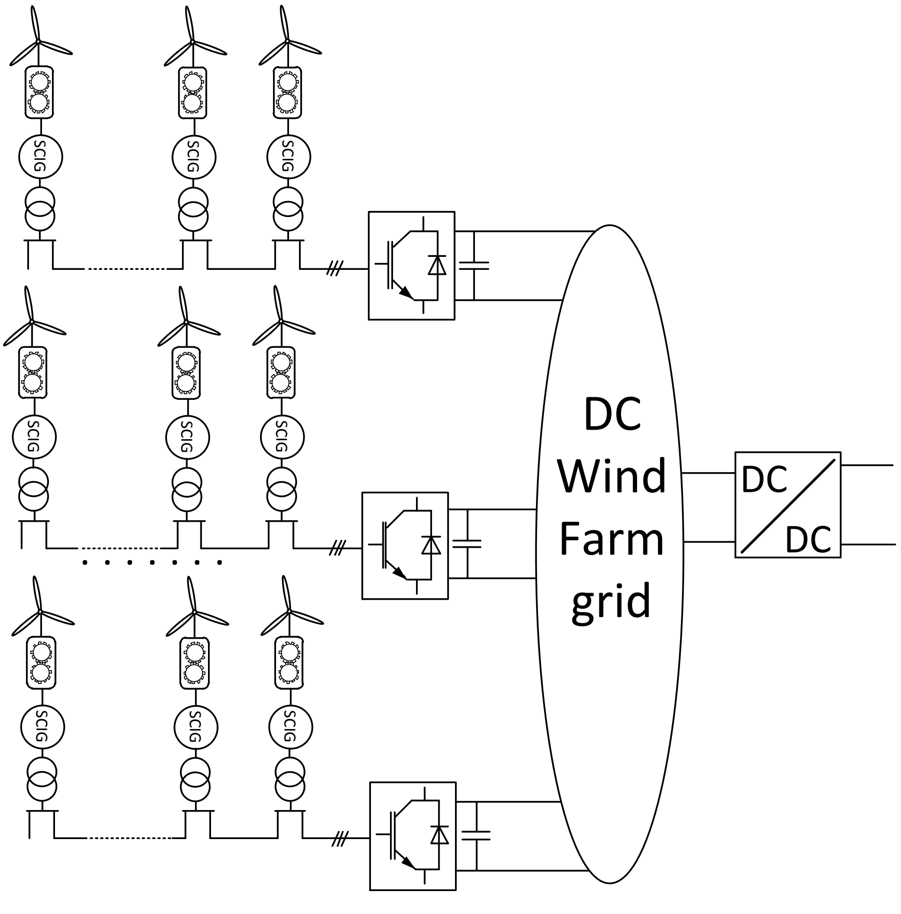

Figure 8.2: Proposed offshore wind farm grid based on multiple wind turbine clusters with a single power converter

8.3.2 Wind turbine driven SCIG

The wind turbine cluster is comprised of N_{wt} wind turbines equipped with SCIG and a variable pitch system. The electrical generator is coupled to the wind rotor using a gearbox. The pitch system allows the regulation of the power captured by each turbine in high wind speed, when the rotational speed or the power generated reaches a given power or speed limit value [73, 74].

The electrical equations for each generator i can be written in the so-called synchronous reference frame [75] as

$$\begin{bmatrix} v_{sq,i} \\ v_{sd,i} \\ 0 \\ 0 \end{bmatrix} = \begin{bmatrix} R_s & L_s\omega & 0 & L_m\omega \\ -L_s\omega & R_s & -L_m\omega & 0 \\ 0 & L_m s\omega & R_r & L_r s\omega \\ -L_m s\omega & 0 & -L_r s\omega & R_r \end{bmatrix} \begin{bmatrix} i_{sq,i} \\ i_{sd,i} \\ i_{rq,i} \\ i_{rd,i} \end{bmatrix} + \begin{bmatrix} L_s & 0 & L_m & 0 \\ 0 & L_s & 0 & L_m \\ L_m & 0 & L_r & 0 \\ 0 & L_m & 0 & L_r \end{bmatrix} \frac{d}{dt} \begin{bmatrix} i_{sq,i} \\ i_{sd,i} \\ i_{rq,i} \\ i_{rd,i} \end{bmatrix}, \qquad (8.5)$$

where $v_{sq,i}$ and $v_{sd,i}$ are the stator voltages, $v_{rq,i}$ and $v_{rd,i}$ are the rotor voltages, s is the generator slip ($s \triangleq 1 - P\omega_m/\omega$), L_s and L_r are the stator and rotor inductances, R_r and R_s are the rotor and stator resistances and L_m is the magnetising inductance.

The torque developed by the generator is given by

$$\Gamma_i = \frac{3}{2}\frac{L_m^2}{L_r}\left(i_{md,i}i_{sq,i} - i_{mq,i}i_{sd,i}\right), \qquad (8.6)$$

where the magnetising currents $i_{mq,i}$ and $i_{md,i}$ depend on the stator and rotor currents as follows

$$i_{mq,i} = i_{sq,i} + \frac{L_r}{L_m} i_{qr,i} \qquad (8.7)$$

$$i_{md,i} = i_{sd,i} + \frac{L_r}{L_m} i_{dr,i} \qquad (8.8)$$

Using a single mass model, the mechanical dynamic behaviour is governed by

$$\frac{d\omega_{m,i}}{dt} = \frac{1}{J}\left(\frac{P_{wt,i}}{\omega_{m,i}} - \Gamma_i\right), \tag{8.9}$$

where J is the total turbine inertia.

8.4 Proposed control scheme

The control strategy for the proposed single converter wind farm configuration is shown in Figure 8.3. The onshore and the offshore converters have different controllers. The objective of the onshore controller is to ensure a stable voltage at the DC bus during the power transmission through the HVDC link and to provide reactive power to the main grid in case of faults [76], whereas the aim of the offshore controller is to regulate the power captured by the entire wind farm. No fast communication systems is required, the HVDC voltage measurement is used to ensure stable operation.

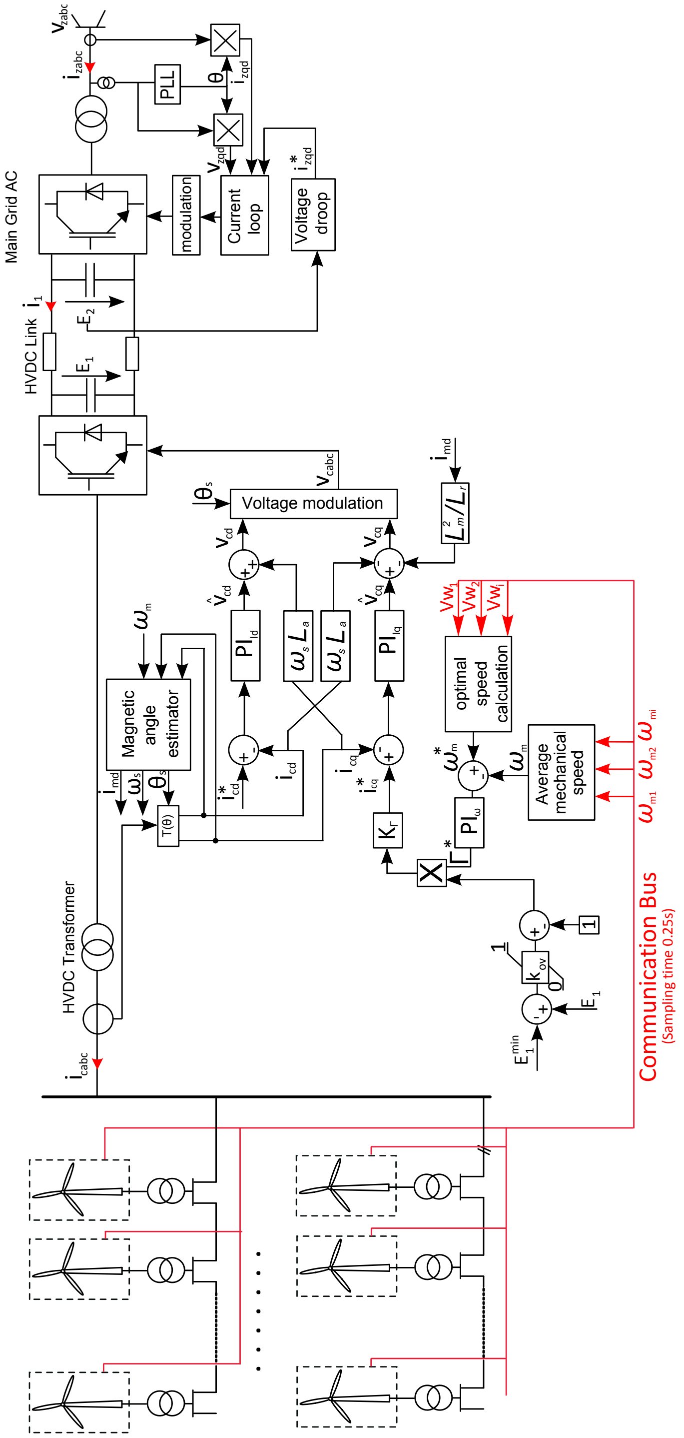

Figure 8.3: Proposed control strategy for the single converter wind farm scheme

8.4.1 Onshore VSC control

The control strategy in the onshore converter is a cascade configuration with two controllers commonly found in VSC. The power converter can control the active and reactive power injected into the grid [42] independently. The active power reference is calculated according to the DC bus voltage using a droop controller [77]. The reactive power reference can be obtained either from a reference signal provided by the transmission system operator or from an AC voltage controller.

As usual, the control of the onshore converter includes limitations on the current references with the aim of avoiding the activation of the over-current protections. The converter can operate in this current limitation mode during severe voltage faults in the AC grid, when the voltages drop and currents rise trying to maintain the transfer of power. During the operation in current limitation mode, the power transmission capability of the converter is reduced and the DC voltage may increase if the power coming from the wind farm is not decreased.

8.4.2 Offshore VSC control

The offshore control consists of two controllers in cascade as illustrated in Figure 8.3. The inner current loop acts on the electric variables of the generators and the outer speed loop acts on the average mechanical speed ω_m. This last controller produces the current reference i_{cq}^* in order to maintain the mechanical speed at the desired value ω_m^*.

Current loop The purpose of this controller is to control the magnetising current and the total torque developed by the wind farm. The proposed controller is based on the flux-oriented vectorial control algorithm for a single SCIG [78, 79]. In this control scheme, the synchronous reference frame angle is chosen so that it matches the angle of the magnetising current, that is, $i_{md} \equiv 0$. Consequently, $i_m = i_{cd}$ and the torque can be controlled by varying the i_{cq} current.

The controller design starts from the SCIG stator equations (8.5) summing the currents of each generator, *i.e.*,

$$i_{cd} = \sum_{i=1}^{N_{wt}} i_{cq,i}, \qquad i_{cq} = \sum_{i=1}^{N_{wt}} i_{cd,i},$$
$$i_{mq} = \sum_{i=1}^{N_{wt}} i_{mq,i}, \qquad i_{md} = \sum_{i=1}^{N_{wt}} i_{md,i}.$$

Then, the aggregated SCIG model is governed by

$$v_{cd} = L_t \frac{di_{cd}}{dt} + R_t i_{cd} + \omega_m i_{cq} L_t, \tag{8.10}$$
$$v_{cq} = L_t \frac{di_{cq}}{dt} + R_t i_{cq} - \omega_m i_{cd} L_t - \frac{L_m^2}{L_r} i_{md} \tag{8.11}$$

where $L_t = (L_s - \frac{L_m^2}{L_r} + L_l)$, L_s is the equivalent electrical grid impedance, $R_t = R_s + R_l$, and R_l is the electrical resistance of the wind farm grid. In this aggregated wind farm model, inductances and resistances of the individual SCIG are divided by the number of wind turbines N_{wt} [80].

The previous model can be decoupled using the average mechanical speed and assuming that the magnetising currents are constant. To this end, the decoupling terms are added to controller outputs $\hat{v}_{cq}$ and $\hat{v}_{cd}$, that is,

$$v_{cd} = \hat{v}_{cd} + \omega_m i_{cd} L_t$$
$$v_{cq} = \hat{v}_{cq} - \omega_m i_{cq} L_t - \frac{L_m^2}{L_r} i_{md}$$

After this change of variables, equations (8.10-8.11) become

$$\hat{v}_{cd} = L_t \frac{di_{cd}}{dt} + R_t i_{cd}, \tag{8.12}$$
$$\hat{v}_{cq} = L_t \frac{di_{cq}}{dt} + R_t i_{cd}. \tag{8.13}$$

Once the system is decoupled, a PI controller can by tuned according to the IMC methodology [16]. Proportional and integral terms are given by

$$k_{p-sc} = \frac{L_t}{\tau_{sc}}, \qquad k_{i-sc} = \frac{R_t}{\tau_{sc}},$$

respectively, where τ_{sc} is the desired time constant of the closed loop system.

As mentioned before, the synchronous reference frame angle is chosen to match the magnetising field of the induction machine. Since this angle cannot be measured, it can be calculated from the stator flux pulsation

$$\omega_s = \frac{-i_{sd} L_r}{R_r i_{md}} \tag{8.14}$$

where the magnetising current i_{mq} is obtained from

$$i_{md} = \int \frac{R_r}{L_r} \left(i_{sq} - i_{md} \right) dt \tag{8.15}$$

The references for the current loop are imposed by the outer loop and the magnetising current required by the induction machine. The reference i^*_{cq} is calculated from torque reference Γ^* provided by the speed controller according to the expression

$$i^*_{cq} = \frac{2}{3} \frac{L_r N_{wf}}{i_{md} L_m^2} \Gamma^* \tag{8.16}$$

The reference i^*_{cd} is given by

$$i^*_{cd} = \frac{V_n N_{wf}}{L_m \omega} \tag{8.17}$$

where V_n is the nominal phase-to-line voltage of the SCIG.

Speed loop This is the higher level and its purpose is to control the average rotational speed of the all wind turbines in the cluster (or farm) and thus regulating the total power capture. The difference between the average mechanical speed ω_m and the reference ω^*_m are entered in a PI controller to produce a reference torque Γ^*.

The PI control law

$$\Gamma^* = K_n(\omega^*_m - \omega_m + \frac{1}{\tau_n} \int \left(\omega^*_m - \omega_m \right) dt)$$

is designed according to [81]

$$K_n = \frac{J_{ag}}{2\tau}, \qquad\qquad \tau_n = \nu\tau,$$

where $J_{ag} = \frac{N_{wt}J}{(PN_{mult})^2}$ is the aggregated equivalent inertia of the whole wind farm, τ is the time constant of the current loop and ν is a speed factor usually chosen as $\nu > 20$.

The sample time in the outer loop is larger than in the inner loop. This ensures that there is sufficient time to transmit the measurements of the rotational speed and the estimations of the wind speed from each turbine to the controller and compute the reference ω_m^*.

Depending on the operation of the wind turbine cluster (or farm), the speed control will seek different objectives:

- In normal operation mode and low wind speed, estimations of the effective wind speed V_i and measurements of the mechanical speed $\omega_{m,i}$ at each wind turbine are sent to the central control. With this information, the central control computes the average mechanical speed reference ω_m^* as described in Section 2 and feeds it into the speed controller, which adjusts the torque developed by the SCIG. Thus, the average mechanical speed are regulated in order to achieve the maximum power capture. While the system is pursuing the maximum power capture objective, the pitch angle is kept constant at its optimal value β_o since the power is below the rated value. In high wind speeds, the offshore controller changes the maximum power capture objective for the aim of keeping the mechanical speed and the power under the limits imposed by the physical limitations of the wind turbines. The pitch controllers of each turbine are used in this circumstance to regulate the power captured by the turbine around the rated value.

- Under fault operation the capability to transfer power of the HVDC link is reduced. In this situation, it is necessary to reduce the power transferred from the wind farm in order to avoid over-voltages in the DC link. The offshore controllers deal with this task by reducing the torque reference and thus reducing the power captured by the wind farm. The offshore converter detects the fault when the DC voltage exceeds a threshold E_1^{min}. When this conditions occurs, the torque reference Γ^* is modified, substracting the reduction torque $\Gamma^*_{red} = \Gamma^* K_{WF}(E_1 - E_1^{min})$ where E_1 is the DC voltage in HVDC terminals. K_{WF} can be designed as $K_{WF} = \dfrac{1}{E_1^{max} - E_1^{min}}$ where E_1^{max} is the maximum voltage permitted.

8.4.3 Wind turbines pitch control

The proposed control scheme of the wind turbine used is shown in Figure 8.4. The pitch control can be acted by the rotational speed or the nominal power. The power-based control is used in normal conditions when the wind speed is higher than the nominal and the captured mechanical power needs to be reduced. The speed-based control is used when the rotational speed is increased, for example due to the electrical power reduction for a AC voltage sag. The maximum value between the both output controllers is used.

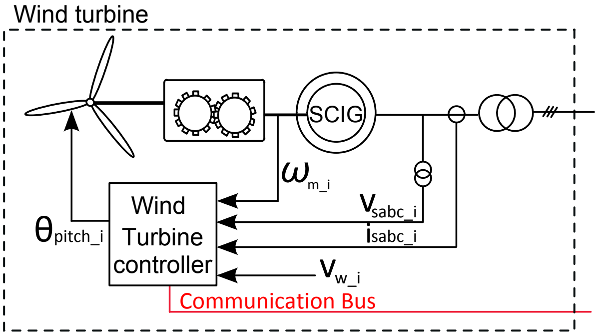

Figure 8.4: Wind turbine and control scheme of the studied fix speed wind turbine

8.5 Simulation results

The proposed control scheme has been evaluated by simulations in the case of an offshore wind farm of 100 wind turbines. The wind turbines have been aggregated in four groups of 25 turbines each. It is assumed that all the wind turbines of a group face the same wind profile, while the different groups can face different winds. An average model is used for the VSC-HVDC.

The parameter values of the wind turbines, generators and gearboxes can be found in Appendix.

Three different scenarios have been considered. The first scenario corresponds to normal operation using four different wind series for each wind turbine group. The second scenario simulates an increasing wind profile that covers the full operating range of the wind turbines. The third scenario analyzes the effects of a voltage sag in the main AC grid, which causes a voltage drop of 85% deep at the point of common connection in the onshore VSC-HVDC. The parameters using for the simulations are

- Power coefficient parameters (C_p): $c_1 = 0.5$, $c_2 = 116$, $c_3 = 0.4$,$c_4 = 0$, $c_5 = 0$, $c_6 = 5$, $c_7 = 21$, $c_8 = 0.08$, $c_9 = 0.035$.
- Wind turbine parameters: $\rho = 1.125$ Kg/m^3, $R = 39$ m, $I_t = 3.6 \cdot 10^6$ kgm^2, $T_s = 0.25$ s.
- SCIG parameters: $V_n = 690$ V, $n_{nominal} = 1530$ min^{-1}, $P_n = 2$ MW, $X_s = 0.075$ pu, $R_s = 0.048$ pu, $X_r = 0.12$ pu, $R_r = 0.018$ pu, $X_l = 3.8$ pu.
- DC Grid parameters: $V = \pm 75$ kV, $R_{DC} = 0.05\ \Omega$, $L_{DC} = 0.005$ H, $C_{DC} = 200\ \mu$F.
- AC Grid parameters: $V_{ac} = 90$ kV, $S_{cc} = 600$ MVA, $X/R = 10$.

The currents are represented in absolute value.

8.5.1 Normal operation in low wind speeds

8.5 shows the simulation results corresponding to the first scenario, where the wind farm is operating in optimum power capture as described in previous sections. The wind profiles faced by each group and the electrical power produced by the entire wind farm can be observed in 8.5a and 8.5b, respectively. The rotational speed of each group along with the average speed are showed in 8.5c and 8.5d. Notice in the zoomed plot that each group is operating close to the average mechanical speed ω_m.

8.5e shows the power coefficient C_P for each group. It can be observed that the energy capture is close to the maximum ($C_P^{\max} = 0.41$) when the wind profiles are similar. As expected, the capture decreases when the wind speeds at each group present significant differences.

The currents and the corresponding references are plotted in 8.5f. Note that i_{cd}^* remains constant as it is related to the magnetising current of the induction machines whereas the i_{cq}^* is related to the desired torque and therefore varies according to the speed reference.

8.5.2 Normal operation during an increasing wind profile

8.6 presents the response of the system to an increasing wind speed profile faced by each group (8.6a). With this wind profile, the power evolves from around 40 MW to the rated power 200 MW (see 8.6b). It can be observed in Figure 8.6c that the wind turbines reach the rotational speed limit at around 13 s. When the rated rotational speed is reached, the controllers leave the maximum power capture objective and seek to maintain the rotational speed close to the rated value 1500 min^{-1}. The pitch angle of each group starts to increase at around 25 s in order to maintain the power close to the rated value (8.6e). Notice that the pitch controllers act locally in each group and therefore they become active at different times. In 8.6e, the pitch control in the groups 1 and 3 become active first since they are exposed to higher wind speeds than the groups 2 and 4 .From 8.6b, it can be observed that the rotational speeds in each group slightly exceed the rated value at 13 s. The converter currents and the corresponding references are plotted in 8.6f.

8.5.3 Operation under fault operation

In 8.7, the behaviour of the proposed scheme during a severe voltage fault in the AC grid is evaluated. In particular, 8.7 shows simulation results corresponding to a three-phase voltage sag of 85% deep in the nominal voltage, starting at 5 s and ending at 5.5 s. In this circumstance, the converter is not capable of transferring to the grid all the power captured by the wind farm without exceeding the current limits. The power excess is stored in the HVDC link capacity and the voltage E_1 starts to rise, as it can be seen in 8.7b. The system enters in fault operation mode when the voltage at the DC bus reaches the threshold $E_1^{min} = 167$ kV. In this mode, the torque reference is modified with the aim of reducing the energy capture. This reduction of

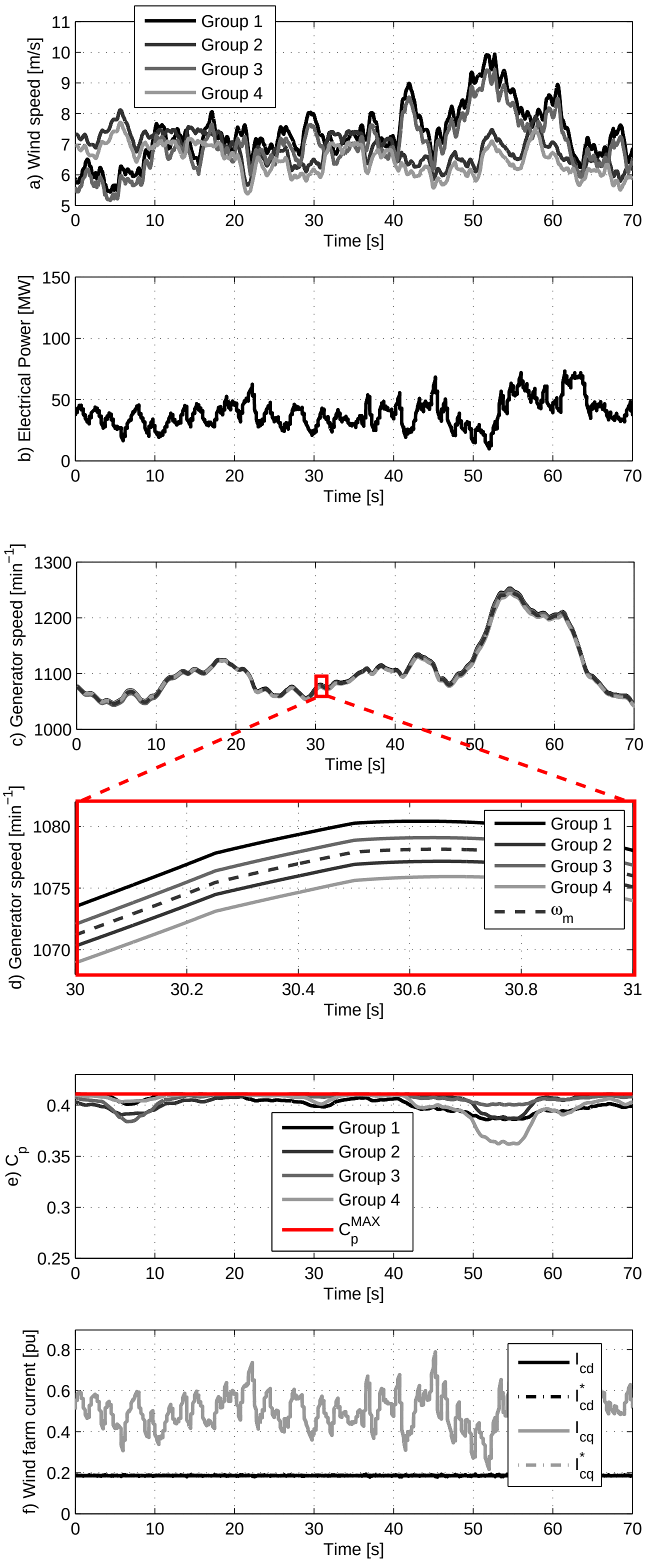

Figure 8.5: Simulation results corresponding to the normal operation scenario in low wind speed

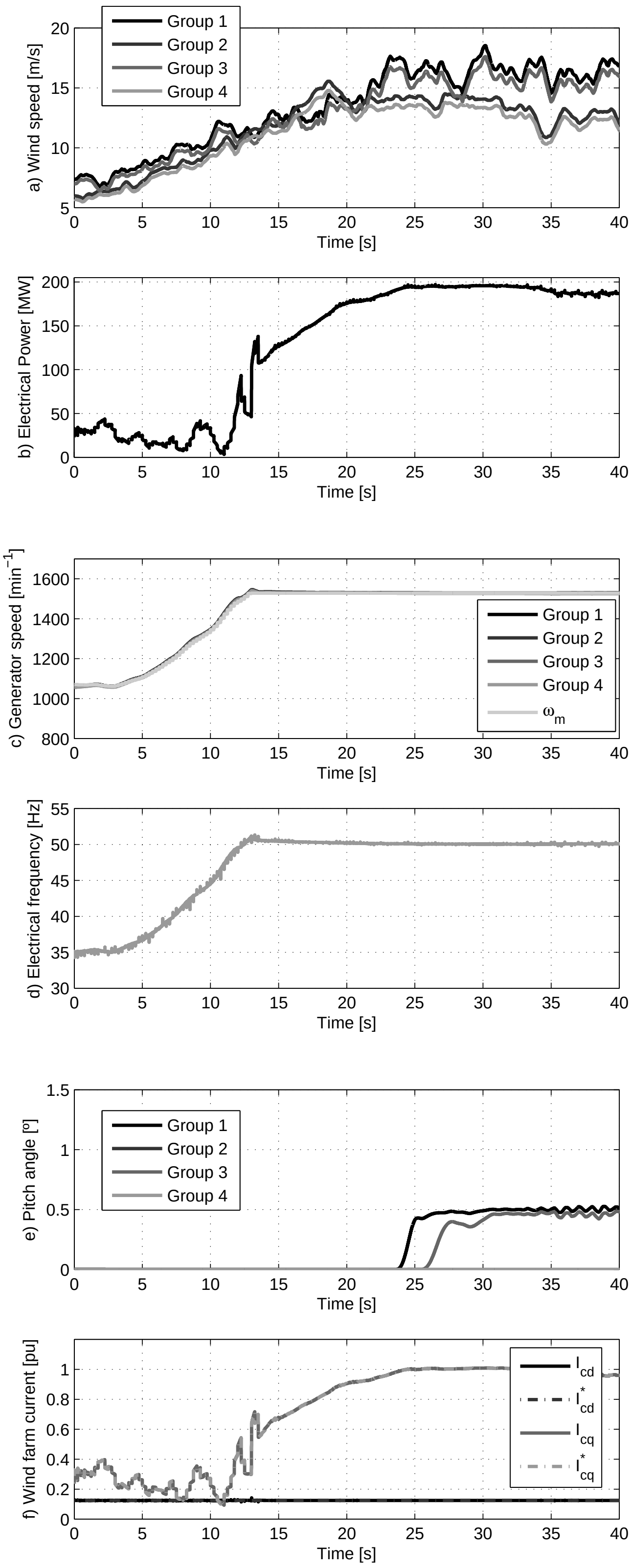

Figure 8.6: Responses to an increasing wind speed profile (normal operation)

the torque reference causes an increment of the rotational speed in all groups and a decrement in the C_P and in the captured power (see 8.7c, 8.7d and 8.7e). In this example, the reduction of the torque reference is so severe that the pitch controllers also must assist in the reduction of the energy capture (8.7f). This correction acts on the voltage loop which operates at a larger sample time (0.25 s), this is the cause of the stepped shape of the electrical power and the DC voltage signals.

Once the voltage sag vanishes, the onshore and offshore converters return to work in normal operation mode. The power coefficients rises to the maximum values and the voltage at the DC bus E_1 returns to the rated value. Also, the mechanical speed of each wind turbines and the captured power return to the nominal values after a transient of approximate 2 s.

8.6 Conclusion

A wind farm control scheme for wind turbine clusters or wind farms equipped with SCIG connected to an unique power converter has been presented. The proposed control scheme is an extension of the classic vector control for a single induction machine, but applied to wind turbine cluster or to an entire wind farm. The proposed control scheme allows the regulation of the average torque and speed of the aggregated wind turbine cluster (or farm). Active power extraction is regulated according to the variation of the electrical frequency. A fast power reduction method is also included in order to guarantee the fault ride-through capability of the proposed scheme. The presented model has been tested with dynamics simulations under different conditions: normal operation, winds speeds increase and a deep voltage sag in the main AC grid.

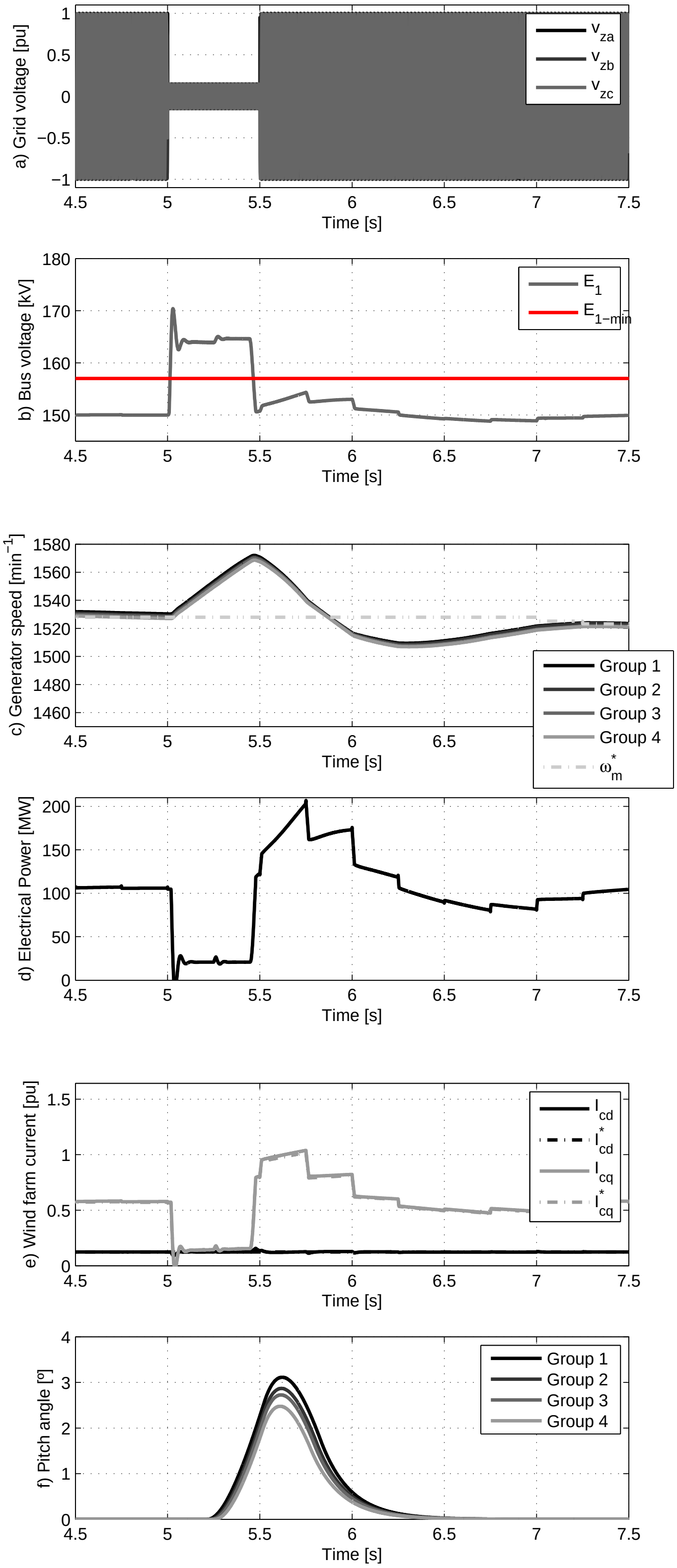

Figure 8.7: Simulation results corresponding to the fault ride-through scenario

Chapter 9

Conclusions

The thesis has covered different aspects for the multiterminal-HVDC systems development. The various pretend to allow the system operation under normal operation and fault conditions and provide full integration with the AC grids ensuring the system stability and the power flow controllability.

The thesis has addressed voltage control in Chapter 2 and the multiterminal HVDC system operation in Chapter 3. A droop-based control scheme has been tested satisfactorily in an experimental platform designed for this purpose in Chapter 4.

The power generation reduction is a crucial issue for MT-HVDC grids. When a contingency takes place, all the generated power might not be injected to the main AC grid and the generated power needs to be reduced. As power converter based systems have a very reduced inertia compared to traditional AC systems, this power reduction must take place almost instantaneously a combined power reduction method based on an HVDC-DBR and a wind farm generated power reduction is proposed in Chapter 5. The advantage of the proposed system is the short faults are controlled by means of the HVDC-DBR and if the fault last more than some seconds the power generated by the wind turbine is decreased.

Previous works on weak grids have indicated that classic control structures are not suitable for VSC connected to weak grids. Chapter 6 has introduced the weak grid phenomena and has analysed the system response considering a vector current control approach. The conclusions from this study have pointed out that the main problem of weak grids is their pronounced non-linear behaviour. This non-linearity is due to the high voltage angle between the VSC and the PCC. The solution proposed in this thesis is based on current vector control and implemented using a gain-scheduled linear controller, which allows to connect a VSC to a weak grid controlling the transferred active power and the voltage at the PCC. The system has been tested by means of simulations that show a positive and stable control performance.

DC voltage control ensures the system stability, but not the power flow that is the final long-term control objective for the TSO. For this reason, a hierarchical power flow control is presented in Chapter 7. The proposed control modifies the primary control set-points allowing the desired power flow in the DC system. The control performance has been checked by means of simulations.

The use of new technologies as HVDC allows new wind farm layouts and configurations. An example of this new configurations is an offshore wind farm equipped with wind turbines based on SCIG where the whole wind farm is controlled by means of the HVDC converter. This structure allows an increase in the system efficiency and the reliability of the system by eliminating the intermediate power converters. In this system, the optimal power extracted from the wind in controlled changing the electrical frequency of the AC by the HVDC converter. In chapter 8 a new control procedure for the mentioned wind farm structure based on vector control is investigated.

9.1 Future Work

From this thesis future research lines have arisen, which appear listed below. Regarding the operation modes and the experimental platform explained in Chapter 4:

- Implementation of the power reduction method described in Chapter 5.
- Implementation of the weak grid control of a VSC connected to a weak grid commented in Chapter 6.
- Implementation of hierarchical control proposed in Chapter 7.

Regarding the proposed power reduction methods in Chapter 5:

- Extension of the control design to MT-HVDC systems.

Regarding the proposed weak grid control presented in Chapter 6:

- Study of the proposed control behaviour during the AC faults and voltage sags.
- Study of the interaction of the proposed controller with others VSC in an HVDC grid.
- Study of the control interaction with weak grids with synchronous generators.

Regarding the proposed hierarchical control for MT-HVDC systems presented in 7:

- Study of other primary control implementations in the hierarchical structure.
- Proposal a tertiary control based on an OPF.

Regarding the control procedure described in Chapter 8:

- Investigation of a sensorless control procedure.
- Investigation of the control with a realistic turbine and cable layout.

Bibliography

[1] I. P. on Climate Change, “Climate change 2013: The physical science basis.” 1

[2] E. E. Agency. Annual european union greenhouse gas inventory from 1990 to 2012 and inventory report 2014. 1

[3] E. Commission. [Online]. Available: http://ec.europa.eu/clima/policies/package/index_en.htm 1

[4] EWEA, “2013 european statistics,” EWEA, Febrary 2013. 1

[5] N. B. Negra, J. Todorovic, and T. Ackermann, “Loss evaluation of HVAC and HVDC transmission solutions for large offshore wind farms,” *Electric Power Systems Research*, vol. 76, no. 11, pp. 916–927, 2006. 2

[6] N. Flourentzou, V. Agelidis, and G. Demetriades, “Vsc-based hvdc power transmission systems: An overview,” *IEEE Transactions on Power Electronics*, vol. 24, no. 3, pp. 592 –602, march 2009. 2

[7] O. Gomis-Bellmunt, J. Liang, J. Ekanayake, R. King, and N. Jenkins, “Topologies of multiterminal HVDC-VSC transmission for large offshore wind farms,” *Electric Power Systems Research*, vol. 81, no. 2, pp. 271–281, 2011. 2

[8] E. Pouresmaeil, C. Miguel-Espinar, M. Massot-Campos, D. Montesinos i Miracle, and O. Gomis Bellmunt, “A control technique for integration of dg units to the electrical networks,” *IEEE Transactions on Industrial Electronics*, vol. Early Access Articles, 2012. 2

[9] S. Bernal-Perez, S. Ano-Villalba, R. Blasco-Gimenez, and J. Rodriguez-Derlee, “Efficiency and fault-ride-through performance of a diode-rectifier and vsc-inverter based hvdc link for off-shore wind farms,”

IEEE Transactions on Industrial Electronics, vol. Early Access Articles, 2012. 2

[10] R. Blasco-Gimenez, N. Aparicio, S. Ano-Villalba, and S. Bernal-Perez, "Lcc-hvdc connection of offshore wind farms with reduced filter banks," *IEEE Transactions on Industrial Electronics*, vol. 60, no. 6, pp. 2372–2380, June 2013. 2

[11] R. Blasco-Gimenez, S. Ano-Villalba, J. Rodriguez-D.Derlee, S. Bernal-Perez, and F. Morant, "Diode-based hvdc link for the connection of large offshore wind farms," *IEEE Transactions on Energy Conversion*, vol. 26, no. 2, pp. 615–626, June 2011. 2

[12] A. Bodin, "Hvdc light a preferable power transmission system for renewable energies," in *Proceedings of the 2011 3rd International Youth Conference on Energetics (IYCE)*, july 2011, pp. 1 –4. 2

[13] D. V. Hertem and M. Ghandhari, "Multi-terminal VSC HVDC for the European supergrid: Obstacles," *Renewable and Sustainable Energy Reviews*, vol. 14, no. 9, pp. 3156–3163, 2010. 2

[14] P. Barrade, *Électronique de puissance*, P. polytechniques et universitaires romandes, Ed., 2006. 8

[15] R. H. Park, "Two-reaction theory of synchronous machines — genralized method of analysis, part i," *AIEE Transactions*, vol. 48, pp. 716 – 727, 1929. 9

[16] L. Harnefors and H.-P. Nee, "Model-based current control of ac machines using the internal model control method," *IEEE Transactions on Industry Applications*, vol. 34, no. 1, pp. 133–141, 1998. 17, 137

[17] S.-K. Chung, "A phase tracking system for three phase utility interface inverters," vol. 15, no. 3, pp. 431–438, 2000. 20, 63, 65, 81

[18] B. R. Beerten, J., "Overview of dc voltage droop control methods for dc grids," *EEE Transactions on Power Systems. submitted*, 2012. 24

[19] L. Xu and L. Yao, "DC voltage control and power dispatch of a multi-terminal HVDC system for integrating large offshore wind farms," *IET Renewable Power Generation*, vol. 5, no. 3, pp. 223–233, 2011. 24, 103, 106, 111

[20] O. Gomis-Bellmunt, J. Liang, J. Ekanayake, and N. Jenkins, "Voltage-current characteristics of multiterminal hvdc-vsc for offshore wind farms," *Electric Power Systems Research*, vol. 81, no. 2, pp. 440 – 450, 2011. 24, 33

[21] L. Shen, M. Barnes, J. Milanovic, and R. Preece, "Control of vsc hvdc system integrated with ac network," in *10th IET International Conference on AC and DC Power Transmission (ACDC 2012)*, Dec 2012. 24

[22] T. K. Vrana, J. Beerten, R. Belmans, and O. B. Fosso, "A classification of dc node voltage control methods for hvdc grids," *Electric Power Systems Research*, vol. 103, pp. 137 – 144, 2013. 26, 103, 106

[23] L. Xu, L. Yao, and M. Bazargan, "Dc grid management of a multi-terminal hvdc transmission system for large offshore wind farms," in *Proc. Int. Conf. Sustainable Power Generation and Supply SUPERGEN '09*, 2009, pp. 1–7. 27

[24] T. M. Haileselassie and K. Uhlen, "Impact of dc line voltage drops on power flow of mtdc using droop control," *IEEE Transactions on Power Systems*, vol. 27, no. 3, pp. 1441–1449, 2012. 27

[25] E. Prieto-Araujo, F. Bianchi, A. Junyent-Ferre, and O. Gomis-Bellmunt, "Methodology for droop control dynamic analysis of multiterminal vsc-hvdc grids for offshore wind farms," *IEEE Transactions on Power Delivery*, vol. 26, no. 4, pp. 2476 –2485, oct. 2011. 27, 56, 63, 103, 106, 113, 116

[26] C. Schauder, "Vector analysis and control of advanced static var compensators," in *International Conference on AC and DC Power Transmission, 1991.*, 1991. 28, 81

[27] A. Egea-Alvarez, A. Junyent-Ferre, O. Gomis-Bellmunt, J. Liang, J. Ekanayake, and N. Jenkins, “Operation and control of vsc-hvdc multiterminal grids for offshore wind,” in *Proceedings of the 2011-14th European Conference on Power Electronics and Applications (EPE 2011)*, 30 2011-sept. 1 2011, pp. 1 –9. 31

[28] J. Liang, O. Gomis-Bellmunt, J. Ekanayake, N. Jenkins, and W. An, “A multi-terminal hvdc transmission system for offshore wind farms with induction generators,” *International Journal of Electrical Power and Energy Systems*, vol. 43, no. 1, pp. 54 – 62, 2012. 33

[29] J. Gray and N. Nakhla, “Prediction of limit cycles in multivariable nonlinear systems,” *IEE Proceedings on Control Theory and Applications*, vol. 128, no. 5, pp. 233–241, September 1981. 54

[30] T.-S. Tsay, “Limit cycle predictions of nonlinear multivariable feedback control systems with large transportation lags,” *J. Control Sci. Eng.*, vol. 2011, Jan. 2011. 54

[31] P. Rault, F. Colas, X. Guillaud, and S. Nguefeu, “Method for small signal stability analysis of vsc-mtdc grids,” in *IEEE Power and Energy Society General Meeting, 2012*, July 2012. 54

[32] G. Kalcon, G. Adam, O. Anaya-Lara, S. Lo, and K. Uhlen, “Small-signal stability analysis of multi-terminal vsc-based dc transmission systems,” *IEEE Transactions on Power Systems*, vol. 27, no. 4, pp. 1818–1830, Nov 2012. 54

[33] J. Conroy and R. Watson, “Aggregate modelling of wind farms containing full-converter wind turbine generators with permanent magnet synchronous machines: transient stability studies,” *IET Renewable Power Generation*, vol. 3, no. 1, pp. 39–52, March 2009. 56, 58

[34] F. D. Bianchi, H. De Battista, and R. J. Mantz, *Wind turbine control systems: principles, modelling and gain scheduling design.* Springer, 2006. 63

[35] K. Tan and S. Islam, “Optimum control strategies in energy conversion of pmsg wind turbine system without mechanical sensors,” *IEEE*

Transactions on Energy Conversion, vol. 19, no. 2, pp. 392–399, 2004. 63

[36] L. Zhang, “Modeling and control of vsc-hvdc links connected to weak ac systems,” Ph.D. dissertation, KTH, 2010. 65, 81, 82

[37] A. Egea-Alvarez, J. Beerten, D. V. Hertem, and O. Gomis-Bellmunt, “Primary and secondary power control of multiterminal hvdc grids,” *10th IET International Conference on AC and DC Power Transmission (ACDC 2012)*, 2012. [Online]. Available: http://digital-library.theiet.org/content/conferences/10.1049/cp.2012.1989 66

[38] J. jaques Slotine and W. Li, *Applied Nonlinear Control*, Pretince-Hall, Ed., 1991. 71

[39] J. Arrillaga, Y. H. Liu, and N. R. Watson, *Flexible Power Transmission: The HVDC Options*, 2007. 81

[40] N. Ahmed, A. Haider, D. Van Hertem, L. Zhang, and H.-P. Nee, “Prospects and challenges of future hvdc supergrids with modular multilevel converters,” in *Proceedings of the 2011-14th European Conference on Power Electronics and Applications (EPE 2011)*, 2011, pp. 1–10. 81

[41] J. Svensson, “Synchronisation methods for grid-connected voltage source converters,” *IEE Proceedings in Generation, Transmission and Distribution*, vol. 148, no. 3, pp. 229–235, 2001. 81

[42] A. Egea-Alvarez, A. Junyent-Ferré, and O. Gomis-Bellmunt, “Active and reactive power control of grid connected distributed generation systems,” in *Modeling and Control of Sustainable Power Systems*, ser. Green Energy and Technology, L. Wang, Ed. Springer Berlin Heidelberg, 2012, pp. 47–81. 81, 94, 136

[43] *IEEE Guide for Planning DC Links Terminating at AC Locations Having Low Short-Circuit Capacities*, 1997. 81

[44] A. Farag, M. Durrant, H. Werner, and K. Abbott, “Robust control of a vsc hvdc terminal attached to a weak ac system,” in *Proceedings of*

IEEE Conference on Control Applications., vol. 1, 2003, pp. 173–177 vol.1. 81

[45] H. Konishi, C. Takahashi, H. Kishibe, and H. Sato, “A consideration of stable operating power limits in vsc-hvdc systems,” in *7th International Conference AC-DC Power Transmission*, 2001, pp. 102–106. 81

[46] L. Harnefors, M. Bongiorno, and S. Lundberg, “Input-admittance calculation and shaping for controlled voltage-source converters,” *IEEE Transactions on Industrial Electronics*, vol. 54, no. 6, pp. 3323–3334, 2007. 82

[47] L. Zhang, L. Harnefors, and H.-P. Nee, “Power-synchronization control of grid-connected voltage-source converters,” *IEEE Transactions on Power Systems*, vol. 25, no. 2, pp. 809–820, May 2010. 82

[48] P. Mitra, L. Zhang, and L. Harnefors, “Offshore wind integration to a weak grid by vsc-hvdc links using power-synchronization control: A case study,” *IEEE Transactions on Power Delivery*, vol. 29, no. 1, pp. 453–461, Feb 2014. 82

[49] J. Zhou and A. Gole, “Vsc transmission limitations imposed by ac system strength and ac impedance characteristics,” in *10th IET International Conference on AC and DC Power Transmission (ACDC 2012)*, 2012, pp. 1–6. 84

[50] N. Bruinsmaa and M. Steinbucha, “A fast algorithm to compute h $_{norm\ \infty}$ source of a transfer function matrix,” vol. 14, pp. 287–293, 1990. 92

[51] P. Apkarian and D. Noll, “Nonsmooth h_∞ synthesis,” *IEEE Transactions on automatic control*, vol. 51, 2006. 92

[52] J. Shamma and M. Athans, “Analysis of gain scheduled control for nonlinear plants,” *IEEE Transactions on Automatic Control*, vol. 35, no. 8, pp. 898–907, Aug 1990. 93

[53] S. Fekri, M. Athans, and A. Pascoal, “Issues, progress and new results in robust adaptive control,” *International Journal of Adaptive Control and Signal Processing*, vol. 20, no. 10, pp. 519–579, 2006. 93

[54] M. Aragues, A. Egea, O. Gomis, and A. Sumper, “Optimum voltage control for loss minimization in HVDC multi-terminal transmission systems for large offshore wind farms,” *Electric Power Systems Research*, vol. 89, pp. 54–63, 2012. 103, 106, 111

[55] Y. G. Rebours, D. S. Kirschen, M. Trotignon, and S. Rossignol, “A survey of frequency and voltage control ancillary services mdash;part i: Technical features,” vol. 22, no. 1, pp. 350 –357, feb. 2007. 104

[56] European Network of Transmission System Operators for Electricity (ENTSO-E), “Operation handbook,” ENTSO-E, Tech. Rep., 2012. [Online]. Available: https://www.entsoe.eu/publications/system-operations-reports/operation-handbook/ 104

[57] P. Rault, X. Guillaud, F. Colas, and S. Nguefeu, “Investigation on interactions between ac and dc grids,” in *IEEE PowerTech (POWERTECH), 2013 Grenoble*, June 2013. 105

[58] W. Lu and B.-T. Ooi, “Dc overvoltage control during loss of converter in multiterminal voltage-source converter-based hvdc (m-vsc-hvdc),” *IEEE Transactions on Power Delivery*, vol. 18, no. 3, pp. 915 – 920, july 2003. 106

[59] A. Egea-Alvarez, F. Bianchi, A. Junyent-Ferre, G. Gross, and O. Gomis-Bellmunt, “Voltage control of multiterminal vsc-hvdc transmission systems for offshore wind power plants: Design and implementation in a scaled platform,” vol. 60, no. 6, pp. 2381–2391, 2013. 106, 108

[60] W. Wang, M. Barnes, and O. Marjanovic, “Droop control modelling and analysis of multi-terminal vsc-hvdc for offshore wind farms,” in *10th IET International Conference on AC and DC Power Transmission (ACDC 2012)*, Dec 2012. 106

[61] N. Bengiamin and W. Chan, "Multilevel load-frequency control of interconnected power systems," *Proceedings of the Institution of Electrical Engineers*, vol. 125, no. 6, 1978. 106, 112

[62] L. M. Fernandez, F. Jurado, and J. R. Saenz, "Aggregated dynamic model for wind farms with doubly fed induction generator wind turbines," *Renewable Energy*, vol. 33, no. 1, pp. 129 – 140, 2008. 115

[63] J. Morren and S. W. H. D. Haan, "Ridethrough of wind turbines with doubly-fed induction generator during a voltage dip," *IEEE Transactions on Energy Conversion*, vol. 20, no. 2, pp. 435–441, June 2005. 116

[64] S. Muller, M. Deicke, and R. D. Doncker, "Doubly fed induction generator systems for wind turbines," *IEEE Industry Applications Magazine*, vol. 8, no. 3, pp. 26–33, 2002. 127

[65] M. Chinchilla, S. Arnaltes, and J. C. Burgos, "Control of permanent-magnet generators applied to variable-speed wind-energy systems connected to the grid," *IEEE Transactions on Energy Conversion*, vol. 21, pp. 130–135, 2006. 127

[66] O. Gomis-Bellmunt, A. Junyent-Ferré, A. Sumper, and S. Galceran-Arellano, "Maximum generation power evaluation of variable frequency offshore wind farms when connected to a single power converter," *Applied Energy*, vol. 87, pp. 3103–3109, 2010. 127

[67] M. de Prada Gil, O. Gomis-Bellmunt, A. Sumper, and J. Bergas-Jané, "Analysis of a multi turbine offshore wind farm connected to a single large power converter operated with variable frequency," *Energy*, vol. 36, no. 5, pp. 3272 – 3281, 2011. [Online]. Available: http://www.sciencedirect.com/science/article/pii/S0360544211001769 127

[68] J. L. Domínguez-García, D. J. Rogers, C. E. Ugalde-Loo, J. Liang, and O. Gomis-Bellmunt, "Effect of non-standard operating frequencies on the economic cost of offshore ac networks," *Renewable Energy*, vol. 44, no. 0, pp. 267 – 280, 2012. [Online]. Available: http://www.sciencedirect.com/science/article/pii/S0960148112001048 127

[69] L. Trilla, O. Gomis-Bellmunt, A. Junyent-Ferre, and A. Sudria-Andreu, "Analysis of total power extracted with common converter wind farm topology," in *Electrical Machines (ICEM), 2010 XIX International Conference on*, sept. 2010, pp. 1 –6. 127, 128

[70] D. Jovcic and N. Strachan, "Offshore wind farm with centralised power conversion and DC interconnection," *IET Generation, Transmission and Distribution*, vol. 3, pp. 586–595, 2009. 127

[71] O. Gomis-Bellmunt, A. Junyent-Ferre, A. Sumper, and J. Bergas-Jane, "Control of a wind farm based on synchronous generators with a central hvdc-vsc converter," *Power Systems, IEEE Transactions on*, vol. PP, no. 99, p. 1, 2010. 127, 128

[72] R. L. Hendriks, R. Völzke, and W. L. Kling, "Fault ride-through strategies for vsc-connected wind parks," in *EWEC*, 2009. 128

[73] L. Holdsworth, I. Charalambous, J. Ekanayake, and N. Jenkins, "Power system fault ride through capabilities of induction generator based wind turbines," *Wind Engineering*, vol. Volume 28, Number 4 / June 2004, pp. 399–409, 2004. 133

[74] F. Bianchi, H. De Battista, and R. Mantz, "Optimal gain-scheduled control of fixed-speed active stall wind turbines," *Renewable Power Generation, IET*, vol. 2, no. 4, pp. 228 –238, 2008. 133

[75] P. C. Krause, *analysis of electric machinery.* Mc Graw Hill, 1986. 133

[76] J. Liang, O. Gomis-Bellmunt, J. Ekanayake, and N. Jenkins, "Control of multi-terminal vsc-hvdc transmission for offshore wind power," in *Proc. 13th European Conf. Power Electronics and Applications EPE '09*, 2009, pp. 1–10. 134

[77] L. Xu and B. Andersen, "Grid connection of large offshore wind farms using HVDC," *Wind Energy*, vol. 9, no. 4, pp. 371–382, 2006. 136

[78] M. P. Kazmierkowski, R. Krishnan, and F. Blaabjerg, *Control in power electronics.* Elsevier, 2002. 136

[79] P. Vas, *Sensorless Vector and Direct Torque Control.* Oxford University Press, 1998. 136

[80] W. Qiao, R. Harley, and G. Venayagamoorthy, “Dynamic modeling of wind farms with fixed-speed wind turbine generators,” pp. 1 –8, june 2007. 137

[81] G. Terörde, *Electrical Drives and Control Techniques*, B. U. A. Leuven, Ed., 2004. 139

Appendix A

List of publications

A.1 Publication related to this thesis

A.1.1 Journal publications (Peer reviewed Journals)

- Agustí Egea-Alvarez, Fernando Bianchi, Adria Junyent-Ferre, Gabriel Gross, Oriol Gomis-Bellmunt, "Voltage Control of Multiterminal VSC-HVDC Transmission Systems for Offshore Wind Power Plants: Design and Implementation in a Scaled Platform", *IEEE Transactions on Industrial Electronics*, Vol. 60, No. 6, Pp. 2381-2391, June 2013.

- Agusti Egea-Alvarez, Adria Junyent-Ferre, Oriol Gomis-Bellmunt, Jun Liang, Janaka Ekanayake, Nicholas Jenkins. "Operation and control of vsc-hvdc multiterminal grids for offshore wind" *EPE Journal* Vol. 23, No. 2, 2014.

- Agustí Egea-Alvarez, Adrià Junyent-Ferre, Joan Bergas-Jané, Fernando D Bianchi, Oriol Gomis-Bellmunt, "Control of a wind turbine cluster based on squirrel cage induction generators connected to a single VSC power converter", *International Journal of Electrical Power and Energy Systems*, Vol. 61, Pp 523-530, October 2014.

- Agustí Egea-Alvarez, Sajjad (Fekri) Fekriasl, Fainan Hassan, Oriol Gomis-Bellmunt, "Advanced vector control for voltage source converters connected to weak grids" Submitted to *"IEEE Transactions on Power Systems" (first revision).*

- Agustí Egea-Alvarez, Jef Beerten, Dirk Van Hertem, Oriol Gomis-Bellmunt, "Hierarchical power control of multiterminal HVDC grids", Submitted to *"Electrical Power System Research" (first revision).*

- Agustí Egea-Alvarez, Mònica Aragüés-Peñalba, Oriol Gomis-Bellmunt, Coordinated power reduction control for operation and fault conditions, Under preparation.

A.1.2 Conference papers

- Oriol Gomis-Bellmunt, Agustí Egea-Alvarez, Adrià Junyent-Ferré, Jun Liang, Janaka Ekanayake, Nick Jenkins. "Multiterminal HVDC-VSC for offshore wind power integration", *IEEE Power and Energy Society General Meeting*, Detroit, 2011.
- Agusti Egea-Alvarez, Adria Junyent-Ferre, Oriol Gomis-Bellmunt, Jun Liang, Janaka Ekanayake, Nicholas Jenkins. "Operation and control of vsc-hvdc multiterminal grids for offshore wind" *European Power Electronics*, Birmingham, September 2011.
- Agustí Egea-Alvarez, Fernando Bianchi, Adria Junyent-Ferré, Gabriel Gross, Oriol Gomis-Bellmunt, "Experimental implementation of a voltage control for a Multiterminal VSC-HVDC offshore transmission system", *3rd IEEE PES International Conference and Exhibition on Innovative Smart Grid Technologies (ISGT Europe)*, Berlin, October 2012.
- Agusti Egea-Alvarez, Jef Beerten, Dirk Van Hertem, Oriol Gomis-Bellmunt, "Primary and secondary power control of multiterminal HVDC grids", *IET AC/DC Conference*, Birmingham, December 2012.
- Agusti Egea-Alvarez, Adria Junyent-Ferre, Gabriel Gross, Samuel Galceran-Arellano, Oriol Gomis-Bellmunt, "Multiterminal-HVDC scaled platform for offshore wind transmission systems emulation",*15th European Conference on Power Electronics and Applications (EPE)*, Lille, September 2013.
- Agusti Egea-Alvarez, Oriol Gomis-Bellmunt, Antoni Sudrià-Andreu "Sensorless control of a power converter for a cluster of small wind turbines", *EWEA Conference*, Barcelona, March 2014.

A.1.3 Book chapters

- Agustí Egea-Alvarez, Adria Junyent-Ferré, Oriol Gomis-Bellmunt, "Active and reactive power control of grid connected distributed generation systems", *"Modeling and Control of Sustainable Power Systems"*, Springer, 2012.
- Jef Beerten, Agusti Egea, Til Kristian Vrana, "Control principles of HVDC grids", *"Building the grid of the future using HVDC"*, Willey, Pending to be published.

A.1.4 Brochures

- CIGRE Working group B4-58 Brochure. *"Devices for Load flow Control and Methodologies for Direct Voltage Control in a Meshed HVDC Grid"*, Pending to be published.

A.2 Other publications realized during the PhD

A.2.1 Journal articles

- Mònica Aragüés-Peñalba, Agustí Egea-Alvarez, Oriol Gomis-Bellmunt, Andreas Sumper, "Optimum voltage control for loss minimization in HVDC multi-terminal transmission systems for large offshore wind farms", *Electric Power Systems Research*, Vol 89, Pp. 54-63, August 2012.
- Mònica Aragüés-Peñalba, Agustí Egea-Àlvarez, Samuel Galceran Arellano, Oriol Gomis-Bellmunt, "Droop control for loss minimization in HVDC multi-terminal transmission systems for large offshore wind farms", *Electric Power Systems Research*, Vol 112, Pp. 48-56, July 2014.
- Fernando D Bianchi, Agustí Egea-Alvarez, Adrià Junyent-Ferré, Oriol Gomis-Bellmunt "Optimal control of voltage source converters under power system faults", *Control Engineering Practice*, Vol. 20, Pp 539-546, May 2012.

A.2.2 Conference articles

- Lluis Trilla, Oriol Gomis-Bellmunt, Adria Junyent-Ferré, Agustí Egea Alvarez, Antoni Sudria-Andreu, "Control of a squirrel cage induction generator wind farm connected to a single power converter", *45th International Universities Power Engineering Conference (UPEC)*, Cardiff, September 2010.

- Raul Perez-Martinez, Roberto Villafafila-Robles, Pau Lloret-Gallego, Agusti Egea-Alvarez, Andreas Sumper, Angel Silos-Sanchez, "Protection system remote laboratory", *International Conference on Electrical Power Quality and Utilisation*, Lisbon, October 2011.

A.2.3 Magazine article

- Mònica Aragüés Peñalba, Eduardo Prieto Araujo, Agustí Egea Alvarez, Oriol Gomis Bellmunt *Buran - Barcelona IEEE Student Branch magazine*, May 2013.

- Agustí Egea Álvarez, Mònica Aragüés Peñalba, Oriol Gomis Bellmunt, Toni Sudrià i Andreu, "Tendencias en el sector eólico. Offshore y repowering", *Automática e Instrumentación.* January 2014

- Mònica Aragüés Peñalba, Oriol Gomis Bellmunt, Toni Sudrià i Andreu, Agustí Egea Álvarez, *Automática e Instrumentación*, January 2014.

- Agustí Egea Álvarez, Mònica Aragüés Peñalba, Oriol Gomis Bellmunt, Toni Sudrià Andreu, "EWEA 2014", *Automática e Instrumentación.* May 2014.